CHALMERS
UNIVERSITY OF TECHNOLOGY

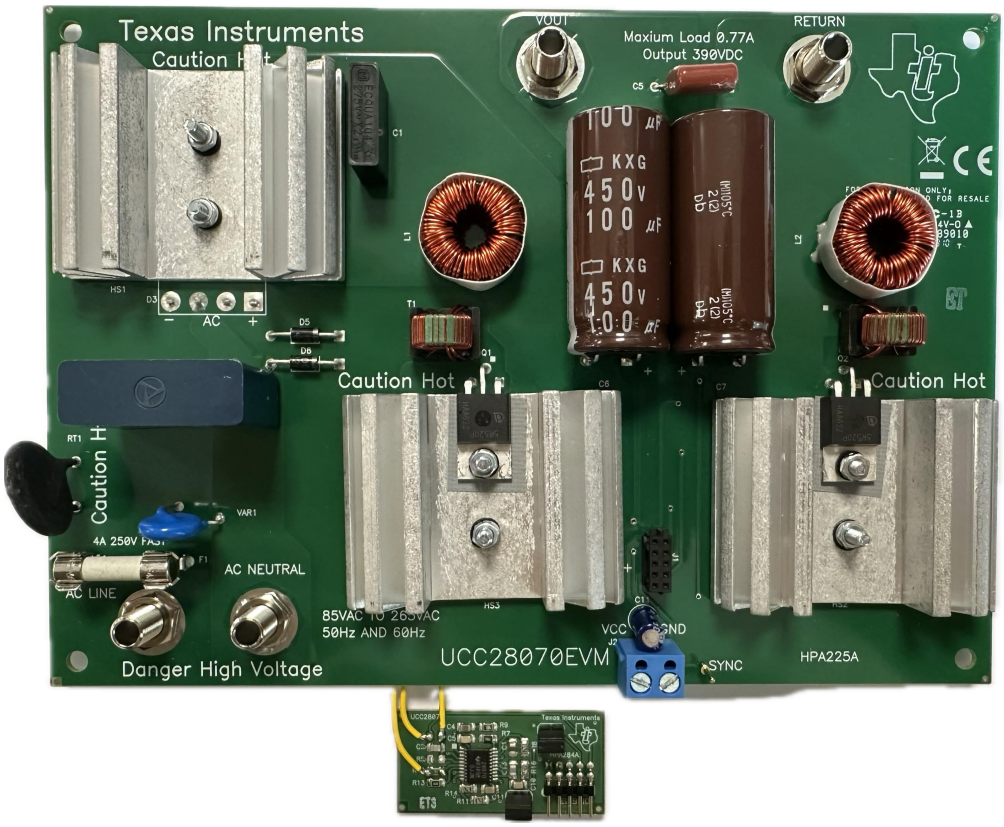

Grid stabilization utilizing an AC/DC converter with adjustable power factor

Master's thesis in Sustainable Electric Power Engineering and Electromobility

EMIN HANUSA
IVAN KUSTURA

DEPARTMENT OF ELECTRICAL ENGINEERING
CHALMERS UNIVERSITY OF TECHNOLOGY
Gothenburg, Sweden 2024
www.chalmers.se

Master's thesis 2024

Grid stabilization utilizing an AC/DC converter with adjustable power factor

EMIN HANUSA & IVAN KUSTURA

CHALMERS
UNIVERSITY OF TECHNOLOGY

Department of Electrical Engineering
Division of Electric Power Engineering
Chalmers University of Technology
Gothenburg, Sweden 2024

Grid stabilization utilizing an AC/DC converter with adjustable power factor

EMIN HANUSA
IVAN KUSTURA

Supervisor: Fredrik Larsson, Ericsson
Examiner: Torbjörn Thiringer, Department of Electrical Engineering

Master's Thesis 2024
Department of Electrical Engineering
Division of Electric Power Engineering
Chalmers University of Technology
SE-412 96 Gothenburg
Telephone +46 31 772 1000

Typeset in LaTeX
Gothenburg, Sweden 2024

Grid stabilization utilizing an AC/DC converter with adjustable power factor
EMIN HANNUSA
IVAN KUSTURA
Department of Electrical Engineering
Division of Electric Power Engineering
Chalmers University of Technology

Abstract

This master thesis investigates the feasibility and consequences of implementing a modified single phase AC/DC converter with adjustable power factor, enabling a local phase compensation in the electrical grid. The theory was validated through simulations in LTspice and a real-world prototype was made from an existing evaluation kit from Texas Instruments. The desired power factor was obtained though a phase shift, employing two primary approaches: one analog and one digital. For the main analog case that provided the best signal integrity, a signal generator and a diode bridge were used to modify the phase angle. Conversely, the digital case utilized the Arduino UNO R4 with an integrated 12 bit digital to analog converter.

The project showed that with an increased phase shift between the current and voltage, a greater local phase compensation could be achieved. This came at the expense of lower efficiency in the converter, transients through the zero crossings, and an increase in harmonics. For one case, where the output current was set to 0.5 A, the maximum amount of phase shift obtained was 13.5°. Simultaneously, the efficiency decreased from 94.3 % to 72.1 % and the total harmonic distortion of the current increased from 38.9 % to 72.6 %.

Additionally, the prototype was tested in a microgrid environment with an AC side current of 1.59 A RMS, demonstrating its ability to achieve a local phase compensation. It was seen that when the current from the converter was high, 0.977 A RMS, the grid current could be adjusted significantly. Conversely, for a lower current, 0.111 A RMS, only minor adjustments could be made. Key regulations were also studied, including IEEE 519-2022 and IEC 61000 that govern performance and electromagnetic compatibility.

Furthermore, the project investigated how local power factor adjustments via a single phase AC/DC converter could enhance grid efficiency and stability. This is of importance for voltage regulation with growing renewable energy integration. The technology could be implemented across Ericsson's base stations, where each station could provide a local grid stabilization service.

Keywords: AC/DC Converter, Power Factor Correction, Local Phase Compensation, Phase Shift, Grid Efficiency, Real-World Prototype.

Acknowledgements

We would like to express our gratitude to everyone who has helped us through our master's thesis journey at the Ericsson Power department. This experience has been a very educative and challenging opportunity, which was made possible by the support of a host of remarkable individuals.

First and foremost we would like to thank our supervisor at Ericsson, Fredrik Larsson, for his expertise, patience, and valuable input which guided us through this process. Thanks to our examiner at Chalmers, Torbjörn Thiringer, for his guidance and insightful discussions.

Furthermore, we would like to thank all the colleagues at Ericsson, especially the AC/DC hardware team, who gave us valuable practical inputs regarding the testing and validation stages of the project. Additionally, a special acknowledgment goes to Stefan Olofsson for his expertise in AC/DC converters.

Emin Hanusa and Ivan Kustura, Gothenburg, June 2024

Contents

1
Introduction

1.1 Background

Controlling reactive power in the electrical grid is essential for maintaining a stable and efficient power system. Reactive power is the component of electrical power that oscillates between the source and the load without performing any useful work. A fundamental reason for the necessity of controlling reactive power lies in voltage regulation. Devices such as motors and transformers, characterized by inductive loads, consume reactive power, leading to a lagging power factor. Without proper control, this could result in voltage instability across the grid, thereby affecting voltage regulation and impacting the operation of electrical devices. Conversely, capacitive loads contribute to a leading power factor, resulting in voltage instability.

Voltage regulation becomes important when there is an excess of either leading- or lagging reactive power, emphasizing the need for control mechanisms. Managing reactive power plays a crucial role in optimizing the efficiency and stability of the electrical grid. It facilitates power factor improvement, which reduces energy losses and maximizes power transfer efficiency. This in turn contributes to a increased lifetime for electrical equipment.

With the transition towards increased renewable energy sources such as wind and solar, there's a increased need for various grid stabilization services. Unlike traditional power generation from fossil and nuclear plants, providing consistent and controllable output, renewables introduce variable output. Therefore, it is of importance to manage the reactive power for grid stability. One possible solution regarding this is through an active AC/DC converter with adjustable power factor. The active management of both inductive and capacitive reactive power is vital for voltage stability, power factor improvement and equipment efficiency, laying the foundation for a resilient future electrical grid.

1.2 Purpose of work

As for today, there are few commercial solutions offering both inductive and capacitive behavior with user-defined power factor. This thesis aims to investigate the feasibility and potential of developing a single phase AC/DC converter with adjustable power factor. This allows for a controllable inductive or capacitive behavior, utilized for various grid stabilisation services.

1.3 Scope

The overall objective of this thesis is to analyze the possibility of local phase compensation by adjusting the power factor using an single phase AC/DC converter. A theoretical analysis on the demand and potential application for this technology will be conducted. A demonstrator will virtually be developed, alongside a real-life prototype of the regulated AC/DC converter. This prototype is based on modifying an existing evaluation kit from Texas Instruments, to achieve the controllable inductive and capacitive features. The performance of the prototype will be compared to the virtual demonstrator and is based on meeting the local grid needs. The present regulatory aspect will also be taken into account.

1.3.1 Research questions

The report studies the following questions:

- Propose an AC/DC converter solution with user defined power factor through modifying an existing AC/DC evaluation kit.
- Determine at a high level, the demand and application for a local phase compensation through the proposed AC/DC converter.

2
Theory

2.1 Technical background

2.1.1 Power triangle

In electrical systems, the power is divided into active and reactive power, which together constitute the apparent power [1]. Understanding these components is a necessity for comprehending the behaviour, efficiency and performance of electrical systems. These three components, the active-, reactive- and apparent power are illustrated in Figure 2.1, graphically showing the conjunction between them through the angle φ.

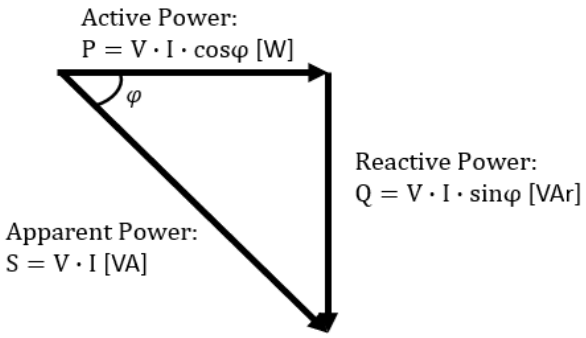

Figure 2.1: Power triangle with active, reactive and apparent power.

Active power represents the actual energy consumed by an electrical device to perform useful work. It is measured in watts, W, and is denoted by the real component of the power in an alternating current, AC, system. It is calculated as

$$P = VI\cos(\varphi) \tag{2.1}$$

where V is the voltage, I the current and φ angle of the load impedance.

The reactive power is the power that oscillates between the source and the load without performing any actual work. It is measured in volt-amperes reactive, VAr, and is denoted by the imaginary component of the power in an AC system. The reactive power is determined as

$$Q = VI\sin(\varphi) \tag{2.2}$$

and emerges due to the presence of inductive and capacitive elements in a circuit. Devices such as motors, transformers, and capacitors contribute to the flow of reactive power. While reactive power itself does not do any work, it is crucial for maintaining voltage levels and supporting the overall grid stability [2].

The apparent power is the combination of active- and reactive power, measured in volt-amperes, VA. It is a measure of the total power flowing in the circuit, and calculated as

$$S = VI \tag{2.3}$$

2.1.2 Power factor

Another measurement is the power factor, PF, which is the ratio between the active- and reactive power [3]. When a purely resistive load is applied, only active power is used and there is no phase difference between current and the voltage. No reactive power is therefore drawn and the active power is equal to the apparent power, giving a unity PF. This implies that all the power flowing is being used for useful work. Aiming for a power factor approaching unity is therefore desirable, as it signifies efficient utilization of electrical energy in the grid, through the lowest possible current for a given power level [2].

When there is an inductor or capacitor present in the circuit, a phase difference is created, leading to reactive power being drawn [3]. In a perfectly balanced system, where the phases of inductive and capacitive components are exactly opposite, they can effectively cancel out each other out [4]. However, if the system is not balanced, and there is an increased presence of inductive loads, such as motors and transformers, the current will lag the voltage. This results in a lagging power factor, shown in Figure 2.2.

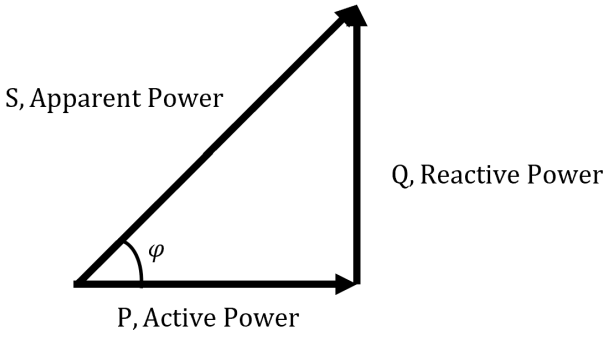

Figure 2.2: Power triangle with inductive load, lagging current.

On the contrary, if the system contains a higher presence of capacitive loads, the current will lead the voltage, resulting in a power factor less than one. This case is shown in Figure 2.3.

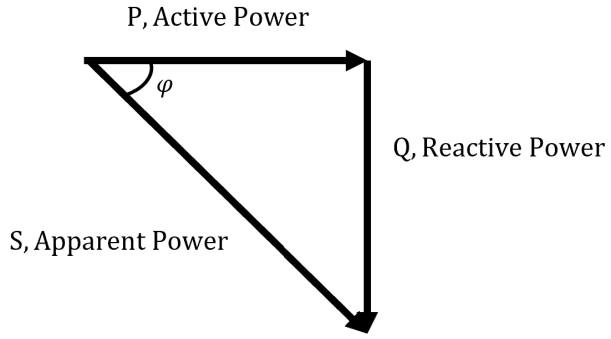

Figure 2.3: Power triangle with capacitive load, leading current.

The power factor is therefore given by

$$PF = \frac{P}{S} = \frac{VI\cos(\varphi)}{VI} \tag{2.4}$$

2.1.3 Harmonics and THD

Another important aspect to consider is harmonics, which are waveforms consisting of multiples of the fundamental frequency [4]. They can be caused by nonlinear loads, such as computers and lights, and can disturb the quality of the grid.

The total harmonic distortion, THD, is the measurement of how much the harmonics are affecting a waveform [4]. It is usually measured as the sum of all the harmonics along with the effect of the fundamental frequency. By reducing the THD value the impact of harmonics on the waveform is minimized, resulting in a purer signal. THD is therefore an important parameter in order to assess the signal quality.

If assumed that the input RMS voltage is an ideal sinusoidal waveform with no harmonics, resulting in $V_{RMS} = V_{1,RMS}$, (2.4) could be rewritten as the product of the displacement power factor, k_{DPF}, and the distortion power factor, k_{D} [5], expressed as

$$PF = k_D k_{DPF} \tag{2.5}$$

The displacement- and distortion power factor could be written as

$$k_{DPF} = \cos(\varphi) \quad ; \quad k_D = \frac{I_{1,RMS}}{I_{RMS}} \tag{2.6}$$

where φ is the phase angle and $I_{1,RMS}$ is the fundamental component of the total current, I_{RMS}. The distortion power factor is directly related to the harmonic distortion, THD, which gives

$$THD = \frac{\sqrt{\sum_{n=2}^{\infty} {I_n}^2}}{I_{1,RMS}} \quad \rightarrow \quad k_D = \frac{1}{\sqrt{1 + (THD)^2}} \tag{2.7}$$

By combining (2.6) and (2.7), the following total power factor equation is derived

$$PF = k_D k_{DPF} = \frac{1}{\sqrt{1 + (THD)^2}} \cos(\varphi) \tag{2.8}$$

which considers both the displacement power factor and the distortion power factor.

2.2 Single phase passive AC/DC converter

A critical consideration in converter design is ensuring adequate power quality. This necessity arises from the fact that most modern devices are connected to the main power supply, requiring the conversion of AC to DC power [4]. This conversion process is called rectification. It is commonly used in applications such as power supplies, air conditioners, battery chargers, electric cars, and solar power systems, to mention some. The process of passive rectification is achieved by using power converters consisting of a diode bridge, usually followed by a large capacitor for smoothing and lowering the output ripple, see Figure 2.4. The power supply is shown as a sinusoidal voltage source, V_s, in series with its internal impedance, which is mainly inductive and is represented by L_s. However, passive rectification can cause some problems in the main power supply. This is because the converter does not draw power in a smooth way (non-sinusoidal), which creates additional electrical oscillations, harmonics.

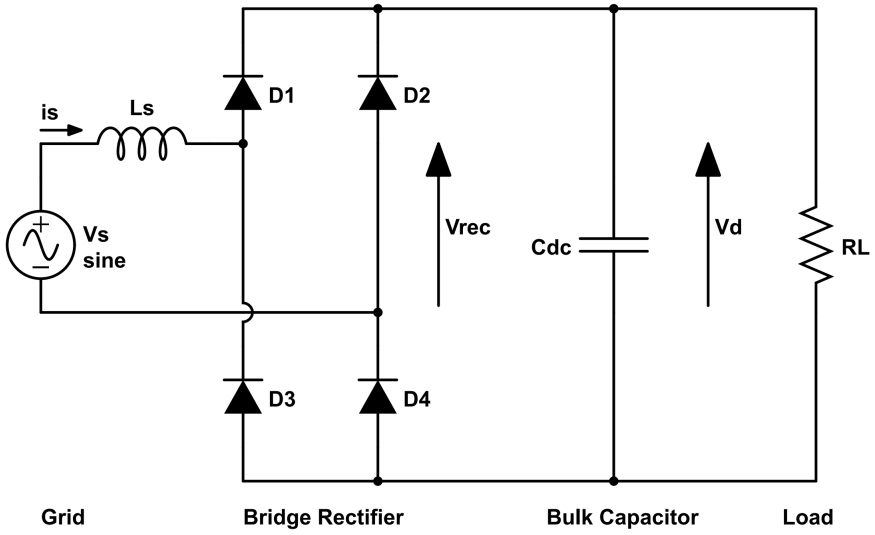

Figure 2.4: AC/DC rectification using diode bridge and bulk capacitor.

The non-sinusoidal phenomena, presented in Figure 2.5, demonstrates the waveforms of the line current, I, and grid voltage, V, and the numerous current harmonics for the conventional rectification approach.

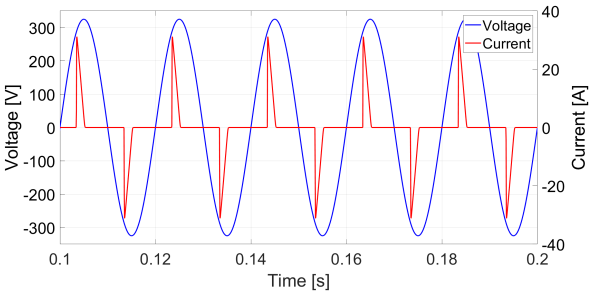

(a) AC voltage and current using a passive rectifier.

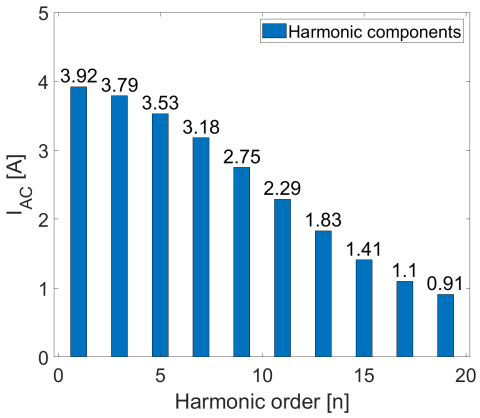

(b) Current FFT spectrum using a passive rectifier.

Figure 2.5: Input voltage and current of passive rectifier with its harmonic content.

2.2.1 Passive AC/DC converter with $L_s = 0$

In Figure 2.6 L_s is assumed to zero, while the DC side of the rectifier is replaced by either a resistance or a constant DC current source. The representation of a load by a constant DC current is an approximation to a case when a large inductor is connected in series with the DC output for filtering.

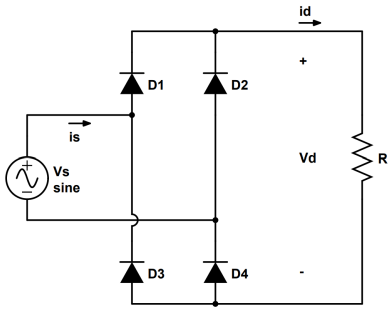

(a) DC side replaced by a resistive load.

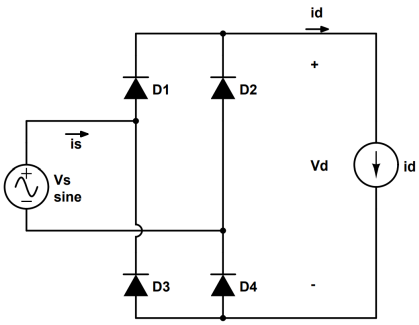

(b) DC side replaced by a current source.

Figure 2.6: Two bridge rectifiers with $L_s = 0$ but different loads.

The circuits from Figure 2.6 are redrawn in Figure 2.7, highlighting that this circuit consists of two sets of diodes: the top group with diodes 1 and 2, and the bottom group with diodes 3 and 4. When the inductor L_s is set to zero, it becomes evident how each group of diodes operates. The current (i_d) flows continuously through one diode from the top group and one diode from the bottom group.

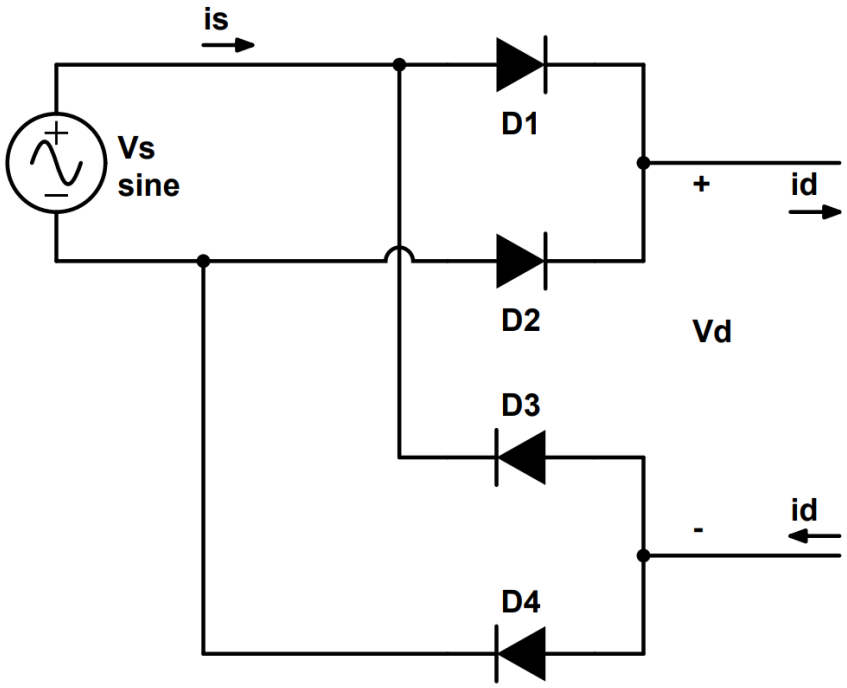

Figure 2.7: Redrawn structure of the rectifiers in Figure 2.6.

In the top group, where the cathodes of the two diodes share a common potential, the diode with its anode at the highest potential conducts i_d [4]. This means that when the voltage source, V_s, is positive, diode 1 conducts i_d, and V_s appears as a reverse-bias voltage across diode 3. When V_s goes negative, the current i_d instantly shifts to diode 3 since L_s is zero, and a reverse-bias voltage appears over diode 1.

In the bottom group, where the anodes of the two diodes share a common potential, the diode with its cathode at the lowest potential conducts i_d. This means when V_s is positive, diode 2 carries i_d, and V_s appears as a reverse-bias voltage across diode 4. When V_s goes negative, the current i_d instantaneously shifts to diode 4, and a reverse-bias voltage appears over diode 2.

When the voltage, V_s, is positive, the diode 1 and diode 4 conducts and the output voltage will be equal to the input voltage, $V_d = V_s$, and output current will be equal to the input current $i_d = i_s$. This is only applicable for ideal components. On the other hand, when V_s is negative, diode 2 and diode 3 will conduct, and therefore the output voltage will be $V_d = -V_s$ and similarly the current will be $i_s = -i_d$. The DC voltage of the converter can be expressed as

$$V_d(t) = |V_s| \tag{2.9}$$

similarly, the current on the AC side can be expressed as

$$i_s = \begin{cases} i_d \text{ if } V_s > 0 \\ -i_d \text{ if } V_s < 0 \end{cases} \tag{2.10}$$

Due to the assumption of $L_s = 0$, the transition between the two values is instantaneous. The average value of the output voltage can be obtained by integrating a sine wave over a half period. The average output voltage is expressed as

$$V_{d,avg} = \frac{2}{\pi}\sqrt{2}V_s \approx 0.9V_s \tag{2.11}$$

where V_s in this case is the RMS value for the input voltage.

When performing a Fourier analysis of current i_s, the fundamental and the harmonic components can be obtained [4]. The RMS value of the fundamental component is expressed as

$$i_{s1} = \frac{2}{\pi}\sqrt{2}i_d = 0.9i_d \tag{2.12}$$

The RMS values for the harmonics are expressed as

$$i_{sh} = \begin{cases} 0 & \text{for even values of h and} \\ i_{s1}/h & \text{for odd values of h} \end{cases} \tag{2.13}$$

where i_{sh} is a harmonic component and h is representing the harmonic order. The harmonic components are displayed in Figure 2.8 and THD is calculated by (2.7) to 48.43 % with the fundamental component of 1 A.

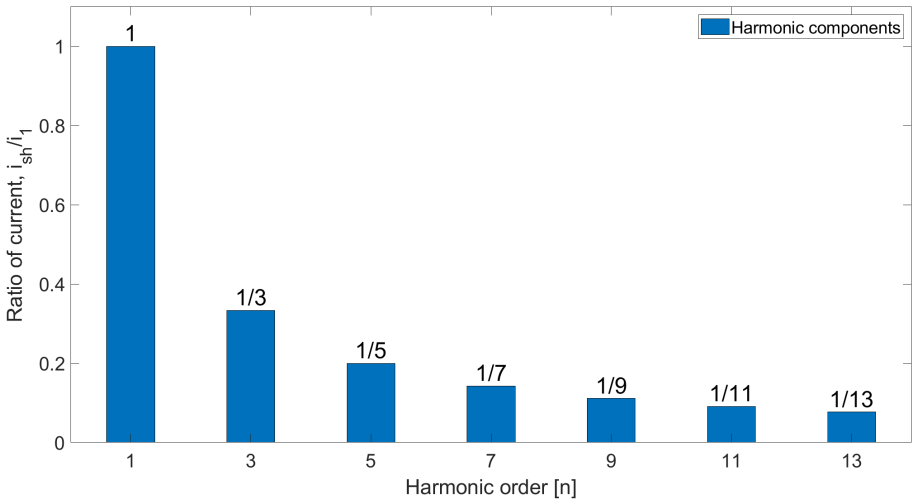

Figure 2.8: Harmonic components of idealized rectifier with $L_s = 0$.

2.2.2 Passive AC/DC converter with finite L_s

To make the line current waveform better, an inductor could be added on the AC side, effectively increasing the value of L_s [4]. In this case the load is represented by a constant DC current, I_d. Consequently, due to the finite L_s, the transition of the AC side current from a positive value of $+I_d$ to $-I_d$ (or vice versa) will not happen instantaneously. This process, where the current conduction shifts from one diode (or a set of diodes) to the other, is known as the current commutation process.

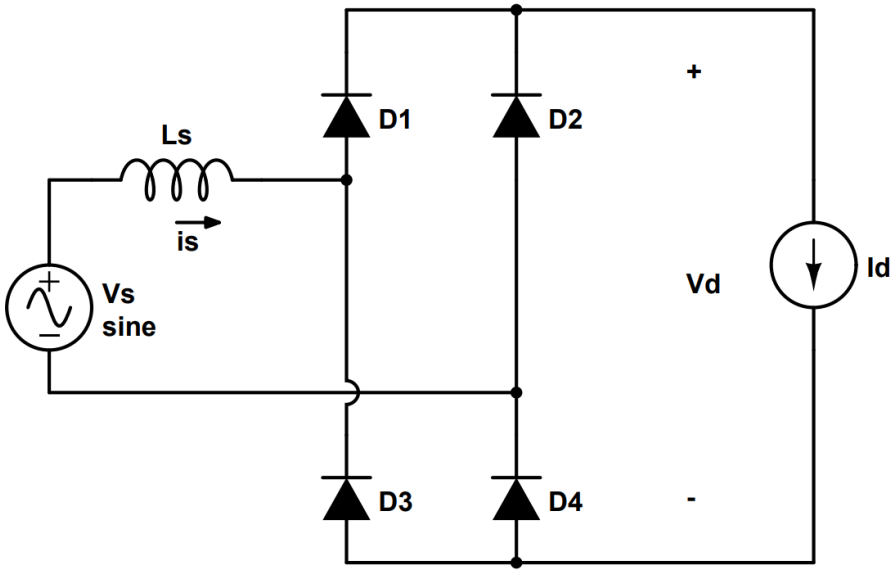

Figure 2.9: Single phase AC/DC converter with finite L_s.

Current commutation occurs at the transition point between the positive and negative half-cycles of the AC input. It can be divided in two stages, end of positive half cycle and start of negative half cycle.

During the end of the positive half cycle, when the input AC voltage approaches zero and starts to reverse its polarity, diodes 1 and 4 (which were conducting) become reverse-biased. There is a brief moment when these diodes are still conducting, due to the characteristics of the diode referred to as the diode's reverse recovery time.

During the start of the negative half cycle, almost simultaneously, diodes 2 and 3 start to become forward-biased as the input voltage becomes negative. However, there's a slight overlap during which diode 1 and 4 are turning off, and diode 3 and 4 are starting to conduct.

This overlap and the brief period of no or minimal conduction is where the commutation takes place. Proper commutation ensures that there are no short circuits and the diodes effectively block current when reverse-biased. Due to the commutation the output voltage, $V_{d,avg}$ will be reduced and expressed as

$$V_{d,avg} = \frac{2}{\pi}\sqrt{2}V_s - \frac{2\omega L_s I_d}{\pi} \tag{2.14}$$

where L_s is the value of the inductance on the AC side, I_d is the constant DC current and ω is $2\pi f$.

In practical applications, current commutation is critical as improper commutation can lead to voltage spikes, diode stress, and inefficiency [6]. Ideal diodes exhibit commutation instantaneously, while real diodes posses characteristics like recovery time affecting the commutation.

2.3 Boost converter

A boost converter or a step-up converter, shown in Figure 2.10, is a circuit which takes a DC voltage and increases it to a higher DC voltage by utilizing an inductor to store energy [7]. When the circuit turns on, current flows through the inductor, building up a magnetic field and storing energy. When the circuit turns off, the inductor resists the change in current and pushes the stored energy to the output. This energy is transferred to a capacitor, which helps maintain a steady output voltage. By controlling the on and off cycles of the circuit through Pulse Width Modulation (PWM), the switching frequency of the boost converter can be precisely regulated. This control mechanism allows for the adjustment of the amount of energy transferred to the capacitor, ensuring efficient energy conversion. This finally results in an increase of the output- compared to the input voltage. Observe that power is conserved, meaning that while the voltage increases, the output current decreases, maintaining the same power level.

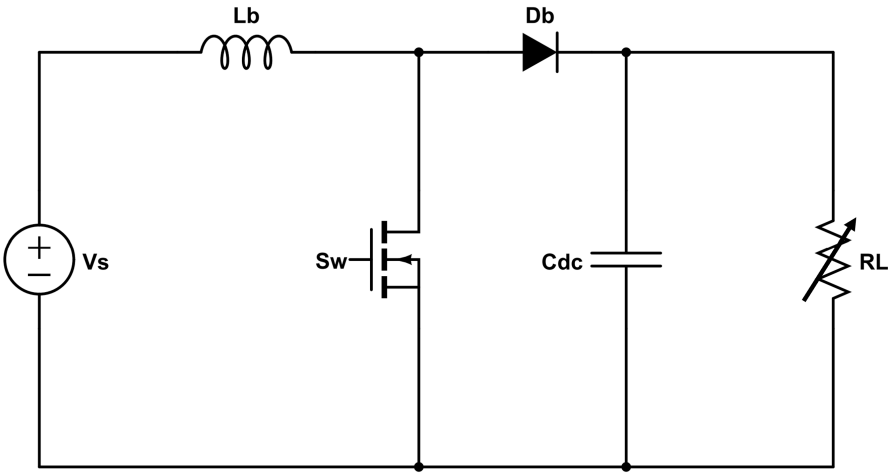

Figure 2.10: Boost DC/DC converter.

The boost converter's two operational modes are illustrated in Figure 2.11. During the on stage, Figure 2.11a, the switch is closed, enabling current to flow through it. The capacitor is simultaneously discharged through the load. Conversely, during the off stage, Figure 2.11b, the switch opens, allowing the capacitor to recharge from the power source.

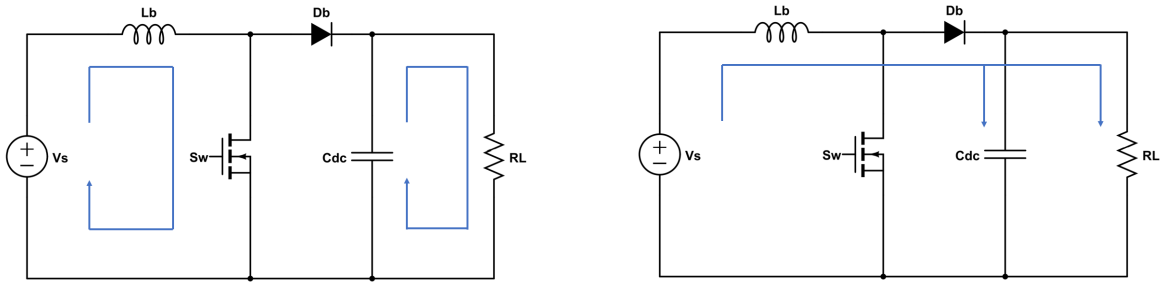

(a) Switch ON. **(b)** Switch OFF.

Figure 2.11: The two operational modes of the boost converter.

2.4 Active AC/DC with boost PFC converter

In practical situations, achieving unity power factor is challenging due to the presence of energy storage components like capacitors and inductors. However, using active power factor correction, PFC, converters between the power source and the load, a power factor greater than 0.99 could be achieved [8]. Figure 2.12, illustrates the boost PFC converter which is commonly used in PFC applications. As the universal line voltage ranges from 85-265 V, it varies sinusoidally up to a peak voltage of 375 V [9]. Therefore a step-up converter is required to obtain a DC link voltage of 380 V or more.

Boost converters are preferred because the input remains continuously connected to the power source through the inductor, L_b [8]. This continuous connection ensures that the current does not experience high rates of change, di/dt. This makes it easier to shape the input current by controlling the switching device, S_w, and achieving low THD. A well known method for controlling the boost PFC is with average current control [10]. It uses two loops for smooth operation, one loop keeps the input current in sync with the input voltage, maximizing efficiency. The other loop ensures a steady output voltage. While these loops offer great benefits, designing them can be difficult as they require a lot of components.

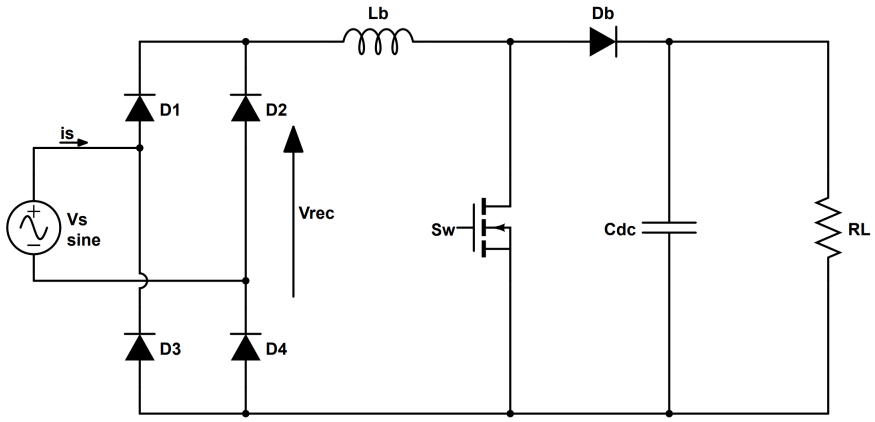

Figure 2.12: Rectifier with boost PFC stage.

2.4.1 Consequence of power factor correction

To ensure an efficient power transmission with low losses, it is important to compensate for different loads and achieve a unity PF [11]. In systems with a low PF the flow of reactive power is increased, leading to energy losses in terms of heat, decreasing the overall efficiency. Hence, by controlling the PF closer to one, the efficiency is increased. This means that by the implementation of PFC, equipment will operate more efficiently, reducing the energy consumption and extending the lifespan. Additionally, it is of importance to use PFC circuits correctly and not cause over-correction, which may cause voltage fluctuations, equipment damage and resonance issues.

Another issue regarding a PF distinct from one are the current harmonics [12]. They can cause serious problems like distorting the voltage in the system, making devices less efficient, and even harming nearby electronic devices connected to the main power supply. To deal with this issue, governments are setting regulations and controlling the amount of harmonics devices can emit [13]. Consequently, international standards like the IEC-61000-3-2 and IEC 1000-3-2 have been set. To meet the rules of the standards, the conducted emissions need to be limited, which can be done utilizing active PFC converters. As mentioned in 2.3, these converters include a PWM stage, placed between the bridge rectifier and the load. By using active PFC the power factor will be increased due to the reduced harmonics, showed in Figure 2.13, where the line voltage and current are presented as well as the reduced harmonic components [13].

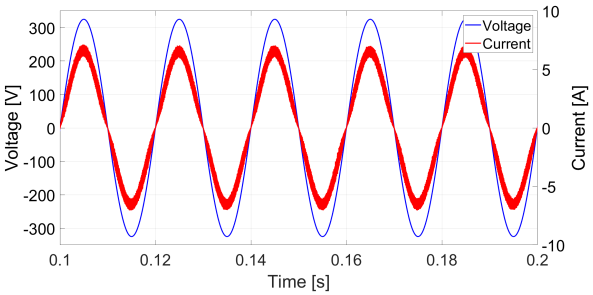

(a) AC voltage and current using an active AC/DC rectifier shown in Figure 2.12.

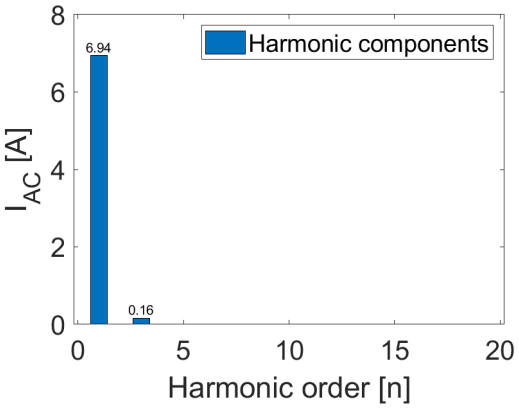

(b) Current FFT spectrum using an active AC/DC rectifier shown in Figure 2.12.

Figure 2.13: Active PFC converter with its waveforms of current and voltage and the harmonic spectrum.

2.4.2 CCM

The continuous conduction mode, CCM, is an important operation mode for different switching components in electrical devices [14]. In this operating mode the inductor in the circuit never gets fully discharged during a switching cycle. Instead, the inductor continues to conduct current during the cycle, which results in a more controlled and stable power/energy conversion from input to output.

This approach controls the current through the inductor, preventing it from reaching zero during a switching cycle [14]. By maintaining the current above zero through the cycle, the loss of magnetic energy over the inductor is reduced, leading to more efficient operation with less EMI. The CCM operation of the converter is shown in Figure 2.14.

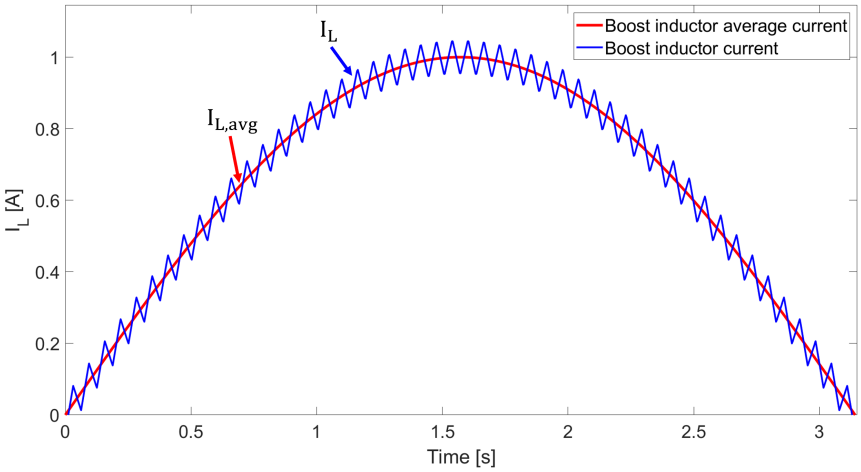

Figure 2.14: Inductor current for CCM operation, actual value and average.

To ensure CCM mode it is important to consider the component values in the circuit together with the switching frequency. One parameter is the ripple factor, k_{ripple}, which quantifies the peak to peak inductor current in relation to the average current [15], given as

$$k_{ripple} = \frac{\Delta i_{Lmax}}{i_{L,avg}} \tag{2.15}$$

This parameter influences the currents flowing through both the input and output capacitors in the PFC boost conversion stage. A typical value for the k_{ripple} parameter is around 20-40 % of the average input current [15, 16]. The boost inductor current in an non-interleaved PFC converter corresponds to the rectified line current as

$$\Delta i_{L,\max} = k_{\text{ripple}}\, i_{L,avg} \tag{2.16}$$

where $i_{L,avg}$ is calculated by

$$i_{L,avg} = |i_{in}| = |I_{in,pk} \sin(\theta)| \tag{2.17}$$

The θ is the phase angle where the maximum current ripple occurs. For a sinusoidal waveform this can be determined as

$$I_{in,avg} = \frac{2\sqrt{2}}{\pi} I_{in,RMS} \tag{2.18}$$

Subsequently the RMS and peak input current can be determined as

$$I_{in,RMS} = \frac{P_{out}}{\eta V_{in,RMS}} \quad ; \quad I_{in,pk} = \sqrt{2} I_{in,RMS} \tag{2.19}$$

From [4], it is given that the ratio between the output- and input voltage is

$$\frac{V_{out}}{V_{in}} = \frac{1}{1-D} \tag{2.20}$$

and with a duty cycle of $D = 0.5$ yielding the maximum current, the input voltage is given by

$$V_{in} = \frac{V_{out}}{2} \tag{2.21}$$

Additionally, V_{in} can be described as

$$V_{in} = V_{in,pk} \sin(\theta) \tag{2.22}$$

giving the angle, θ, where the maximum ripple occurs.

The voltage over the inductance could be expressed as

$$V_L = V_{in} = L \frac{\Delta I_L}{D T_s} \tag{2.23}$$

which by using (2.21) and setting $D = 0.5$ gives the minimum inductance value for a CCM operation

$$L_{CCM} \geqslant \frac{V_{out}}{4 \Delta i_{L,\max} f_{sw}} \tag{2.24}$$

2.5 Interleaved AC/DC with boost PFC converter

The interleaved power factor correction circuit, seen in Figure 2.15, is a power supply circuit that uses multiple parallel boost-converters working in phase [17]. This configuration divides the total input current into multiple currents and treating them separately, in parallel. The interleaved arrangement therefore lowers the load on each separate converter, improving the system's performance and efficiency. Components like the DC-bus capacitor, MOSFETs, and diodes are sized for lower current ripple [17], resulting in higher power density.

In addition to the lower operational current in the interleaved state, each individual converter can operate at a lower switching frequency [18]. This could lead to smaller and more cost effective input filter components and EMI filtering. To ensure the safe operation of the interleaved PFC boost converter, it is important to phase shift the converters operation to avoid collisions and unwanted noise [19]. This can be achieved by a sufficient control strategy and signaling to synchronise their operation, described more in section 2.6.

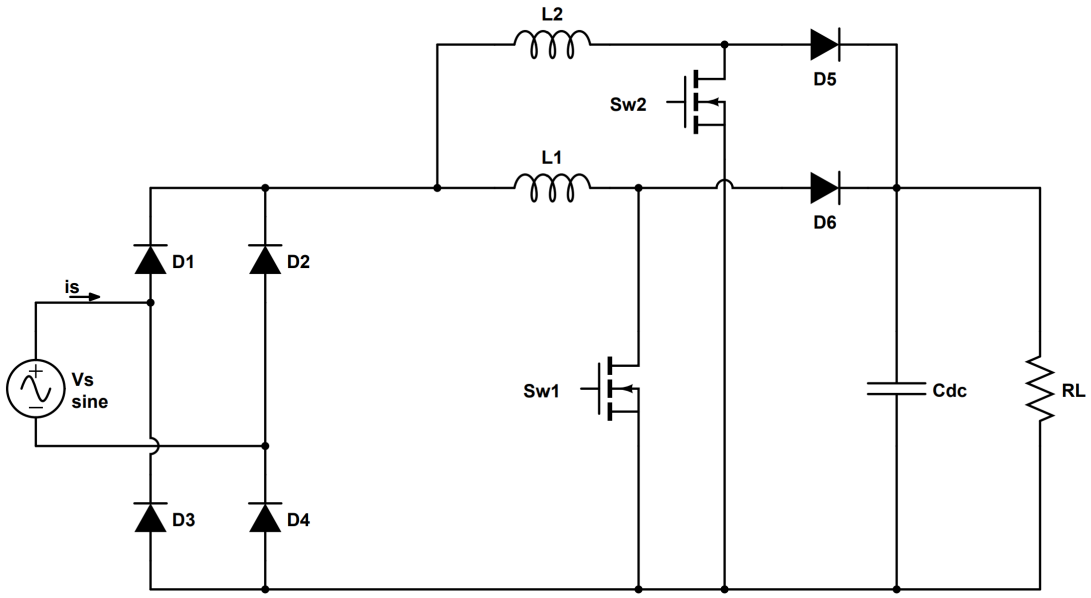

Figure 2.15: Interleaved AC/DC converter with PFC boost stage.

One important advantage with the interleaved operation, shown in Figure 2.15, is the current ripple cancellation [20]. In Figure 2.16 the on and off stages for the switches are showed, Sw_1 and Sw_2, as well as the rectified input current, I_L, and current waveforms, I_{L1} and I_{L2}.

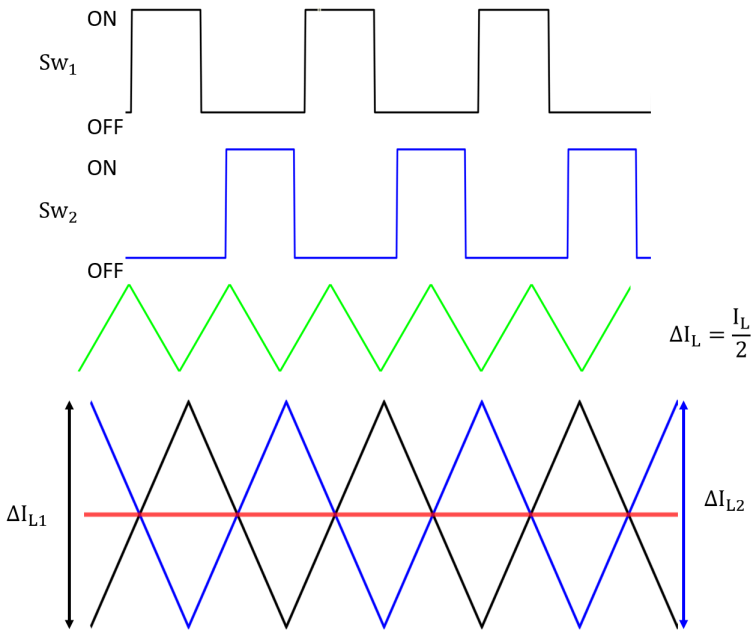

Figure 2.16: Interleaved boost stage, on/off switch signal and the resulting inductor current waveforms.

A parameter that demonstrates this is the cancellation factor, K_C, which compares the ratio between the interleaved ripple magnitude to the single phase ripple magnitude [20]. It is therefore defined as

$$K_C = \frac{\Delta I_L}{\Delta I_{L1}} \tag{2.25}$$

The cancellation factor can be reformulated, based on the duty cycle, D, depending on whether it is greater than, equal to, or less than 50 %, as

$$K_C(D) = \frac{1-2D}{1-D} \text{ if } D \leqslant 0.5 \tag{2.26}$$

$$K_C(D) = \frac{2D-1}{D} \text{ if } D > 0.5 \tag{2.27}$$

Because of the duty cycle variation in the PFC converter, the cancellation of the current ripple does not occur in every part of the cycle [20]. Multiple interleaved cells could therefore be used to reach the maximum amount of current ripple cancellation. Figure 2.17 shows cancellation factor for one and two interleaved cells, in regards to the duty cycle. It could be concluded that at a duty cycle of 50 %, D = 0.5, the interleaved operation with two cells theoretically results in a ripple free current.

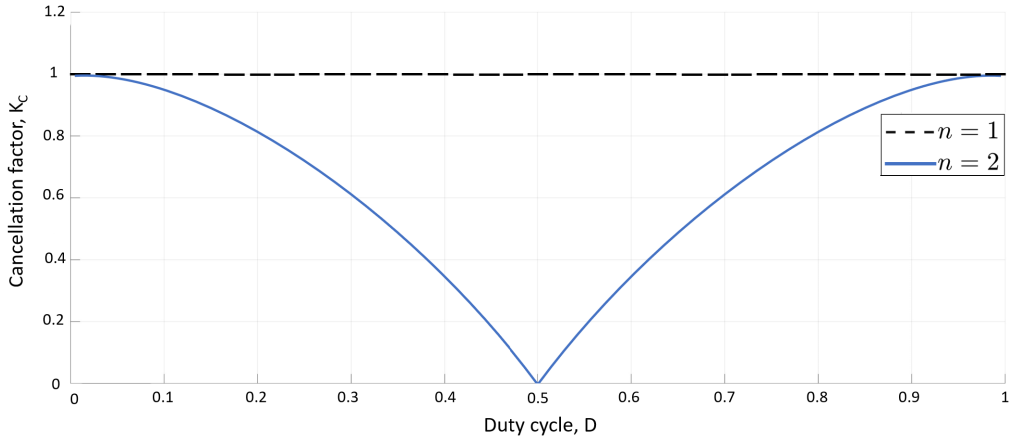

Figure 2.17: Cancellation factor in regards to duty cycle for one and two interleaved cells.

Another relevant aspect to consider in an interleaved cell is the energy stored in the inductor [20], given by

$$E = \frac{1}{2}LI^2 \tag{2.28}$$

Because of the interleaved operation, the input current is divided between the two parallel inductors, resulting in

$$E_{\text{int}} = \frac{1}{2}L_{int}\left(\frac{I_{in,RMS}}{2}\right)^2 + \frac{1}{2}L_{int}\left(\frac{I_{in,RMS}}{2}\right)^2 = \frac{1}{4}L_{int}I_{in,RMS}^2 \tag{2.29}$$

It should be noted that in order to maintain a constant energy storage, in regards to an non-interleaved cell, the inductance of each interleaved cell should be doubled

$$L_{int} = 2 \cdot L_{single} \tag{2.30}$$

2.5.1 Capacitor- and inductor design

In the interleaved converter the parameter calculation for the output capacitor design [21], is stated as

$$C_{dc} \geqslant \frac{2P_{out}t_{hold}}{V_{out}^2 - V_{out,min}^2} \tag{2.31}$$

where t_{hold} is the holdup time and $V_{out,min}$ is the minimum output voltage. This encompasses the capacitors time to maintain the desired output voltage within the acceptable voltage range for a certain duration. Consequently, the capacitance value is also affected by the load. Increasing the load demand requires a higher capacitance to guarantee the necessary voltage- and current output.

The inductance value is determined in a similar way as in section 2.4.2. The inductance equation stays the same as in (2.24) for the non-interleaved case, while the input current is halved. This due to the current distribution between the inductors, giving

$$I_{L,avg,int} = \frac{I_{in,pk}}{n} \sin(\theta) \tag{2.32}$$

The average inductor current, $I_{L,avg,int}$, is calculated as the peak input current, $I_{in,pk}$ divided by the number of interleaved phases, n. This consequently gives

$$L_{CCM,min} = \frac{V_{out} D(1-D)}{f_{sw} \Delta i_{L,\max}} \tag{2.33}$$

This implies that with increased output power (increased current), the required inductance value to keep the converter in CCM decreases, assuming all other parameters remain constant. This occurrence is attributed to that the inductor experiences a higher ripple at higher power demands, due to an increased average inductor current, seen from (2.16). Conversely, at a lower power, the inductance to keep the converter in CCM increases.

2.5.2 Power losses, interleaved PFC

The power losses in the interleaved circuit, Figure 2.15, could be categorized as bridge rectifier losses, conduction losses and switching losses [17]. The losses in the bridge occur in the diodes due to their forward voltage drop as the diodes are conducting, and can be estimated by

$$P_{diode} = V_{th} I_{in,avg,BR} + R_{diode} I^2_{in,RMS,BR} \tag{2.34}$$

where V_{th} is the threshold voltage, $I_{in,avg,BR}$ is the average current through the bridge rectifier, R_{diode} is the dynamic resistance of the diode and $I_{in,RMS,BR}$ is the RMS current through the bridge rectifier. The input current RMS value, $I_{i,in,RMS}$ is determined as

$$I_{in,RMS} = \frac{P_{out}}{\eta V_{in,RMS}} \tag{2.35}$$

The total bridge rectifier losses are therefore

$$P_{BR} = 4 P_{diode} \tag{2.36}$$

Conduction losses are also present due to the resistive elements of the components. The switching conduction losses, $P_{S_{cond}}$, could be determined as

$$P_{S_{cond}} = D V_{ce,sat} I_c \tag{2.37}$$

and the diode conduction losses, $P_{Di_{cond}}$, as

$$P_{Di_{cond}} = (1-D) I_f V_f \tag{2.38}$$

This gives the total conduction losses of

$$P_{cond,total} = P_{S_{\text{cond}}} + P_{Di_{cond}} \tag{2.39}$$

The switching losses, arising during the transition between the on- and off states, are determined by

$$P_{sw} = f_{sw} \left(E_{on} + E_{off} \right) \tag{2.40}$$

During the on-time, the energy dissipation, E_{on}, is given as

$$E_{on} = \frac{t_{on}}{2} I_{c,pk} V_{ce,pk} + Q_{rr} V_{ce,pk} \tag{2.41}$$

where the $I_{c,pk}$ is the peak collector current, $V_{ce,pk}$ is the peak collector emitter voltage. The Q_{rr} is the reverse recovery charge that puts stress on the components upon switching, which is determined by

$$Q_{rr} = \frac{1}{2} t_{rr} I_{rr} \tag{2.42}$$

Naturally, t_{rr} is the reverse recovery time and I_{rr} is the reverse recovery current. The energy dissipation at the off state, E_{off} is determined as

$$E_{off} = \frac{t_{off}}{2} I_{c,pk} V_{ce,pk} \tag{2.43}$$

2.6 Control structure, interleaved PFC

Figure 2.18 represents the block diagram of the interleaved AC/DC with the PFC- and control stage [17, 19]. The goal of the PFC controller is to achieve both low line current distortion, resulting in a high PF, and a precise output voltage regulation. The control method for achieving this is the average current mode control, ACMC [19]. It operates on the principle of regulating the mean value of the current through each inductor and controlling it to be proportional to the rectified input voltage. Consequently, this regulation ensures that the line current corresponds to a sinusoidal waveform and remains in phase with the line voltage, shown in Figure 2.13a. This control strategy is dependent on monitoring the inductor currents, i_{L2} and i_{L3}, the output voltage, V_{out} and the rectified line voltage, V_{INAC}, seen in Figure 2.18.

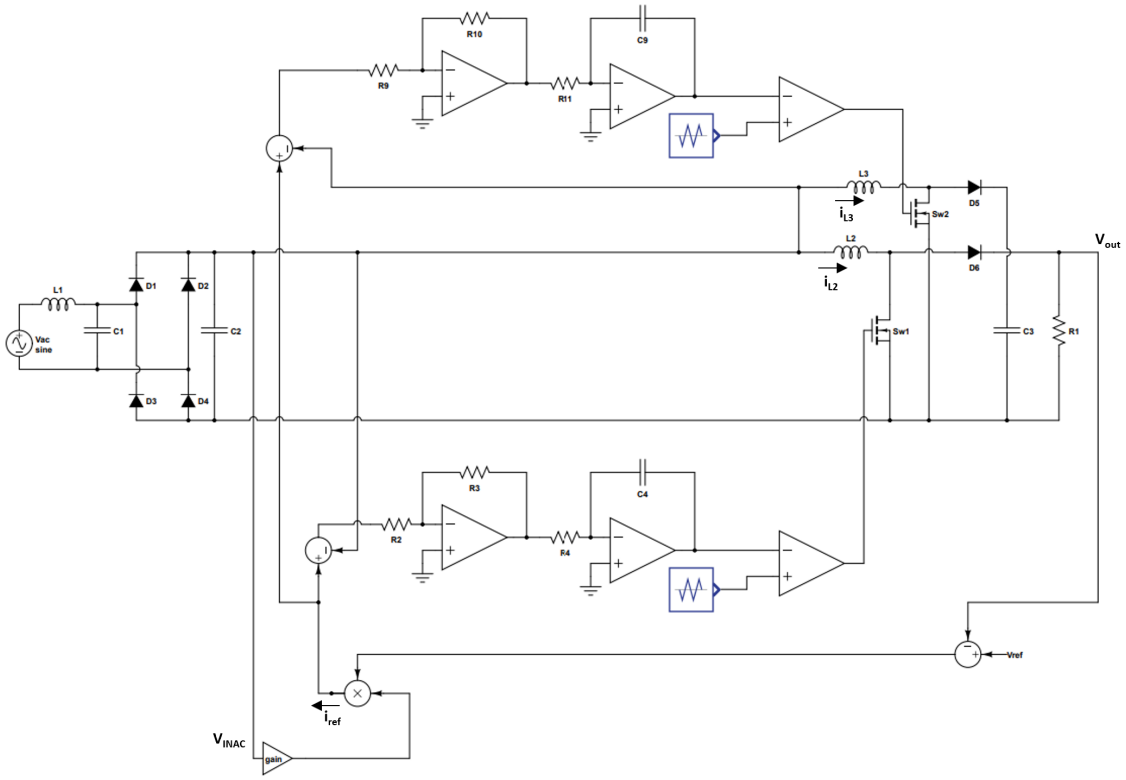

Figure 2.18: Schematics of the control strategy for the interleaved AC/DC converter.

A cascade controller is a control system that uses two interconnected control loops, where the primary loop provides a setpoint for the secondary loop [22]. For the interleaved case, the cascaded controller consist of two inner loops, regulating the current, and one outer loop, regulating the voltage [23]. This improves the control performance and enhances the stability of the system. The two inner loops are used for controlling the input current to achieve a high power factor [23]. The bandwidth of the loops is high to get a fast response, due to the rapidly changing input current. The outer loop is instead used for regulating the DC voltage. Here, the bandwidth is low and the response is therefore slow, due to that it focuses on the slower-changing output voltage. The outer loop does not therefore need to react as quickly as the inner loop. Its main job is to maintain a steady output voltage for the converter, even with changes in load or input voltage. A slower response here is acceptable because the voltage does not fluctuate as much as the current. The result is a control strategy that offers inherent stability across a wide range of operating conditions, making it well-suited for applications demanding high performance and reliability. One should also note that the inner current loop bandwidth should be much higher than the bandwidth of the outer voltage controller in order to avoid interactions between the control loops and maintain stability [24].

2.6.1 Current controller design

In the current controller the current through each inductor is initially sensed. The sensed current is then averaged over a complete switching cycle to eliminate the high-frequency ripple component. Next, this averaged current value is compared to a reference current signal, i_{ref}, see Figure 2.18. This reference current is generated based on the desired input power and the AC mains voltage. By controlling this reference current, the shape of the input current waveform is indirectly influenced. The goal is to achieve a sinusoidal and in-phase current that aligns perfectly with the AC line voltage, thus achieving a PFC effect. Finally, the difference between the sensed average current and the reference current is utilized to adjust the duty cycle of the PWM signal driving the switch in each boost converter.

Fundamentally, the controller increases the duty cycle if the sensed current falls below the reference current [23]. If the sensed current is higher than the reference, the duty cycle is decreased. This feedback loop ensures that the average input current of each stage tracks the reference, ultimately shaping the overall input current waveform to the converter. By modulating the duty cycle in response to variations in the input or output conditions, the average current mode controller effectively regulates the power transfer. This in turn ensures efficient utilization of energy and reduces distortions in the input current waveform. Another feature when using the ACMC is the possibility to detect irregularity or overloads early, which in turn can be used as a safety function to mitigate errors and faults of the converter [25].

A PI controller that satisfies the CCM current controller requirements is obtained though

$$G_{c1}(s) = G_{c2}(s) = K_{p,c} + \frac{K_{i,c}}{s} \tag{2.44}$$

where $K_{p,c}$ is the proportional gain and $K_{i,c}$ is the integral gain for the current controller [24]. To avoid aliasing, the sampling period is chosen in accordance to the Nyquist Theorem, as

$$f_s \geq 2f_{max} \tag{2.45}$$

where f_s is the sampling frequency and f_{max} is the maximum frequency in the system [26].

When the input sine wave's inherent symmetry is combined with average current mode control, even harmonics are significantly reduced or canceled [4]. For every positive half-cycle, there is a corresponding and identically inverted negative half-cycle in the original waveform. The more closely the input current of the converter matches a sine wave, the more effective the cancellation of the even harmonics is. Specifically, if the duty cycle approaches 50 %, the input current more closely resembles a sine wave, enabling the controller to more accurately detect the average current and enhance the cancellation of even harmonics.

2.6.2 Voltage controller design

In the voltage loop the sensed voltage is compared to a predetermined reference voltage V_{ref}, seen in Figure 2.18. The difference between the sensed voltage and the reference voltage serves as the control signal. This signal is used to adjust the reference current signal provided to the inner current loops. By increasing the reference current, the average current flowing through the inductors increases as well, consequently boosting the output voltage.

In contrary, decreasing the reference current leads to a lower output voltage [23]. The outer loop acts as a main controller, continuously ensuring that the converter maintains the desired output voltage level. It achieves this by fine-tuning the inner current loops. Even in the presence of variations in the input AC voltage or load current, the outer loop ensures the converter delivers a stable output voltage [25]. The voltage loop needs to operate at a low bandwidth to reduce distortion in the line current. However, it is crucial for the controller to respond quickly to changes in the output voltage reference, especially during load variations. Given the presence of a second harmonic component, 100 Hz, in the output voltage, the bandwidth of the voltage controller is typically limited to a maximum of 20 Hz [10].

A PI controller that satisfies the CCM current controller requirements is obtained though

$$G_v(s) = K_{p,v} + \frac{K_{i,v}}{s} \tag{2.46}$$

where $K_{p,v}$ is the proportional gain and $K_{i,v}$ is the integral gain for the voltage controller [24].

2.7 AC/DC converter utilizing the UCC28070 controller

The controller utilized in this project was the UCC28070 from Texas Instruments. It was selected due to its availability and accessibility of the control parameters. This allowed for modifications to the controller to obtain the desired power factor.

The UCC28070 is an PFC controller, using an interleaved operation that integrates two PWM signals which operate 180 degrees out of phase [27]. This interleaved operation results in a reduction of input- and output current ripple, which makes the EMI filtering easier to handle. The UCC28070 promotes performance enhancements in PF, efficiency, transient response and THD. It also implements multiple protection and safety features, including a over-voltage detection at the output, a peak current limit and a open loop protection. Furthermore, Texas Instruments has developed an AC/DC Evaluation module, designed for 300 W utilizing the UCC28070 controller [28]. It consists of a motherboard, Figure 2.19, and a daughterboard, Figure 2.20, linked through the connection port J1. In this chapter, key functions of the UCC28070 and its EVM kit will be presented, for additional information see

respective datasheet [27, 28].

In Figure 2.19 the motherboard of the EVM kit is presented, where the passive rectification and power stages are implemented. Some of the key components are highlighted.

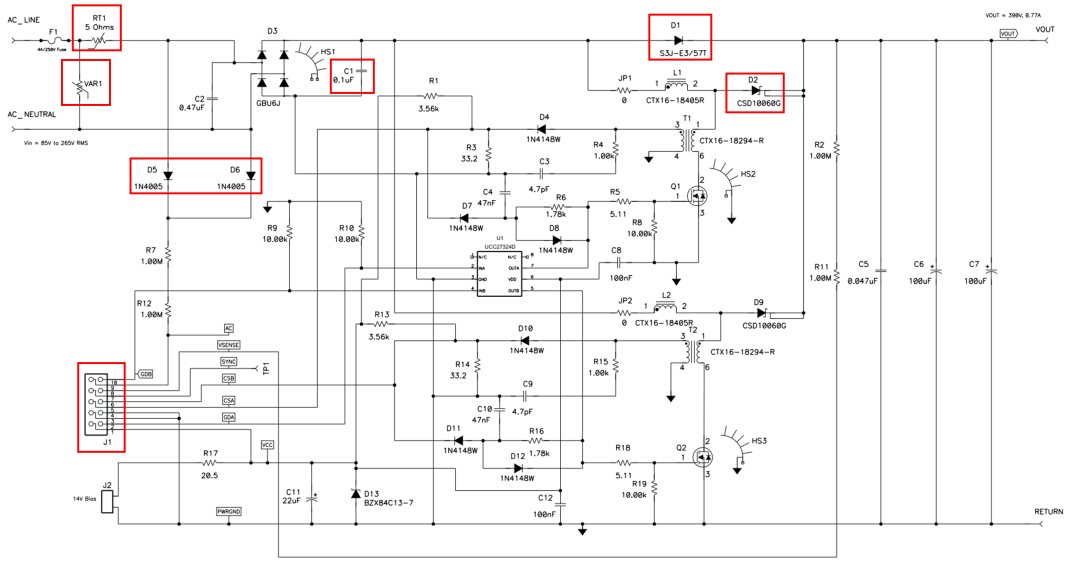

Figure 2.19: Motherboard of UCC28070EVM [28]. Reprinted with permission.

The motherboard is responsible for rectifying the alternating voltage and ensuring reliable power delivery to the components. The rectification occurs within the diode bridge, working in conjunction with the capacitor, C1, to filter the signal, resulting in a DC output. Simultaneously, to ensure an accurate signal measurement to the controller a separate half bridge, consisting of diodes D5 and D6, is used without a capacitor. This is due to that a direct measurement immediately after the full diode bridge (D3) would result in inaccuracies due to damping by the EMI capacitor, C1.

Two diodes are also present at the output side of the motherboard, D1 and D2. The first one, D1, is a Schottky diode and is used during the startup, while the output capacitors (C6 and C7) are being charged, and during possible transients. The aim of this is to ensure safe operation for the other diode, D2, which is made out of silicon carbide and cannot handle as high currents. This diode is used to reduce the reverse recovery losses, as it offers low reverse recovery currents and short reverse recovery times.

Other important components in the motherboard are the resistor, RT1, and the varistor, VAR1. The resistor, RT1 limits the inrush currents, which are the initial high currents occurring during startup. The varistor, VAR1, plays an important role by controlling the voltage transients. When the voltage level suddenly increases, due to for example disturbances in the grid, the varistor absorbs the excess voltage, stabilizing the voltage level. Both of these components therefore act as protection for

the circuit, ensuring that the startup phase is handled correctly and that the circuit is not being overloaded. Additionally, there is also a glass cartridge fuse on the motherboard, protecting against overcurrents and short circuits.

In Figure 2.20 the daughterboard of the EVM kit is presented, consisting of the control circuitry for the active PFC stage.

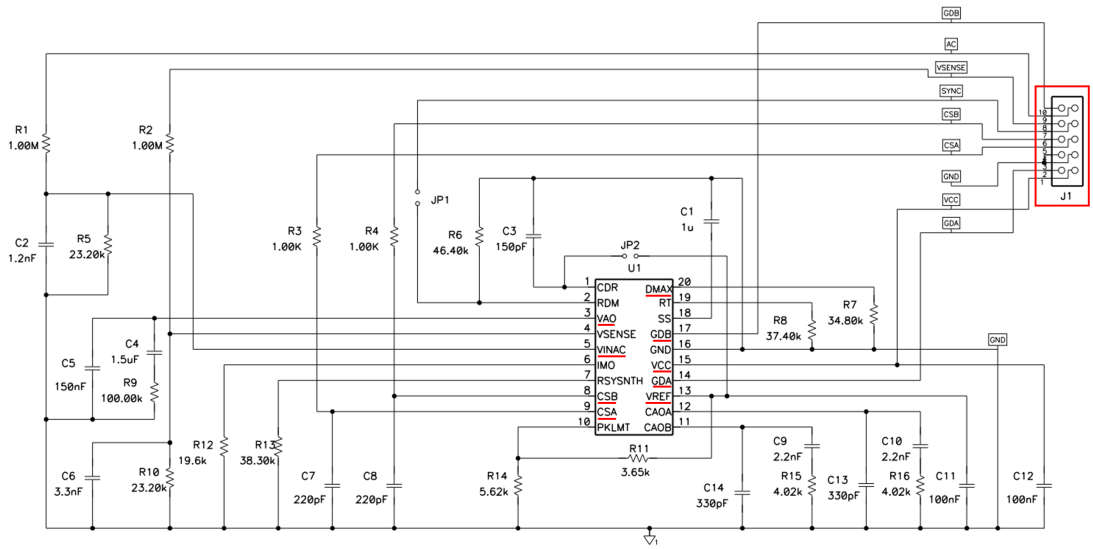

Figure 2.20: Daughterboard of UCC28070EVM [28]. Reprinted with permission.

In Figure 2.20, some important pins of the controller are highlighted. CSA and CSB are used for measuring the current for the two phases. In the same way, GDA and GDB are used to control the two different switches. The pin DMAX sets the maximum duty cycle and VREF is the reference voltage and the internal bias voltage. VCC supplies the output bias voltage. VINAC is the scaled AC line input voltage that is connected to the multiplier, affecting the phase shift. VAO is the voltage amplifier output, used to amplify the error between the desired voltage and the actual voltage. These pins combined mainly set the control for the active PFC circuit. The complete block diagram for the daugheterboard is presented in Figure A.10.

The equations specific to the design of the converter using the UCC28070 differ from the general equations presented in section 2.5.2. These variations are due to the characteristics of the UCC28070. All of the following equations originate from [28].

The capacitor design accounts for the holdup time and is determined by

$$C_{out} \geq \frac{\frac{2P_{out}}{f_{Line}}}{{V_{out}}^2 - (0.75V_{out})^2} \tag{2.47}$$

The inductor value is defined by

$$L_1 = L_2 = \frac{V_{in_{min}}\sqrt{2}D_{PLL}}{\Delta I_L \cdot f_s} \tag{2.48}$$

where the D_{PLL} is the converter's duty cycle at the peak of low line operation. This is described as

$$D_{PLL} = \frac{V_{out} - V_{in_{min}}\sqrt{2}}{V_{out}} \tag{2.49}$$

The conduction- and switching losses are calculated by

$$P_{M_{cond}} = \left(\frac{0.5P_{out}}{\sqrt{2}V_{in_{min}}} \sqrt{2 - \frac{16}{3\pi}\frac{\sqrt{2}V_{in_{min}}}{V_{out}}} \right)^2 R_{DS(\text{on})} \tag{2.50}$$

$$P_{M-sw} = \frac{1}{2} f_{sw} \left(V_{out} \, \frac{I_{line,max}}{2} \left(t_r + t_f\right) + C_{oss} V_{out}^2 \right) \tag{2.51}$$

Lastly, the bridge rectifier loss is estimated by

$$P_{BR,max} = 2V_F I_{n,avg,max} \tag{2.52}$$

2.8 EMI and EMC

Electromagnetic interference, EMI, and electromagnetic compatibility, EMC, are two important concepts regarding electrical components and their performance [29]. EMI refers to disturbances that affect the performance in an electrical device or system due to electromagnetic radiation och conduction from an external source. This interference can impact the normal operation, leading to errors, defects and other unwanted effects. On the contrary, EMC denotes the ability of an electronic device to endure such interference and operate correctly without causing disruption to other devices. This could entail designing the electrical devices with considerations for filtering, grounding and shielding among other protective measures.

2.8.1 Types of emissions

When looking at EMI and EMC there are different types of emissions to consider [29]. Conducted- and radiated emissions, are both mainly cased by switching events and high frequency signals. The conducted emissions refer to electromagnetic radiation going though cables and wires. This results in interference with the operation of other electronic equipment connected to the same power or signal lines. Radiated emissions are instead manifested as electromagnetic waves. Furthermore, there are transient emissions, descending from abrupt changes in voltage or current within a system, often due to turn on and off [29].

Two other types of emissions, significant to electrical devices are common mode,

CM, emissions and differential mode, DM, emissions [29]. These are generally considered when designing an input filter. The DM noise is the voltage difference between the supply line and return line in the circuit, see Figure 2.21. This noise is mainly prevalent due to the switching events taking place in the device and is directly affecting the circuit components. As for the CM noise, it is usually shown as the voltage transient between supply lines and ground, becoming uniform to all lines in regards to ground.

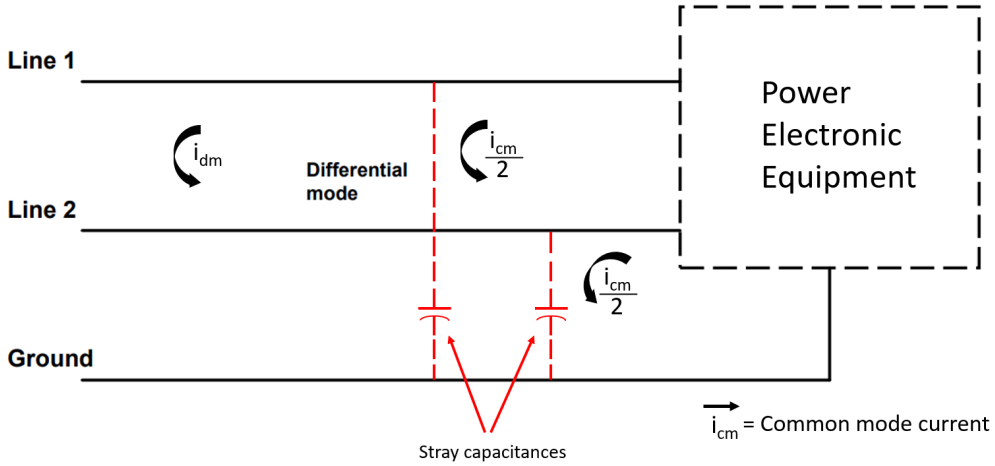

Figure 2.21: Conducted interference, DM and CM.

2.8.2 EMI standards

There are different types of standards such as CISPR, IEC, VDE and FCC that specify the maximum limit of conducted EMI [4]. To asses the conformity between these limits the conducted EMI is measured with an Line Impedance Stabilization Network, LISN. This establishes an standardized testing environment and providing accurate measurements. Through following these standards, manufacturers can guarantee that their products meet the regulatory requirements, ensuring electromagnetic compatibility and minimizing unwanted interference in electrical systems [30].

In Figure 2.22 the CISPR 32 standard is presented for main ports, which applies to multimedia equipment with a supply voltage not exceeding 600 V, whether it is AC or DC [31]. The standard ensures that the multimedia equipment does not generate electromagnetic interference, affecting other equipment, and it is immune to the interference present in its intended environment. In the standard there are two defined classes, as shown in Figure 2.22, class A and class B. Class A addresses equipment intended for commercial or industrial use, usually with higher levels of emissions, while Class B is for residential environments with stricter requirements [29]. Within respective class there are two different measurement parameters, average, AVG, and quasi peak, QP. The average measurement method addresses the average emissions over a specific frequency spectra, while the quasi peak treats short term repetitive peaks.

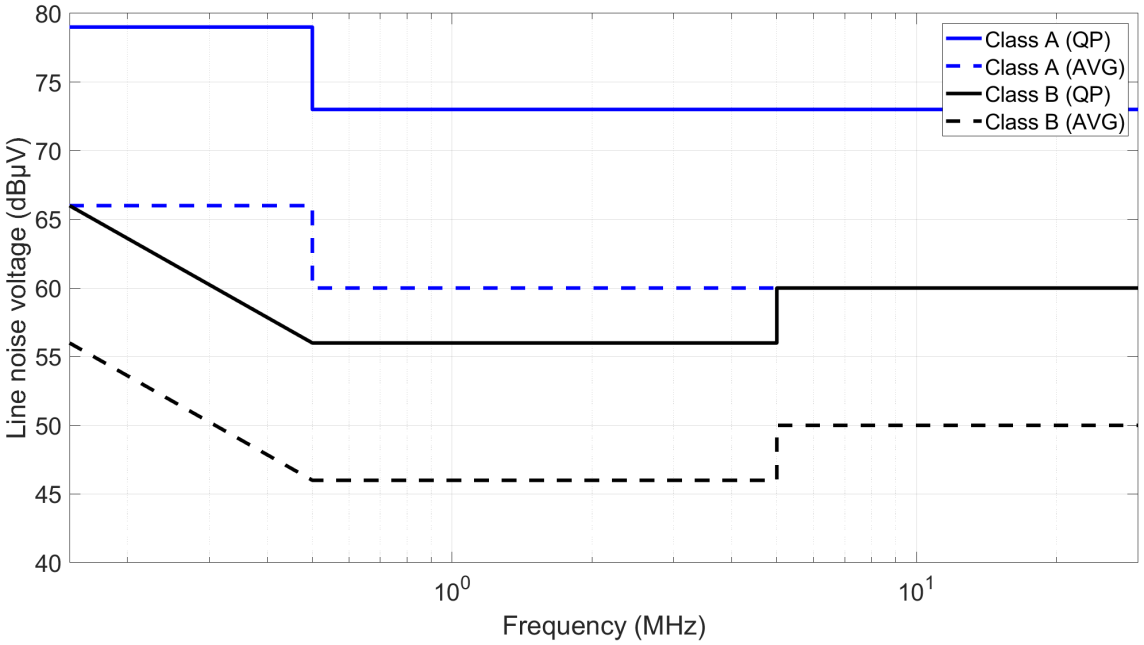

Figure 2.22: Conducted Emission levels as per CISPR 32 standards for main ports.

2.8.3 Standards applicable to AC/DC converters

To ensure reliable and compliant AC/DC converters, following industry standards is necessary. Key standards include the IEC 61000 and IEEE 519-2022, that govern performance and electromagnetic compatibility for devices like AC/DC converters [32, 33]. For both standards, specific criteria are established regarding allowed levels of distortion, power factor, and overall power quality. By adhering to these standards, the converter maintains a clean and stable EMI profile, ensuring reliable operation and compliance with regulatory requirements.

The IEC 61000 consist of multiple standards, including IEC 61000-2-2 that specifies a maximum voltage distortion of 8 % for low frequency devices in public networks [33]. Therefore, when designing an AC/DC converter, the input voltage distortion must not exceed 8 %. The standard also sets a limit for each odd harmonic, where the maximum allowed distortion decreases as the harmonic order increases.

Another important standard to consider is the IEC 61000-3-2, which is a safety standard related to EMC [31]. It applies to equipment intended to be connected to public low voltage distribution systems with a maximum rated input current of 16 A per phase. The standard is divided into four classes, A-D, each with specific limits for accepted harmonic currents across different harmonics. In regards to section 2.7, the used converter is designed for 300 W, making class D relevant as it applies to equipment with a maximum power consumption of 600 W. In Table 2.1 the limits for the 15 first harmonic current components for class D are presented [31].

Table 2.1: IEC 61000-3-2 harmonic limits for the first 15 components (Class D).

Harmonic Order	Limits class D [A]
2	-
3	3.40
4	-
5	1.90
6	-
7	1
8	-
9	0.50
10	-
11	0.35
12	-
13	0.29
14	-
15	0.25
16	-

IEEE 519-2022 sets the standard for operating AC/DC converters safely and efficiently [32]. It establishes requirements to minimize electromagnetic interference and ensure proper function in different environments. According to the standard, the THD on the grid must not exceed 8 % for voltages below 1 kV. Additionally, no individual harmonic component should exceed 5 %.

On the DC-side, the regulations are dependent on the application. For instance, in a railway application the voltage ripple should not exceed 15 % [34], while DC power systems on ships should not exceed 10 % [35]. Devices connected through USB should not experience a ripple higher than 5 % [36].

Although, one should be careful when designing an electrical device as there are more standards to consider, and one of them being the IEC/EN 62368-1 [37]. This standard applies to audio/video-, information-, and communication technology equipment. It includes a wide range of products, covering computers, monitors, TVs, audio equipment, and other similar devices. In this standard there are safety requirements for electrical, mechanical, chemical and thermal hazards. By following this standard, the safety of the users can be ensured and the risk of accidents involving electronic devices is reduced.

2.9 Microcontroller

The microcontroller can be seen as an all-in-one solution for many calculation- and control needs [38]. It stands as a compact device, housed within a single integrated circuit, enabling the processing of data through various control algorithms. Although

its small size, it usually includes a processor, memory, input- and output ports, and a variety of different functions, enabling it to handle a diversity of tasks.

2.9.1 Arduino UNO R4 and LOLIND32

The two development boards used in this project, seen in Figure 2.23 are the LOLIND32 using an ESP32 controller and the Arduino Uno R4, utilizing a Renesas RA4M1 as a controller and an ESP32 for connectivity [39, 40]. This means that both boards offer integrated WiFi and Bluetooth connectivity due to the ESP32. They are compatible with the Arduino Integrated Development Environment, IDE, and provide an integrated USB to serial conversion, making uploading code from a computer easy. The development boards also provide multiple amount of pin connectors, enabling connection to various sensors and devices without the need of soldering. Additionally, the LOLIND32 offers a 8 bit digital to analog converter, DAC, while the Arduino Uno R4 utilizes a 12 bit DAC resolution.

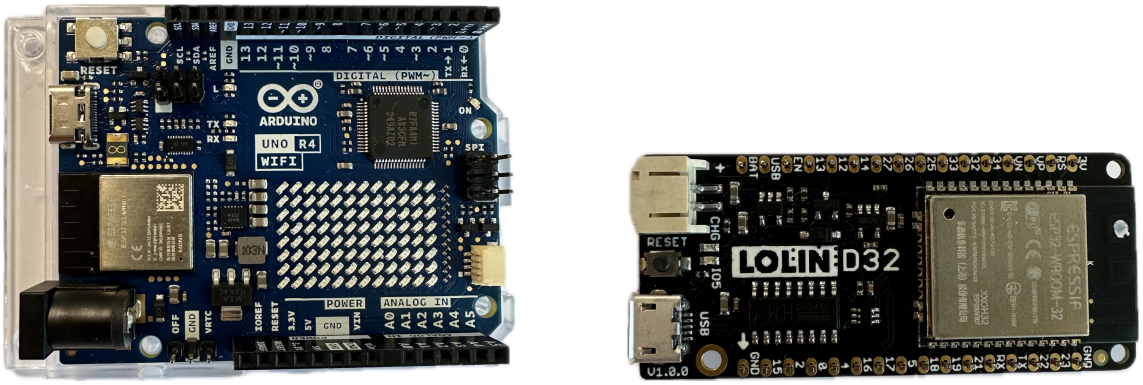

(a) Arduino UNO R4 WIFI. **(b)** Wemos LOLIND32.

Figure 2.23: The two different microcontrollers used.

2.9.2 Wi-Fi, Bluetooth and Modbus

The ESP32's built-in Wi-Fi and Bluetooth capabilities, coupled with the LOLIND32 and Arduino Uno R4, makes the modules excellent for crafting wireless IoT devices or sensors with seamless communication [41]. The ESP32 provides two Wi-Fi modes, station and access point [42, 43]. In the station mode the ESP32 connects to a Wi-Fi access point and works similarly to a computer, connected to a router. If the router has Wi-Fi, so does the ESP32. It can act as a client, initiating requests to other devices on the network, or as a server where it receives requests from other devices. In the access point mode, the ESP32 is transformed into a Wi-Fi network that is similar to a router, providing other devices to connect to it. In this standalone mode the ESP32 is not connected to another network and therefore lacks internet access.

The ESP32 also enables the use of Modbus communication, accessible through libraries on the Arduino platform [44]. However, both the LOLIND32 and the Arduino UNO R4 need to be connected to a separate communication unit, for example an Ethernet- or an RS-485 module. The modules could be used for reading and

transmitting data with other Modbus units. They could be programmed as either a Modbus slave or a Modbus master, enabling a wide variety of potential uses.

2.10 Electricity grid

In the world of power systems it is of great importance to strive for stability, reliability and efficiency in the electrical grid [45]. This is especially true with the increased implementation of renewable power sources, such as solar- and wind power, making the grid stabilization services of great importance.

To ensure smooth operation throughout the power grid, voltage regulation is a critical aspect [46]. It describes the system's ability to provide constant voltage over different load conditions. Another critical aspect to consider is the phase relation between the current and voltage. Therefore, phase compensation is of importance in the grid. By adjusting and optimizing the phase relations a better power flow could be achieved, which in turn gives the power system increased efficiency.

2.10.1 Swedish electrical grid infrastructure

In Sweden there is a well developed and diversified energy supply that includes multiple production sources as hydropower, wind power, nuclear power and solar energy [47]. Most of the large production facilities in terms of hydro- and wind power are located in the north of the country, due to the favorable conditions. In recent years the previous nuclear power plants, located in the southern part of the country, have been discontinued and closed [48]. This consequently lead to difficulties in regards to the distribution system, with most of the energy production in north and most of the energy consumption in south.

The Swedish grid infrastructure can be divided into different levels [49], shown in Figure 2.24. Following the energy production, the distribution of high voltage electricity goes through the transmission grid. Svenska Kraftnät is the state owned company responsible for the transmission grid, which enables transfer of large amounts of electricity over long distances.

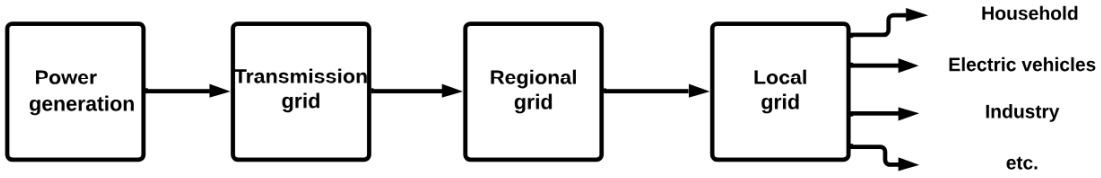

Figure 2.24: Sectioning of the Swedish grid, divided in transmission-, regional- and local grid.

Regional grids receive the electricity from the transmission grid and distribute it

through transformer stations to local networks [49]. These grids are administered by multiple companies, including for example Vattenfall, ensuring that the electricity is accommodating the demand in cities and industrial areas.

Lastly, there are the local distribution networks, which are responsible for delivering the electricity from the regional grids to for example households and businesses within a specific geographical area. These grids could either be municipal or private, and consist of transformers, distribution lines and other components to distribute electricity to consumers.

2.10.2 Evolving grid services

The need for different grid services is constantly increasing as more renewable energy sources are implemented in the electrical grid [45]. These could involve balancing the supply and demand, controlling the frequency and regulating the voltage. Simultaneously, the electricity market is undergoing a change with a relaxation of regulations and the supply chain being divided into various segments [50]. This encourages companies to offer more efficient and affordable services to consumers. By dividing the market into these segments, competition increases because no monopoly is in control. Additionally, deregulation supports this by encouraging flexibility and innovation, reducing government barriers in the electricity market. This encourages new companies to enter the market, contributing to the rise of renewable energy sources, and advancements in smart grid technologies. There is a push to optimize each part of the electricity supply chain, ultimately making the market more focused on the needs of consumers.

One way of doing this is with demand response programs, which can be seen as part of the evolving grid services. These programs enhance grid flexibility by providing services to quickly change the load, therefore supporting the integration of renewable energy sources [51]. With the decentralization of the grid, consumers are becoming more active participants. This is due to increase of distributed energy sources, such as solar panels, electric vehicles and energy storage systems, complementing the demand response efforts. These the smart grid technologies facilitate more effective demand response, it is of importance to implement a real-time communication and control. It could be achieved by different time based rates and incentive-based programs [51].

2.10.3 Ericssons Base stations

Within telecommunications, a base station is a device that provides coverage within a specific region, essentially functioning as a cell phone tower that connects devices to the network [52]. These towers require a constant electricity supply from the Power Supply Unit, PSU, to operate effectively. As of today, Ericsson's network is divided into multiple base stations, each equipped with multiple single phase AC/DC PSUs and a battery [50], as illustrated in Figure 2.25. The battery serves as a backup power source that sustains the base station for several hours in the

event of a grid connection failure. The duration is dependent on the regulatory requirements. During this time, most operators should be able to activate their backup generators and restore power.

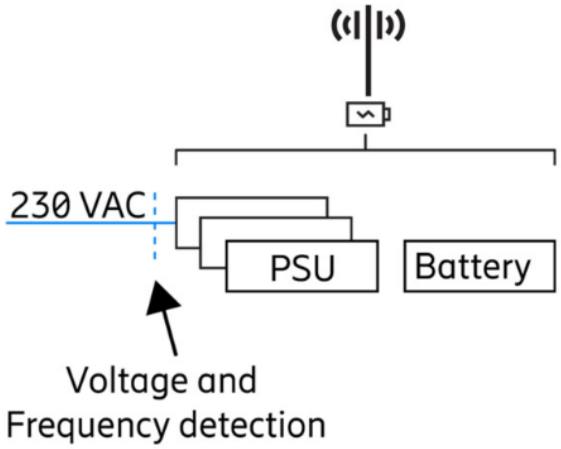

Figure 2.25: Base station with PSU and battery [50]. Reprinted with permission.

Expanding on this, Ericsson's AC/DC converters within the base stations can be synchronized with the Swedish Transmission System Operator, TSO, [53]. The TSO emits a clock signal that represents the frequency, which could guide the adjustment of the power factor in the converters. This synchronization enables the converters to dynamically adjust their operation in response to changes in the grid frequency and load demand. Consequently, during peak demand periods, the converters can adjust their PF to ensure efficient energy utilization. This capability offers a method for enhancing grid stabilization services.

3
Case Setup

This chapter introduces the constructed simulation model together with the design and assembly process of the prototype. Additionally, it outlines the essential tests conducted to assess the prototype's functionality and compliance with the grid stabilization requirements. The integrated circuit, IC, that has been used is the UCC28070 together with its evaluation kit, UCC28070EVM, which is an AC/DC converter solution specified for 300 W.

3.1 Simulation

A behavioral model of the interleaved boost AC/DC PFC converter has been created using LTspice. The model draws inspiration from the UCC28070EVM and is generally based on the same control structure, ACMC. It serves as a tool in validating the theoretical feasibility of the first research question, presented in 1.3.1, of an possible AC/DC converter solution. The simulation behaviour was conducted for three different values of phase shift: 0°, 30°, and 60°. This was done for half power, 150 W, and for full power, 300 W. In Figure 3.1 the interleaved AC/DC PFC model is presented.

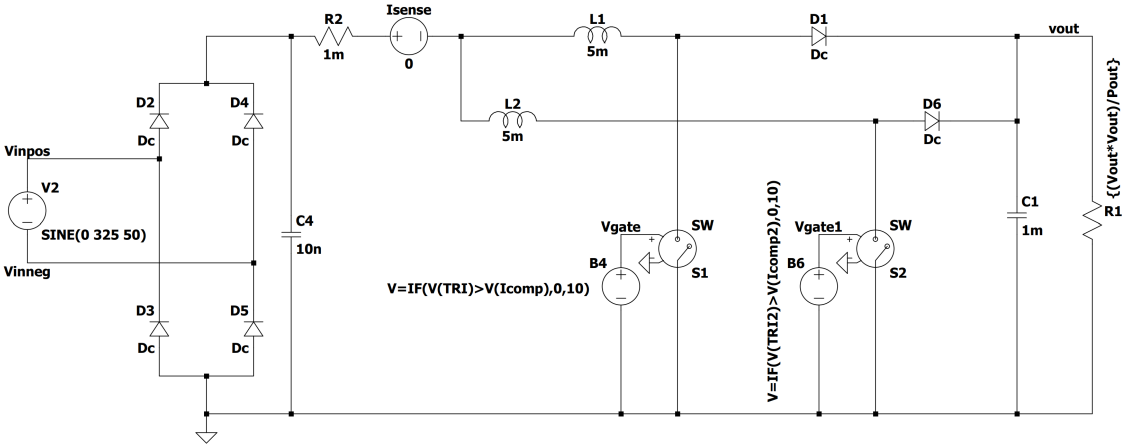

Figure 3.1: Schematics over the simulation model. Behavioural model of interleaved AC/DC with PFC.

The parameters used in the simulation are presented in Table 3.1.

Table 3.1: Simulation parameters.

Parameter	Value
f	50 Hz
V_{in}	230 V
V_{out}	390 V
P_{out}	150/300 W
F_{sw}	150 kHz

In Figure 3.2 the control structure of the behavioral model is presented.

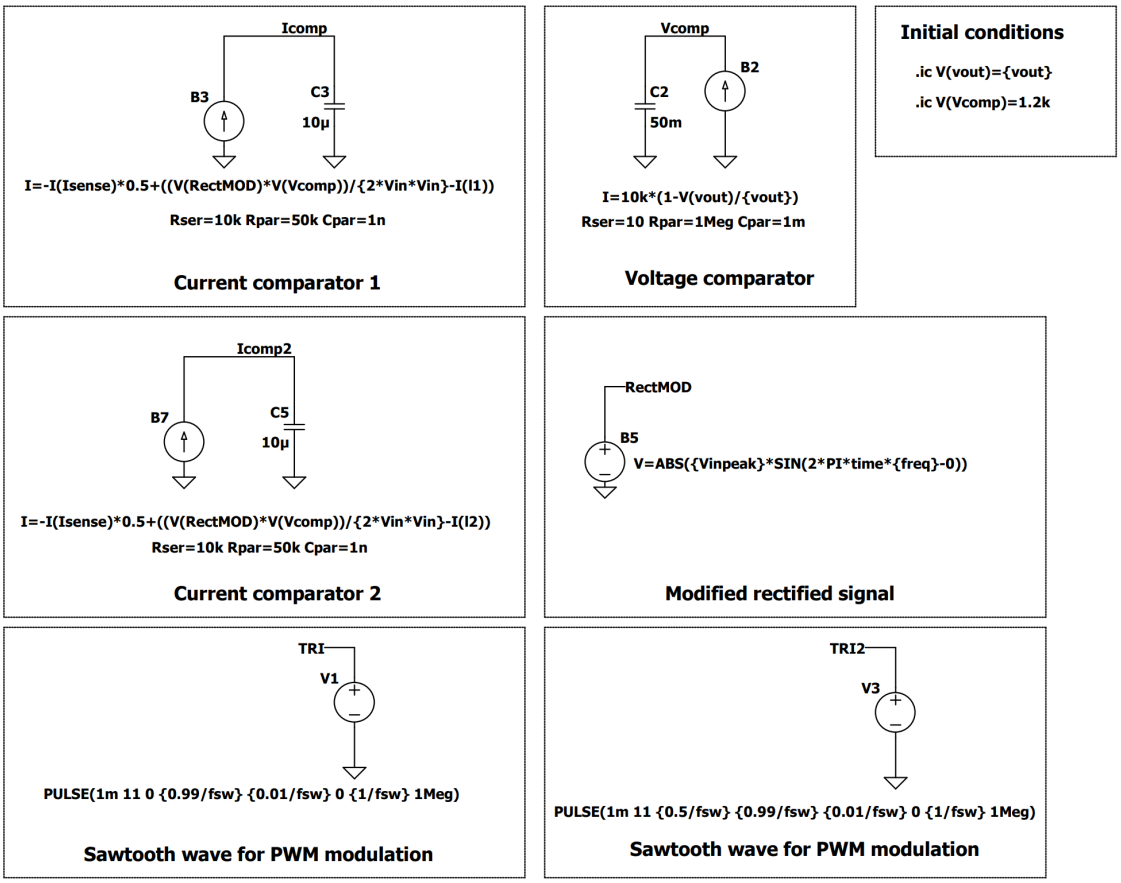

Figure 3.2: Control network consisting of voltage comparator, current comparators, sawtooth signals, modified rectified signal and initial conditions for the simulation.

The model bases its control strategy on the theory presented in section 2.5, and consists of a voltage comparator and two current comparators. The voltage comparator in the model serves as a control element that outputs a high or low signal depending on how the actual output voltage compares to the set output voltage. In the simulation model the voltage comparator was connected in series with a capacitor, symbolizing an analog PI controller seen in Figure 3.3.

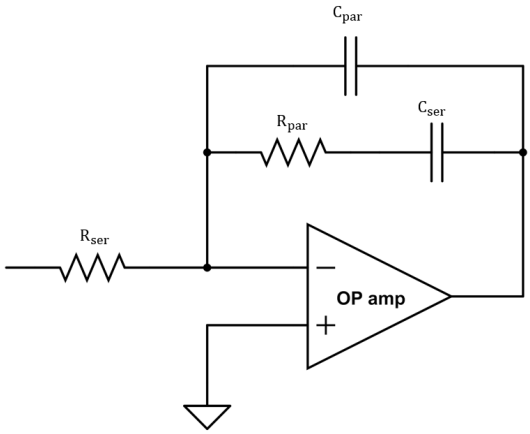

Figure 3.3: Analog PI controller.

The analog PI controller sets the proportional- and integral gain of the feedback. The combination of R_{ser} and C_{ser} initially shapes the error signal, allowing the controller to react proportionally to changes in the output voltage. R_{par} and C_{par} creates an RC network that determines the rate at which the integral part becomes effective. This network integrates the error signal, providing a summing action that helps reducing steady-state errors and improve system stability.

The two current comparators are vital components in the feedback loop, controlling the converter's switching frequency and duty cycle. They compare the rectified voltage that is modified at the behavioral voltage source, B5, in the block called 'Modified rectified signal', to the voltage comparator, seen in 3.2. The phase shift is set in radians at this modification stage, influencing the switching behavior through the feedback loop of the current comparators. This results in a phase shift of the current in regards to the voltage. The two current comparators are also connected in series with a capacitor, symbolizing the analog PI controller. It should be noted that the simulation model follows a similar ACMC control structure as the UCC28070, but without the additional complex structure. The primary focus of the model is to validate the theoretical framework and its practical feasibility.

3.2 Information applicable to both case setups

For both the analog and digital cases, the primary task was to modify the VINAC pin (pin 5) on the daugtherboard, as shown in Figure 2.20, in order to achieve a phase shift in the current. This approach was deemed most reasonable after studying the functional block diagram of the PFC, see Figure A.10. The reason was that this pin directly leads into the multiplier of the circuit, impacting the feedback loop regulating the phase of the current in accordance to section 2.6.

One thing that was changed in the motherboard, presented in Figure 3.4, was the fuse marked as F1. It was initially rated as 4 A fast fuse, which was changed to 5 A slow. This was done due to the initial fast transient, which did not work with the

fast fuse. The 5 A value was in stock and was selected for convenience.

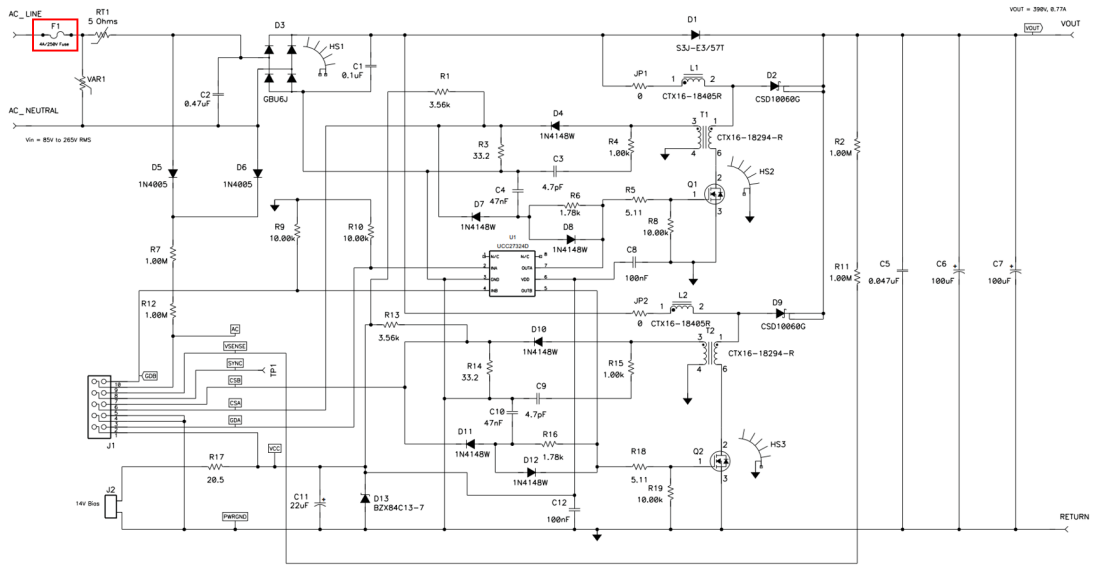

Figure 3.4: Motherboard of UCC28070EVM [28]. Reprinted with permission.

Additionally, all the tests were set up with a floating potential throughout the circuit. This was done to enhance the safety aspect and signal integrity. By floating the system there is no direct path to the ground potential, minimizing the potential difference between the high- and low-voltage side, which reduces the risk of a high current flow. In practice, an isolation transformer was utilized to ensure a floating potential. Furthermore, thoughts were given to remove possible ground loops (multiple paths to ground with different potentials), increasing safety, signal integrity and accuracy. This also allowed for choosing a reference point suiting the measurement needs and enabling isolation between different parts of the system.

3.3 Analog Case

Two analog methods were explored in attempting to achieve a phase shift of the current in relation to the input voltage. For both models, the regular input into the VINAC pin was removed and replaced with a fabricated signal. The first analog method involved the use of a signal generator together with a diode bridge to achieve full wave rectification. The second method focused on building an RC phase shift oscillator with operational amplifiers and RC phase legs to obtain the desired phase shift.

3.3.1 Signal generator and diode bridge

When using the signal generator it was set to produce a 50 Hz sinusoidal waveform, aligning with the frequency of the AC power supply and thus the electrical grid. The waveform had an amplitude of 5 V, which was a safe choice given the 7 V limit on the VINAC pin. This ensured adequate signal strength without risking component

strain. The phase of the generator was then synced to the phase of the AC power supply, ensuring that there was no initial phase shift between them. Subsequently, the signal passed through the diode bridge, becoming fully rectified and was then directed into the VINAC pin. A gradual phase shift was then applied with the signal generator until the current deviation at the zero crossing became excessive. In Figure 3.5 a block diagram of the test is presented.

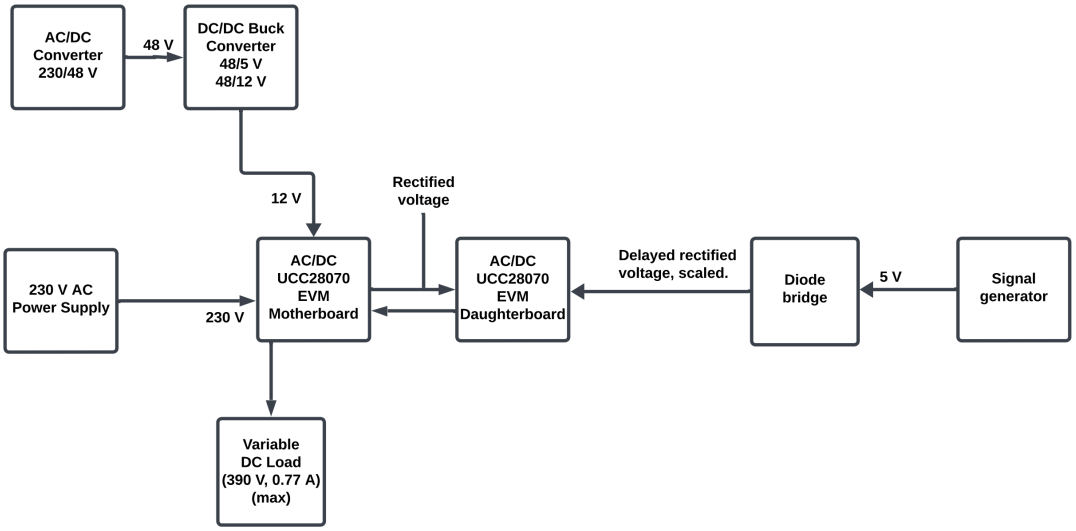

Figure 3.5: Block diagram of the analog test setup.

In regards to Figure 3.5, two converters were used to achieve the desired voltage for the respective components. An AC/DC converter was used bringing the voltage down from 230 V to 48 V. Subsequently, a DC/DC buck converter module was used to lower the 48 V to 12 V.

The diode bridge was constructed following the schematic in Figure 3.6, utilizing UF4004-E3/54 diodes. The diodes were selected to achieve a low forward voltage drop and thereby minimize losses.

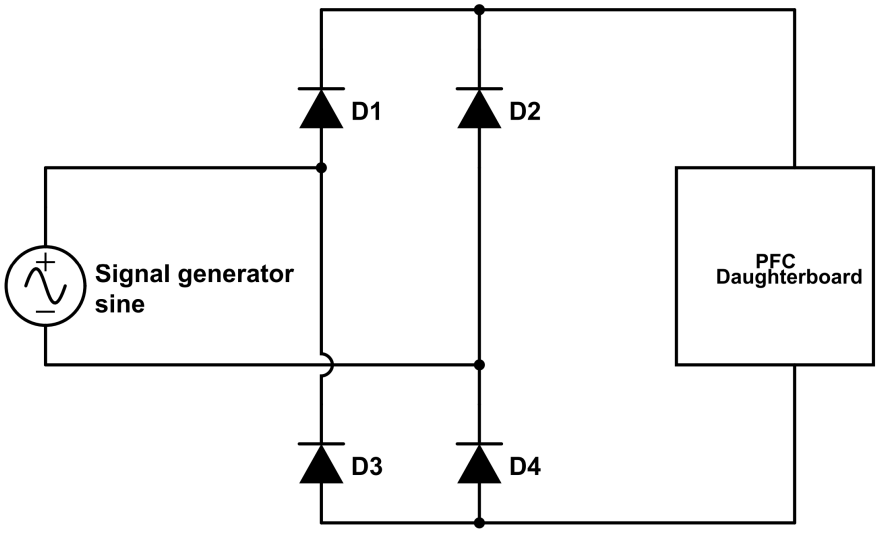

Figure 3.6: Diode bridge rectifier combined with a signal generator, load and the PFC daughterboard.

3.3.2 RC phase shift oscillator

Another method that was used to phase shift the current to a fixed value was the RC phase shift oscillator. This type of oscillator creates a phase-shifted output signal through the use of RC legs and a feedback loop [54]. The working principle implies that the capacitors are charged and discharged in a certain rate when current is fed into the circuit. This depends on the frequency of the input signal and the values of the resistors and capacitors, resulting in a phase shift between the input- and output signal. In Figure 3.7 one operational amplifier, op-amp, is used together with one RC leg to achieve an inductive behavior on the output signal.

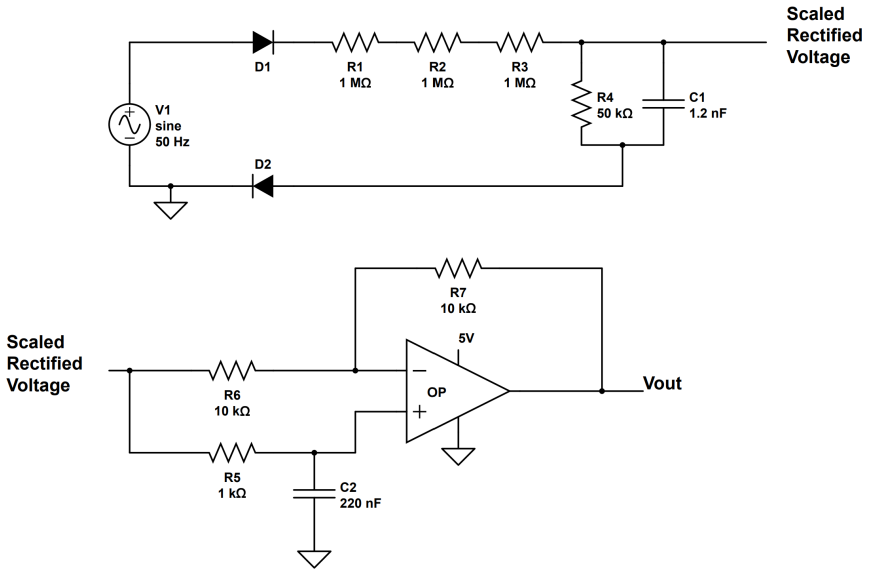

Figure 3.7: RC phase shift oscillator with one op-amp.

The oscillator was constructed in accordance to [54], where gain was determined by

$$\frac{V_{out}}{V_{in}} = \frac{\frac{s-1}{R_5C_2}}{\frac{s+1}{R_5C_2}} \tag{3.1}$$

The phase shift at any frequency was determined as

$$\text{phase(rad)} = \tan^{-1}\left(\frac{\frac{2\omega}{R_5C_2}}{\omega^2 - (\frac{1}{R_5C_2})^2}\right) \tag{3.2}$$

To achieve a capacitive behavior on the output signal three operational amplifiers were used instead, as seen in Figure 3.8. The first op-amp is used to generate the phase shift together with the three RC legs according to (3.2). Because a capacitive behavior of the circuit is desired, the combined phase shift needs to be slightly less than half a period, 180°. This was facilitated most effectively by utilizing three RC phase legs, due to that each RC leg could achieve a maximum of 90° phase shift [55]. The output frequency of the oscillator, presented in [56], was calculated by

$$f_{out} = \frac{\sqrt{2N}}{2\pi RC} \tag{3.3}$$

where N is the amount of RC phase legs.

One problem that found was regarding the amplitude of the signal that was put in to the VINAC pin. The PFC circuit only identified zero crossings below 0.7 V. However, due to employing one op-amp, with three RC phase legs, with such a significant phase shift, a DC offset exceeding 0.7 V was introduced. This meant that the converter did not recognize the signal, as no zero crossings were detected. This was tried to be solved by adding two additional op-amps, with the second one inverting the signal and the third one fine-tuning the DC offset. The inverting gain of the second op-amp, given in [57], was calculated by

$$A = \frac{V_{out}}{V_{in}} = -\frac{R_9}{R_8} \tag{3.4}$$

and the DC offset of the third op-amp, was calculated in accordance to [58] as

$$V_{offset} = (1 + \frac{R_{13}}{R_{12}})V_2 \tag{3.5}$$

But due to the complexity of adding two more op-amps, achieving functionality with these RC phase oscillators required precise evaluation of factors like bandwidth and component accuracy. This consequently led to the decision to discard this approach. The intended solution is presented in Figure 3.8.

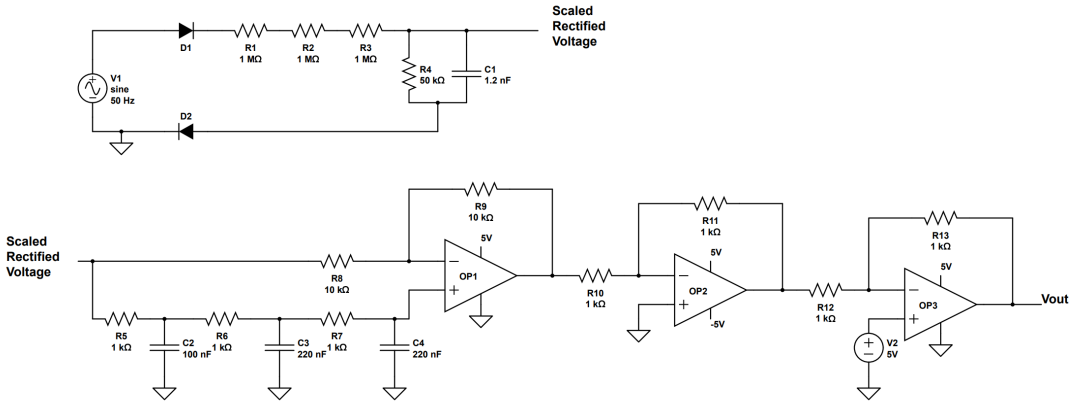

Figure 3.8: RC phase shift oscillator with three op-amps.

3.4 Digital Case

Following the analog phase shift which confirmed the feasibility of the solution, the next step involved implementing the phase shift digitally. A microcontroller was used, tasked with delaying the voltage signal entering the VINAC pin. This was done to achieve the intended delay in current, attaining the user-defined power factor. To accomplish this, the microcontroller required voltage and current measurements as inputs to perform the necessary calculations. Hence, voltage and current sensors were essential components. In Figure 3.9 a block diagram over the complete case setup is presented.

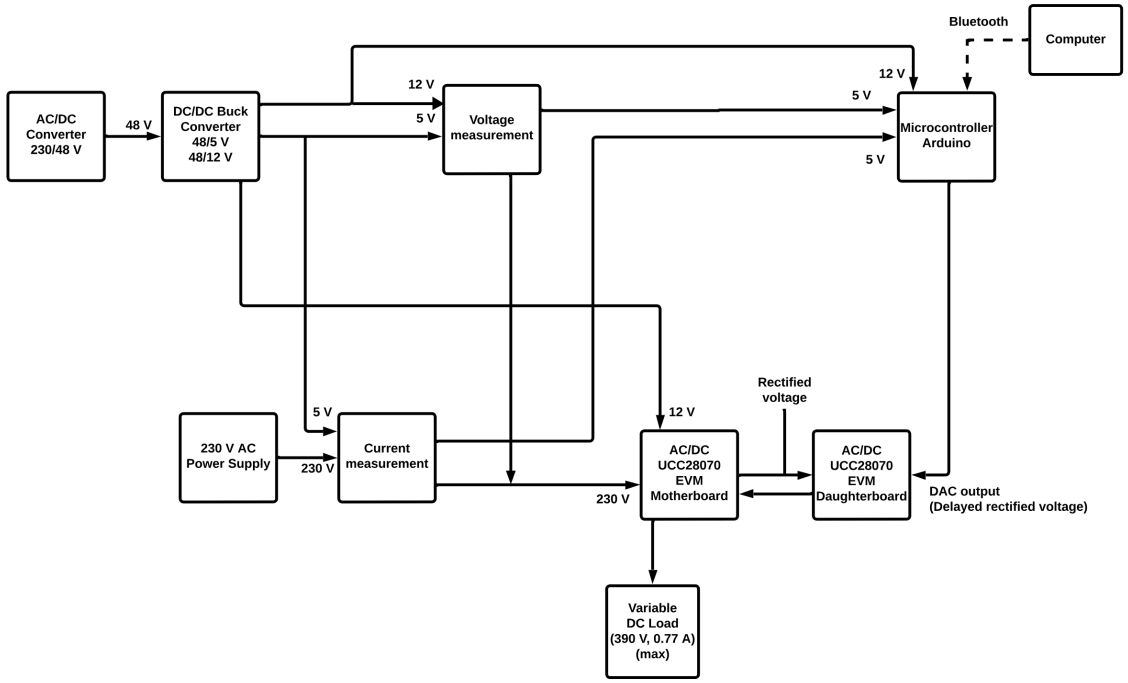

Figure 3.9: Block diagram over the digital setup.

Two converters were used to achieve the desired voltage for the respective components. An AC/DC converter was used bringing the voltage down from 230 V to 48 V. Subsequently, a DC/DC buck converter module was used to lower the 48 V to 5 V and 12 V, respectively.

To facilitate the routing of the VINAC signal through the microcontroller and establish a closed circuit, it was necessary to remove two components: R1 and R5. This modification allowed for the signal's reconnection back to the VINAC pin on the daughterboard, as illustrated in Figure 3.10.

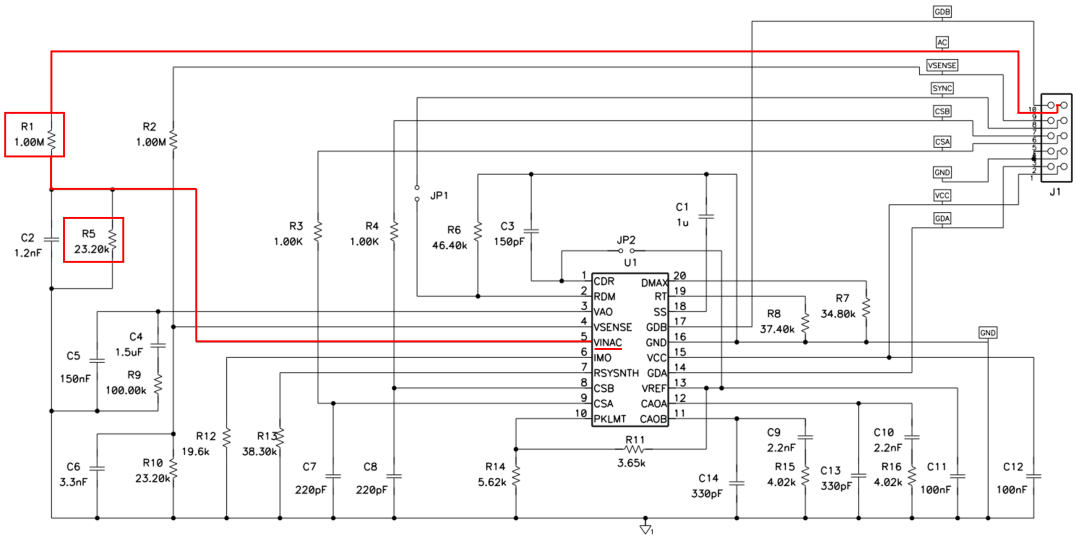

Figure 3.10: Daughterboard of UCC28070EVM [28]. Reprinted with permission.

The removed components from the daughterboard were placed on a separate breadboard connected to the microcontroller. In Figure 3.11 the schematic over the separate breadboard is presented.

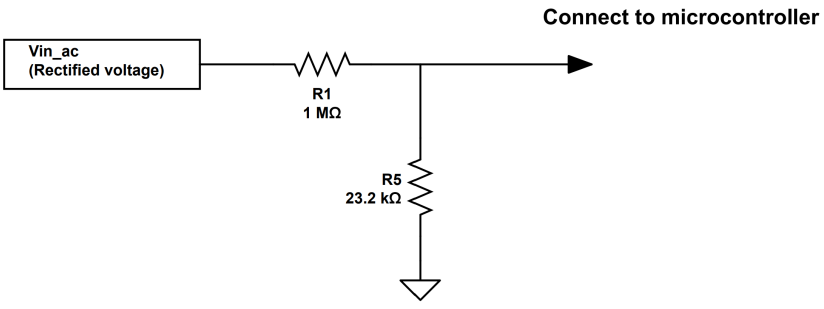

Figure 3.11: Separate breadboard with the removed components from the daughterboard.

3.4.1 Built voltage- and current sensors

To be able to measure the voltage, a voltage sensing circuit seen in Figure 3.12 was built. The key component in the circuit is the LTC6226, a low distortion rail-to-rail output operational amplifier. This allowed for the output voltage to swing much closer to both the positive and negative supply rails, compared to an traditional operational amplifier. Consequently, the rail-to-rail feature offered improved performance and flexibility in applications where precise control of the entire voltage range is necessary. In this application, the LTC6226, was used in a differential amplifier circuit, which converts the sinusoidal input voltage to a measurable voltage for the microcontroller. The resistors, R_1-R_{10}, and the capacitors, C_1-C_3, are used for the determining the gain and filtering characteristics of the circuit. These components directly affected the range of measurable voltages which were obtained by the microcontroller.

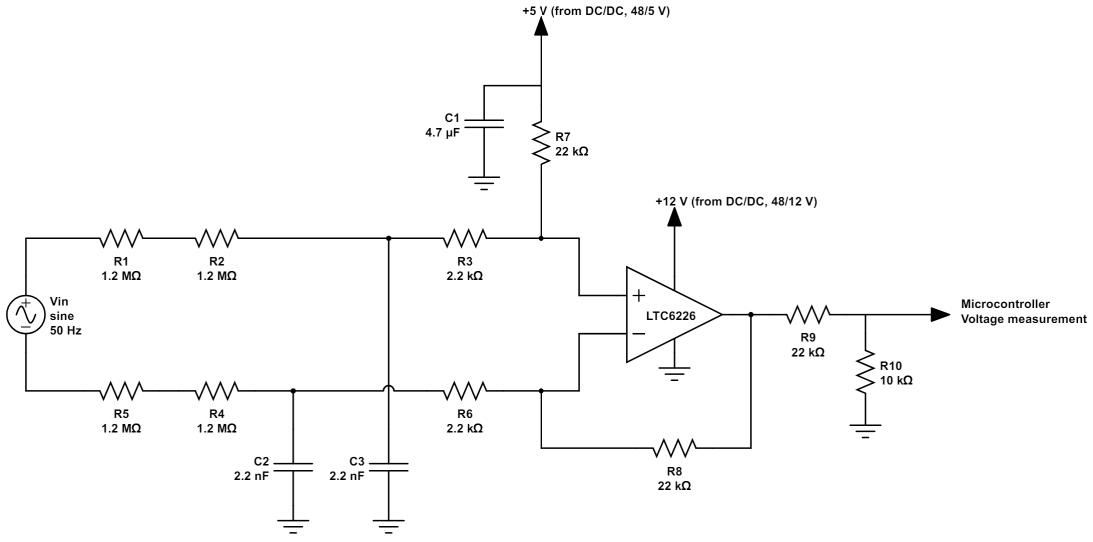

Figure 3.12: Voltage sensor for the microcontroller.

The gain in the voltage sensor is calculated by

$$\frac{V_{out}}{V_{in}} = \frac{R_8}{R_1 + R_2 + R_3} \tag{3.6}$$

The purpose of R_7 is to raise the DC voltage level to avoid negative values. The maximum output of the op-amp becomes

$$\frac{V_{out}}{V_{in}}\sqrt{2}V_{in} = \sqrt{2}V_{out} \tag{3.7}$$

Lastly, the resistors R_9 and R_{10} form a voltage divider, scaling the voltage to suitable levels for the microcontroller.

The built current sensing circuit, presented in Figure 3.13, utilized the ACS70331 current sensor. The ACS70331 uses Giant Magneto-Resistive, GMR, technology for

measuring the current flowing through the conductor [59]. This is done by generating a magnetic field, which is then detected by the sensor. Subsequently, the sensor's output is translated into a proportional analog voltage, which is obtained by the microcontroller. The capacitors are used for filtering improving the accuracy of the measurement.

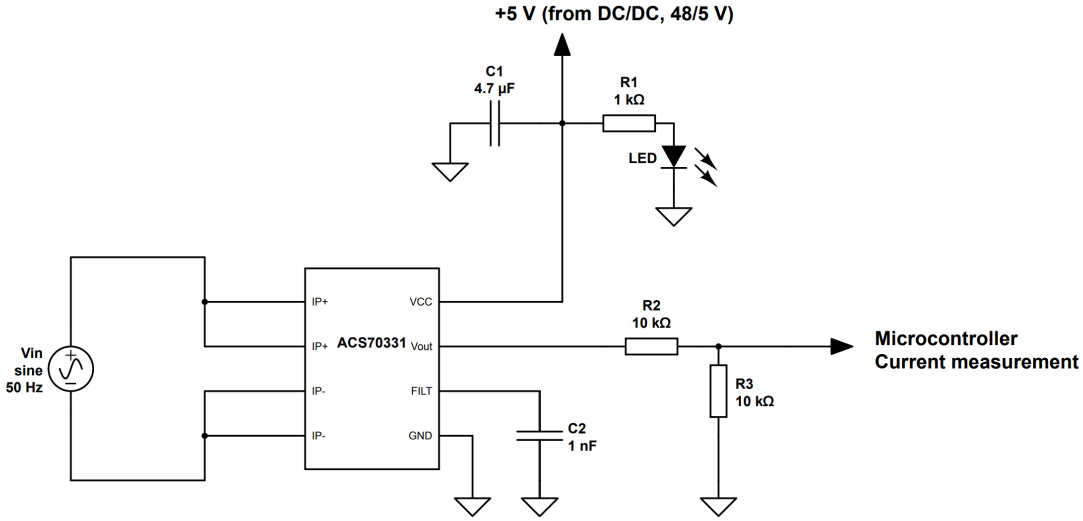

Figure 3.13: Current sensor for the microcontroller.

The signal integrity of the custom-built current and voltage sensors ended up being poor when the PFC was on, resulting in excessive noise and inaccurate measurements at the microcontroller, see Figure 3.14 and 3.15. Therefore, it was decided to use a commercially manufactured voltage- and current sensor designed specifically for this purpose.

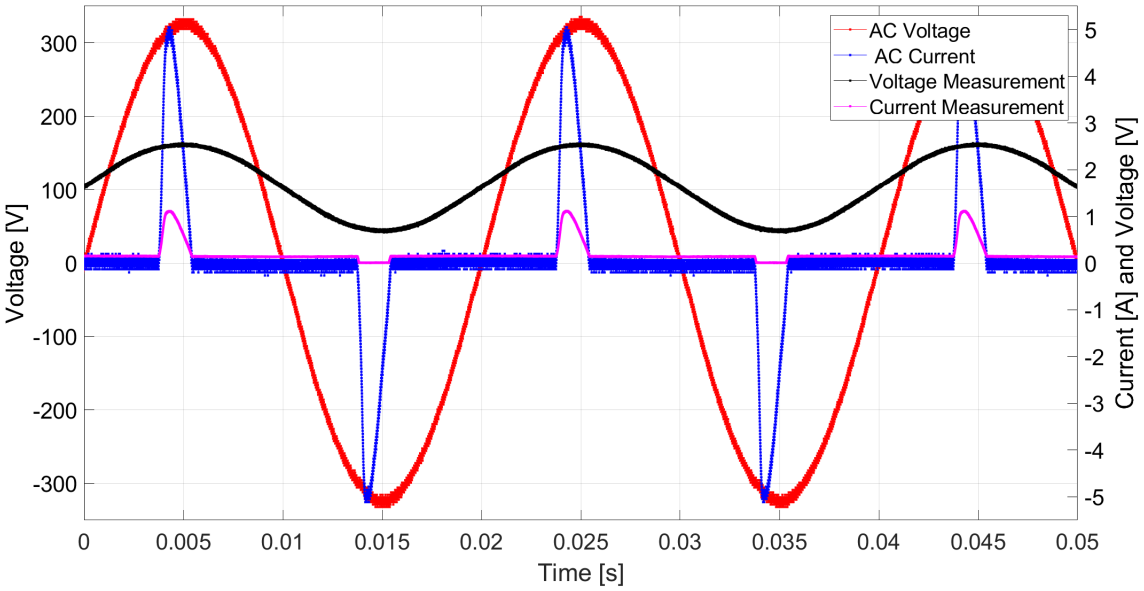

Figure 3.14: Voltage and current measurements using the built sensors, PFC switched off.

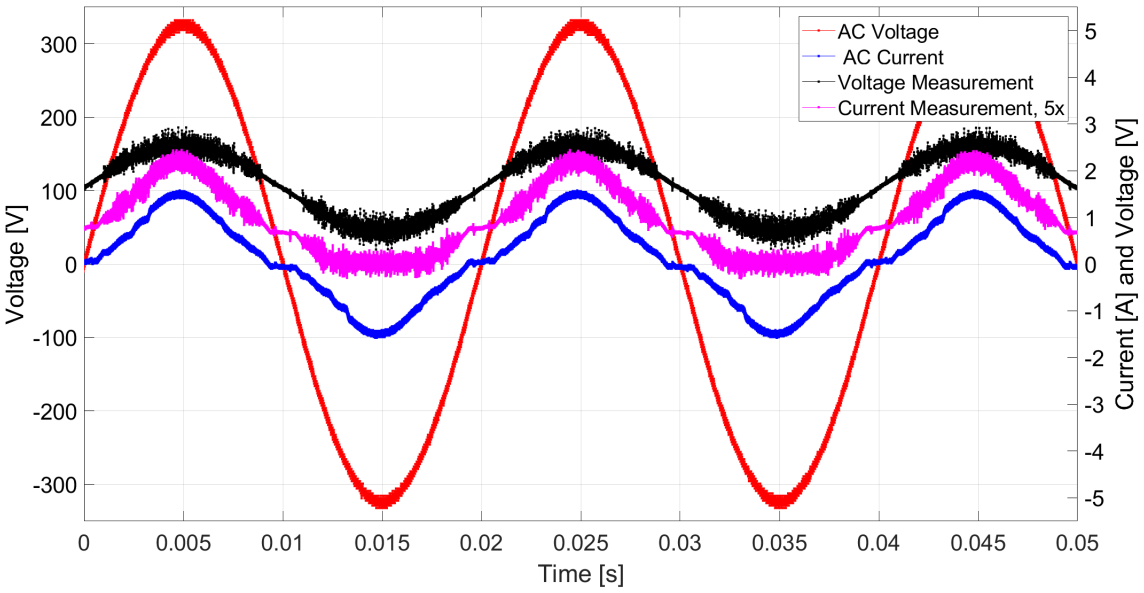

Figure 3.15: Voltage and current measurements using the built sensors, current measurement is amplified 5 times. PFC is switched on.

3.4.2 Voltage- and current sensor modules

The voltage module used was the ZMPT101B, shown in Figure 3.16. It utilizes a one-to-one voltage transformer and a voltage divider to measure AC voltage. The transformer isolates the input interface from the output interface in the module, while the voltage divider makes the data suitable for further processing by the microcontroller. The module also has a potentiometer which is used for calibrating and adjusting the the output voltage.

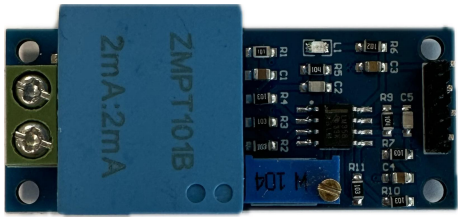

Figure 3.16: ZMPT101B Voltage sensor module.

The current sensor that was used for measuring the alternating current was the ACS712, shown in Figure 3.17. The module measures the current by utilizing the hall effect which occurs when current is flowing through an conductor while placed in an electric field. This results in a voltage that is proportional to the current. This voltage is then used together with the sensitivity of the sensor to determine the current. The sensitivity is a property of the sensor that describes how much the Hall voltage changes per unit through the electrical current that is flowing. These Hall effect current sensors are useful due to that they are non intrusive, meaning that they do not need to break the circuit to measure the current. It is therefore usually isolated from the circuit where the current is measured, making it relatively

safe to use. The current sensor that is used, the ACS712, is rated for 20 A and has a sensitivity of 100 mV/A.

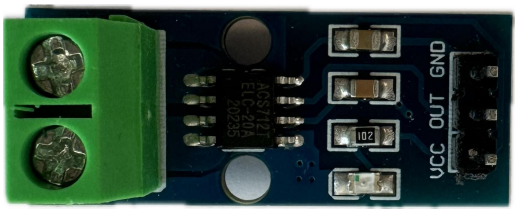

Figure 3.17: ACS712 Current sensor module.

3.4.3 Microcontroller

To attain the user-defined power factor, two microcontrollers were tested and used, the LOLIND32 and the Arduino UNO R4. During the initial testing phase, an issue was found with the LOLIND32. The AC voltage and current measurements necessitated the use of an external library in the Arudino IDE software to produce accurate voltage- and current inputs, which obstructed further code processing. Furthermore, the 8-bit DAC that was available in the LOLIND32, did not provide a sufficient enough signal to generate the rectified sinusoidal waveform. Therefore the Arduino UNO R4 seemed like a better alternative, providing better voltage- and current readings without the need of external libraries. It also offered a 12-bit DAC resolution, which resulted in a more accurate output for the rectified sinusoidal voltage.

The operating principle for both microcontrollers involves obtaining the given current and voltage values from the modules. Through analyzing the phase shift between current and voltage, the controller adjusts the phase shift by delaying the current for a certain time frame, to obtain the user-defined power factor. The code used in the Arduino Uno R4, written in the Arduino IDE, is presented in Appendix C.1. The code is inspired by [60], although modifications have been done to achieve an adjustable power factor. This includes an PI controller for a closed loop system, zero crossing detection for obtaining the frequency, and a filter for smoothing the DAC output. The code displays real- and apparent power, current- and voltage RMS values, and the power factor.

3.5 Testing

The following tests were performed to determine the functionality of the converter. For all the tests the analog method was used with the signal generator and the diode bridge rectifier. This method gave the best signal integrity with the least amount of noise. The connection was done in accordance to section 3.3.1 and is shown in Figure 3.18.

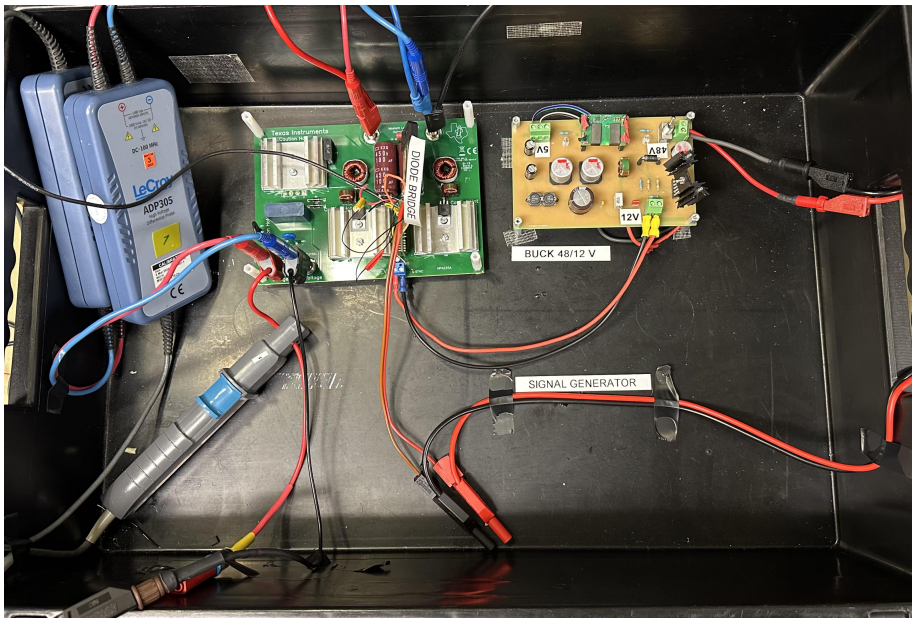

Figure 3.18: Test setup for the analog case.

The necessary external equipment used for making the testing possible is presented in Table 3.2.

Table 3.2: External equipment used for test setups.

Device	Model
AC power supply	Chroma model 6430
Electronic load	EA-EL 9750-20 B
Signal generator	Keysight 33600A
DC power supply	Delta Elektronika SM7020-D

3.5.1 Power factor

A test was made to determine the power factor for three different values of phase shift: 0°, 30°, and 60°, with varying loads on the DC side of the converter. This was done for each load level, ranging from 10 % to 100 % with 10 % increments.

To calculate the power factor the THD value was used in accordance to (2.8). Therefore, an FFT analysis was done on the current through the converter for each load level and phase shift. This enabled a frequency analysis of the current signal, making it possible to observe the amplitude for the different harmonic components.

3.5.2 Efficiency

The efficiency test was done for the same load levels of 10% to 100% with 10% increments and for the same phase shift, 0°, 30°, and 60°. The efficiency was calculated through the ratio between the input and output power as $P_{out}/P_{in} \cdot 100$. This was

done by monitoring the input voltage and current, as well as the output current and voltage.

3.5.3 Harmonics

To further evaluate the converter's performance, a Fast Fourier Transform (FFT) test was conducted across various load levels and phase shifts to assess compliance with regulatory EMI and EMC standards. This testing was carried out using an oscilloscope. It should be noted that a LISN could not be used during these tests due to the presence of extensive equipment near the test object, which compromised the reliability of the results. During the test, the load on the DC side of the converter was maintained at 0.5 A. Measurements were taken for the input current, while the phase input to the controller was varied across 15 distinct settings, ranging from -60° to +60°. The waveforms recorded included input current, input voltage, output voltage, and the signal to the VinAC pin.

3.5.4 Temperature

The converter's operation was monitored through an infrared, IR, thermometer at max power, 300 W, for the three different phase shifts. The converter was left to operate for one hour at each setting. The objective of this test was to investigate whether the components experienced an increase in temperature when exposed to phase shifting of the current. It was also monitored that the components stayed withing their respective operating temperature. According to the datasheet of the varistor [61], it has a temperature range from -40 °C to 105 °C, while the inductors have operating temperature range of -20 °C to 105 °C [62].

3.5.5 Microgrid

To observe the converter's ability to perform a local phase shift in a real-world scenario, a microgrid was connected on the AC side. The microgrid consisted of multiple fluorescent lights, which resulted in a peak current value of 2.25 A with an inductive behavior. Therefore, only an inductive setting was tested due to the available equipment. The voltage, current and frequency were monitored and subsequently, harmonic distortion as well as power factor were calculated.

The test was designed around three different current settings on the DC side of the converter: 0.05 A, 0.145 A and 0.5 A. Each scenario was tested across five different phase shifts: -60°, -30°, 0°, 30°, and 60°.

In Figure 3.19 a schematic over the microgrid test setup is presented, where the non-ideal loads are represented by old fluorescent lights with an inductive behavior.

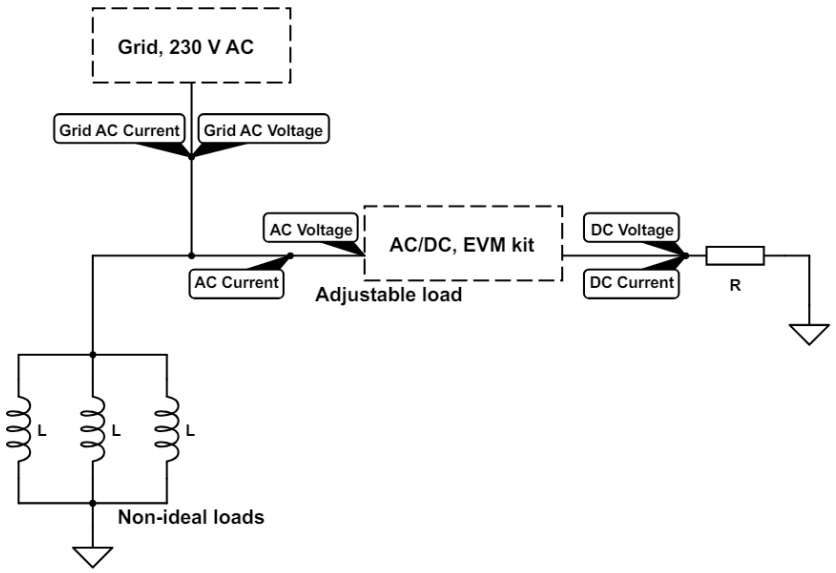

Figure 3.19: Schematic over the microgrid setup with measured voltages and currents presented.

A baseline case of the grid was established, with no converter connected to the grid and only the lights operational. This allowed for the determination of the power factor of the microgrid.

3.5.6 Maximum phase shift for different loads

This test evaluated the attainable phase shift, based on the load applied on the DC side. It was done for full load, 300 W (0.77 A), and for half the power, 150 W (0.385 A). Based on this, the converter's phase-shifting capability is examined for different loads.

3.5.7 Line regulation

For this test, different input voltages were applied at half load of 150 W and full load of 300 W. The input voltages were 85 V, 175 V and 265 V, due to the operating voltage range of the converter, 85-265 V. Each voltage level was tested for three different phase shifts, 0°, 30°, and 60°. This test denoted the converter's capability to sustain a steady output voltage.

3.5.8 Input voltage distortion

The distortion of the input voltage for the AC/DC converter was measured for the three different phases with the FFT function of the oscilloscope. This analysis identified problematic harmonics that could affect the performance and longevity of the converter and the connected equipment.

3.5.9 Load regulation

During this test, the output voltage was measured under different loads and phase shifts to ensure that the converter regulated the output voltage to the set level, 390 V. The phase shifts were set to 0°, 30°, and 60°, where the loads on the DC side ranged from 10 % to 100 % with 10 % increments. An electronic load was utilized to achieve the different loads. This test exhibited the converter's ability to maintain a constant output voltage, despite changes in output current or load.

3.5.10 Output voltage and output current ripple

In this test, the ripple of the output voltage and output current was tested. The ripple assessed the performance and quality of the converter, where lower ripple values indicated better stability and reliability for connected electronic devices. The ripple was studied for phase shifts of 0°, 30°, and 60°, and the loads ranged from 10 % to 100 % with 10 % increments.

3.5.11 1:1 proportionality

This test was done to study the current phase shift in regards to the voltage signal into the VINAC pin. It was done for the whole input voltage interval, 85-265 V, to asses when the 1:1 proportionality starts decreasing. This was done for half load, 150 W, and for full load, 300 W. The test indicated how predictable the end phase shift of the current was in relation to the input voltage and load.

3.6 Digital Results

For the digital case, the voltage and current modules were tested to assess their performance. Additionally, the DAC output was studied. The connection was made in accordance with section 3.4 and is shown in Figure 3.20.

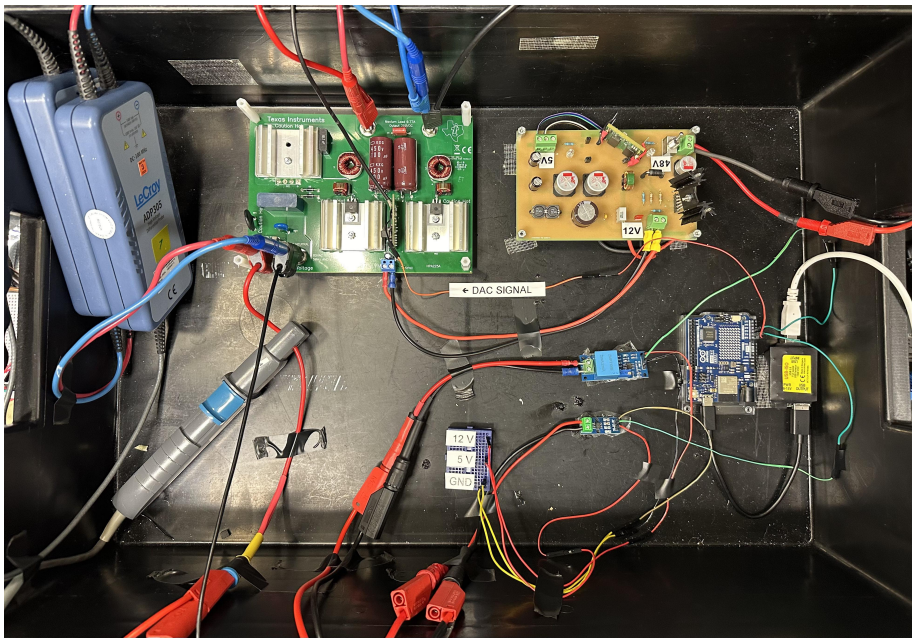

Figure 3.20: Test setup for digital case.

4
Results

In the following chapter, outcomes from the simulations, the AC/DC converter prototype, and the demand and application of a specific grid service will be presented.

4.1 Simulated results

The result from a 0° phase-shifted current, is shown in Figure 4.1. When output power was set to 150 W the RMS value of the current reached a value 0.65 A.

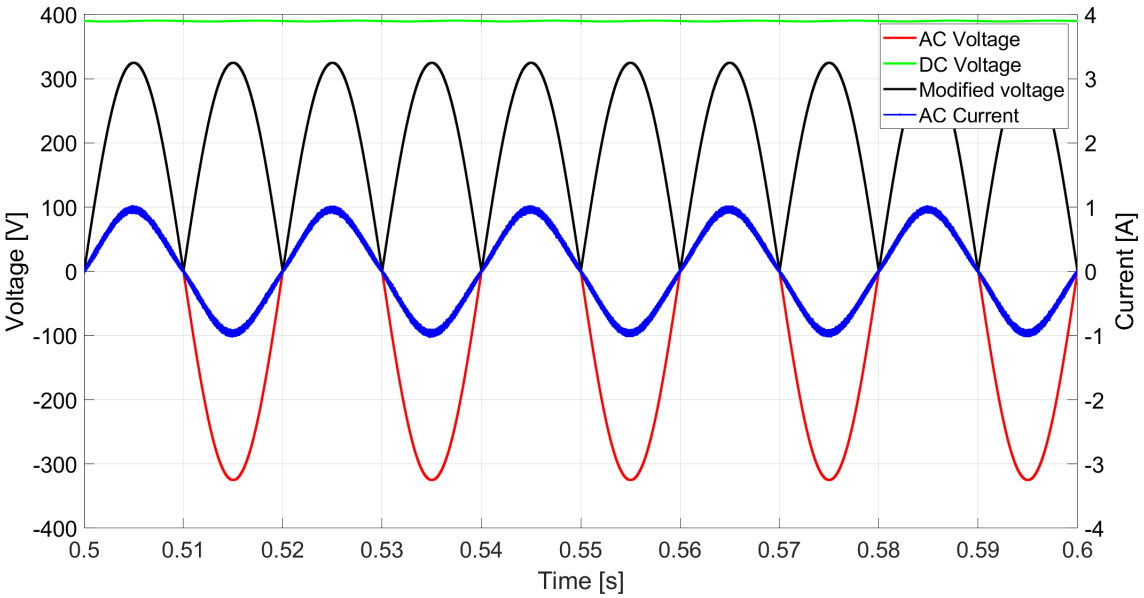

Figure 4.1: Simulated input voltage and current, modified voltage and output current, 0° phase shift for an output power of 150 W.

Figure 4.2 represents the 20 first harmonic components of the input current at a load of 150 W. The THD of the input current at 0° is 4.52 %.

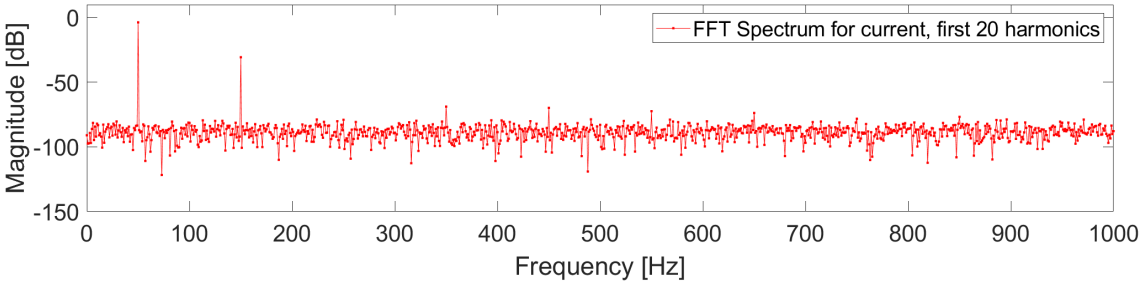

Figure 4.2: FFT analysis of the 20 first harmonic components for the input current, 0° phase shift for an output power of 150 W.

In Figure 4.3 the rectified signal had been phase shifted 30° and the output power was set to 150 W. The RMS value of the current reached a value 0.70 A and the current spikes at zero crossings reached approximately ±0.45 A.

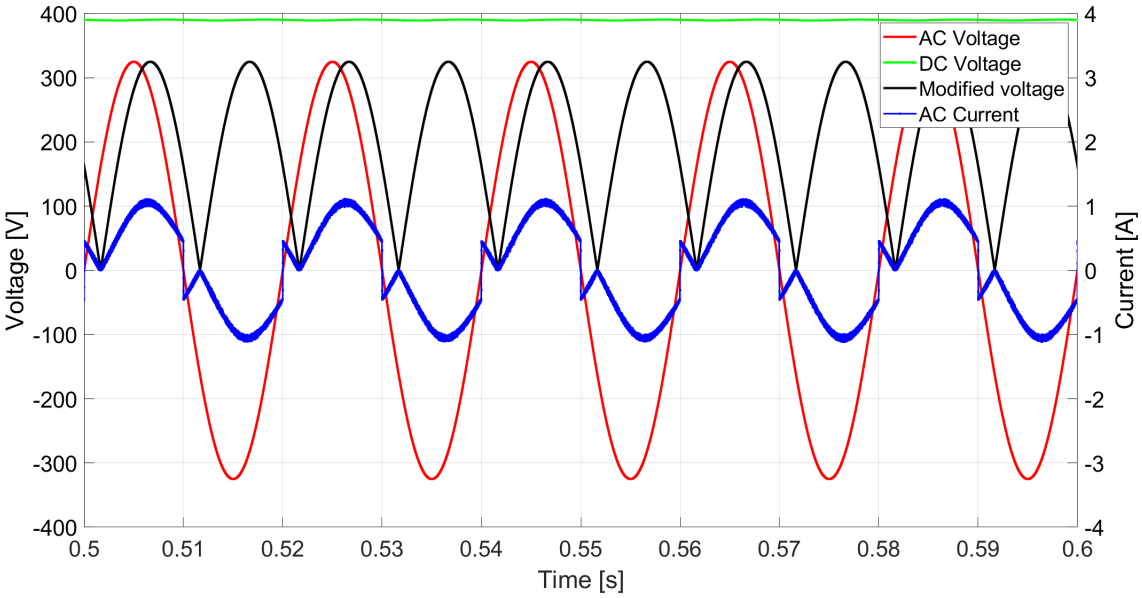

Figure 4.3: Simulated input voltage and current, modified voltage and output current, 30° phase shift for an output power of 150 W.

Figure 4.4 represents the 20 first harmonic components of the input current at a load of 150 W. The THD of the input current at 30° is 28.13 %.

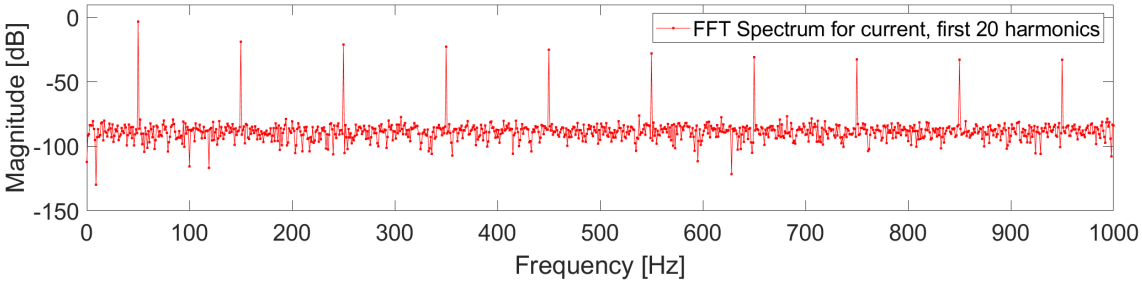

Figure 4.4: FFT analysis of the 20 first harmonic components for the input current, 30° phase shift for an output power of 150 W.

In Figure 4.5 the rectified signal had been phase shifted 60° and the output power was set to 150 W. The RMS value of the current reached a value 0.87 A and the current spikes at zero crossings reached approximately ±1.045 A.

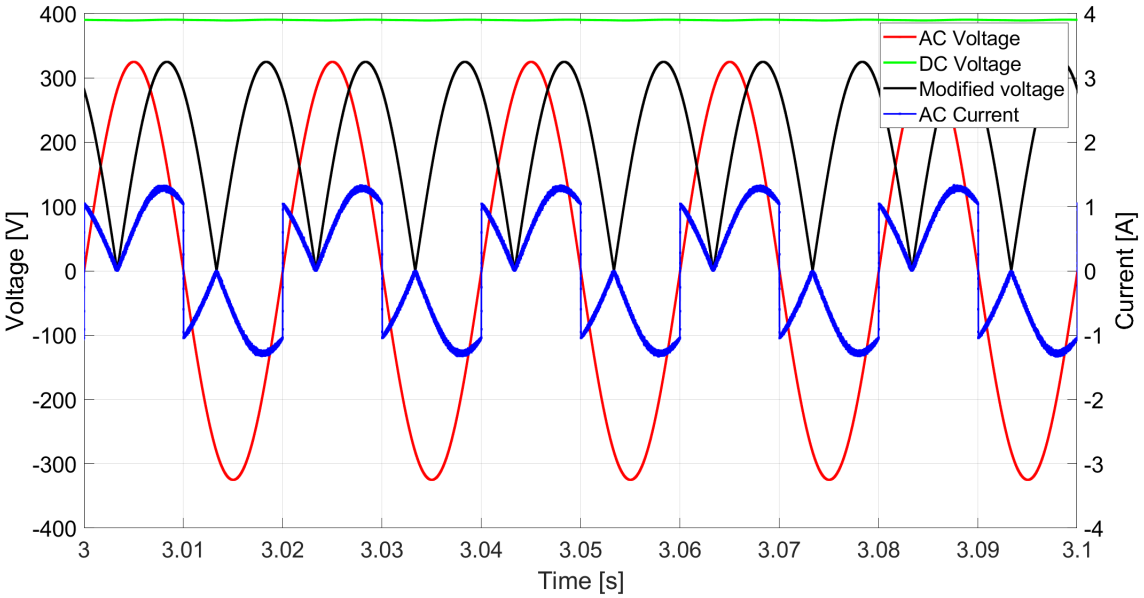

Figure 4.5: Simulated input voltage and current, modified voltage and output current, 60° phase shift for an output power of 150 W.

Figure 4.6 represents the 20 first harmonic components of the input current at a load of 150 W. The THD of the input current at 60° is 77.5 %.

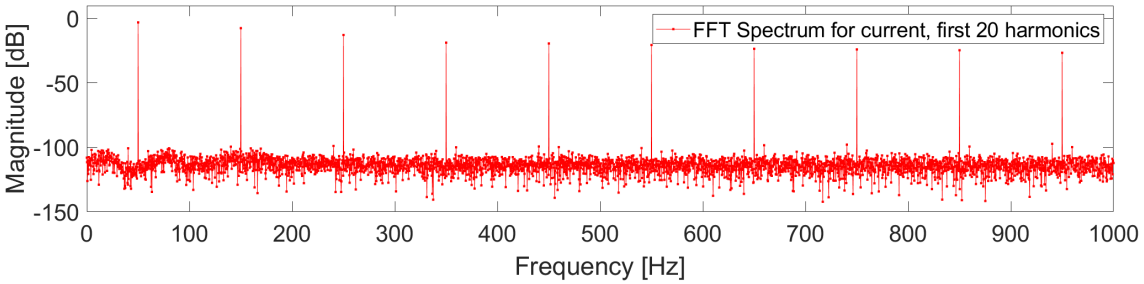

Figure 4.6: FFT analysis of the 20 first harmonic components for the input current, 60° phase shift for an output power of 150 W.

For all simulations made at 150 W, it was evident that the current closely tracked the voltage waveform. The displacement power factor, distortion power factor and the resulting power factor at 150 W is presented in Table 4.1.

Table 4.1: Power factor for various phase shift inputs at 150 W.

Phase shift [°]	$\mathbf{PF_{distortion}}$	$\mathbf{PF_{displacement}}$	$\mathbf{PF_{total}}$
0	0.99	1	0.99
30	0.96	0.87	0.83
60	0.79	0.5	0.40

In Figure 4.7, the rectified signal had been phase shifted 0° and the output power was set to 300 W. The RMS value of the current was 1.31 A.

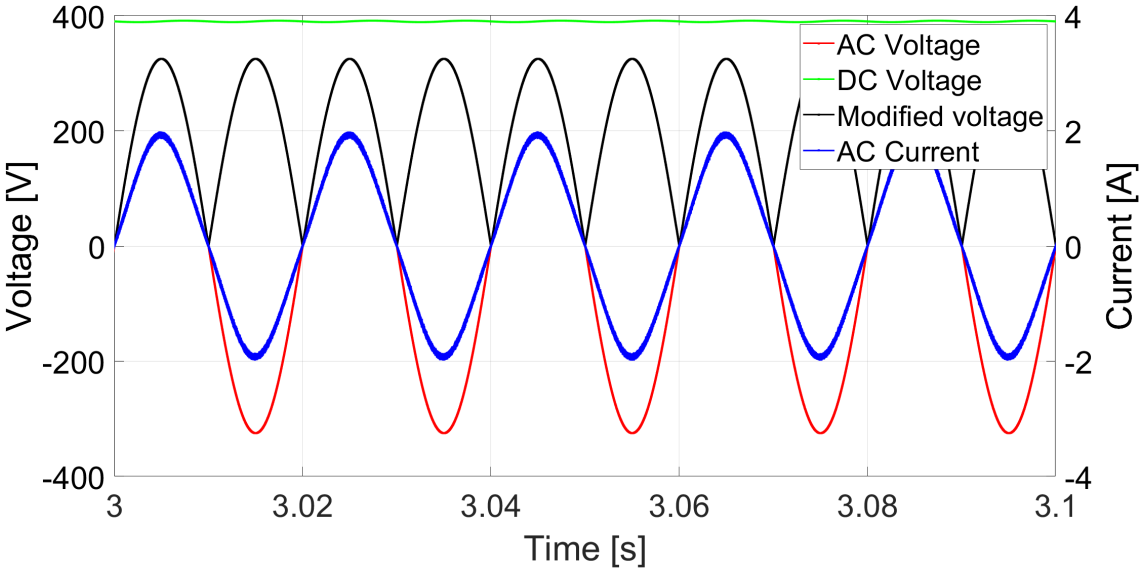

Figure 4.7: Simulated input voltage and current, modified voltage and output current, 0° phase shift for an output power of 300 W.

Figure 4.8 represents the 20 first harmonic components of the input current at a load of 300 W. The THD of the input current at 0° is 4.41 %.

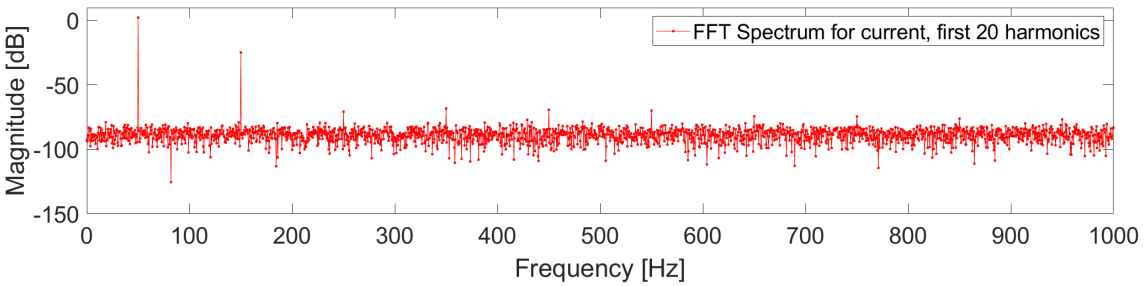

Figure 4.8: FFT analysis of the 20 first harmonic components for the input current, 0° phase shift for an output power of 300 W.

In Figure 4.9 the rectified signal had been phase shifted 30°, when the output power of the converter was set to 300 W. The RMS value of the current reached a value 1.44 A and the current spikes at the zero crossings reached approximately ±0.91 A.

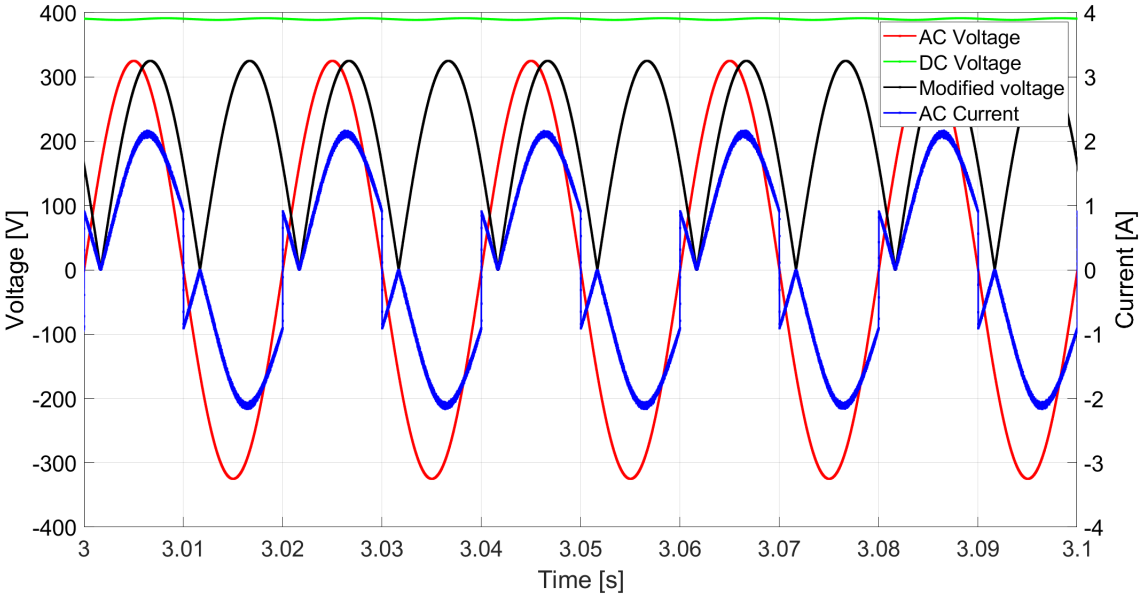

Figure 4.9: Simulated input voltage and current, modified voltage and output current, 30° phase shift for an output power of 300 W.

Figure 4.10 represents the 20 first harmonic components of the input current at a load of 300 W. The THD of the input current at 30° is 27.84 %.

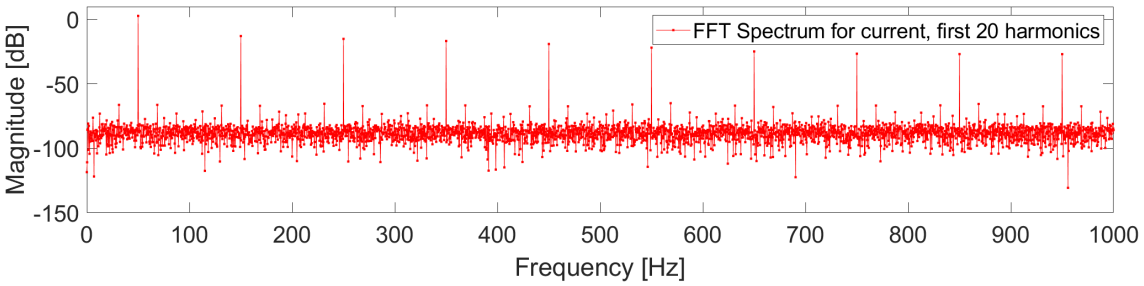

Figure 4.10: FFT analysis of the 20 first harmonic components for the input current, 30° phase shift for an output power of 300 W.

In Figure 4.11 the rectified signal had been phase shifted 60°, when the output power of the converter was set to 300 W. The RMS value of the current reached a value 1.82 A and the current spikes at the zero crossings reached approximately ±2.09 A.

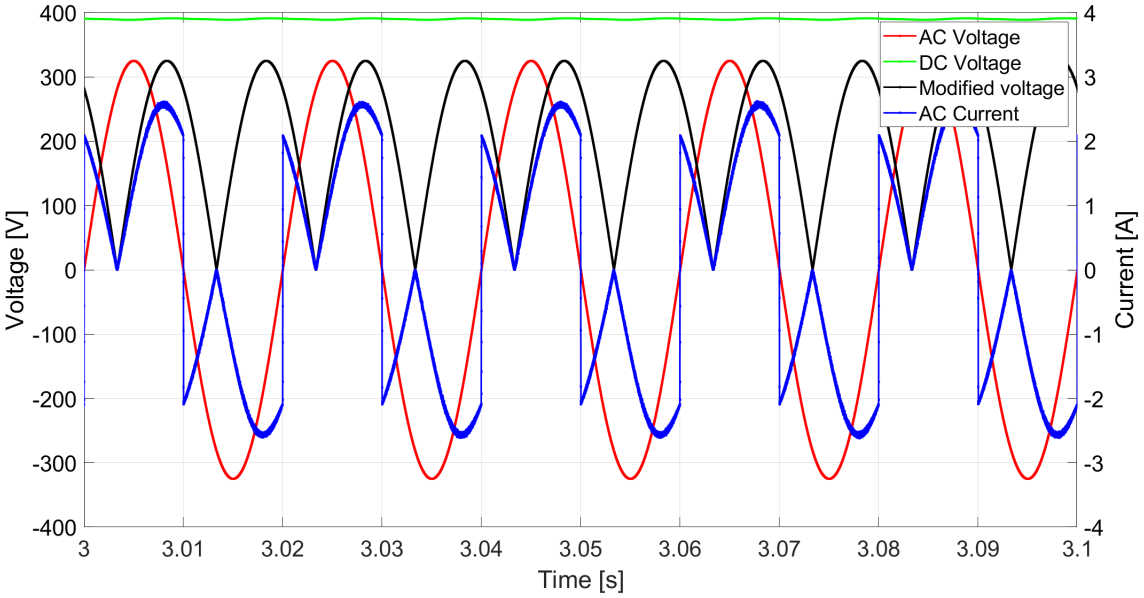

Figure 4.11: Simulated input voltage and current, modified voltage and output current, 60° phase shift for an output power of 300 W.

Figure 4.12 represents the 20 first harmonic components of the input current at a load of 300 W. The THD of the input current at 60° is 77.43 %.

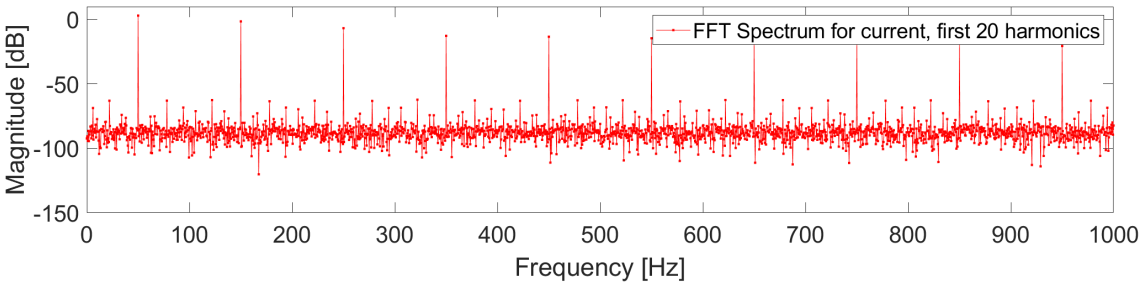

Figure 4.12: FFT analysis of the 20 first harmonic components for the input current, 60° phase shift for an output power of 300 W.

For all simulations made at 300 W, it was evident that the current closely tracked the voltage waveform. The displacement power factor, distortion power factor and the resulting power factor at 300 W is presented in Table 4.2.

Table 4.2: Power factor for various phase shift inputs at 300 W.

Phase shift [°]	$\mathbf{PF_{distortion}}$	$\mathbf{PF_{displacement}}$	$\mathbf{PF_{total}}$
0	0.99	1	0.99
30	0.96	0.87	0.84
60	0.79	0.5	0.39

Similar simulations, showcasing negative phase shifts, are presented in Appendix B.1.

4.2 Measured results from the prototype

In the following section, the results from the tests performed on the prototype are presented in the same order as in chapter 3.5.

4.2.1 Power factor

In Figure 4.13 the power factor is shown, reaching a maximum of 0.97 for a load of 300 W (0.77 A) at 0° phase shift with no modifications made to the control circuitry. The lowest power factor 0.76, was obtained at 60 ° phase shift, with a load of 80 %. Generally, it was seen that the power factor increased with an increasing load, except for the case with a phase shift of 60°.

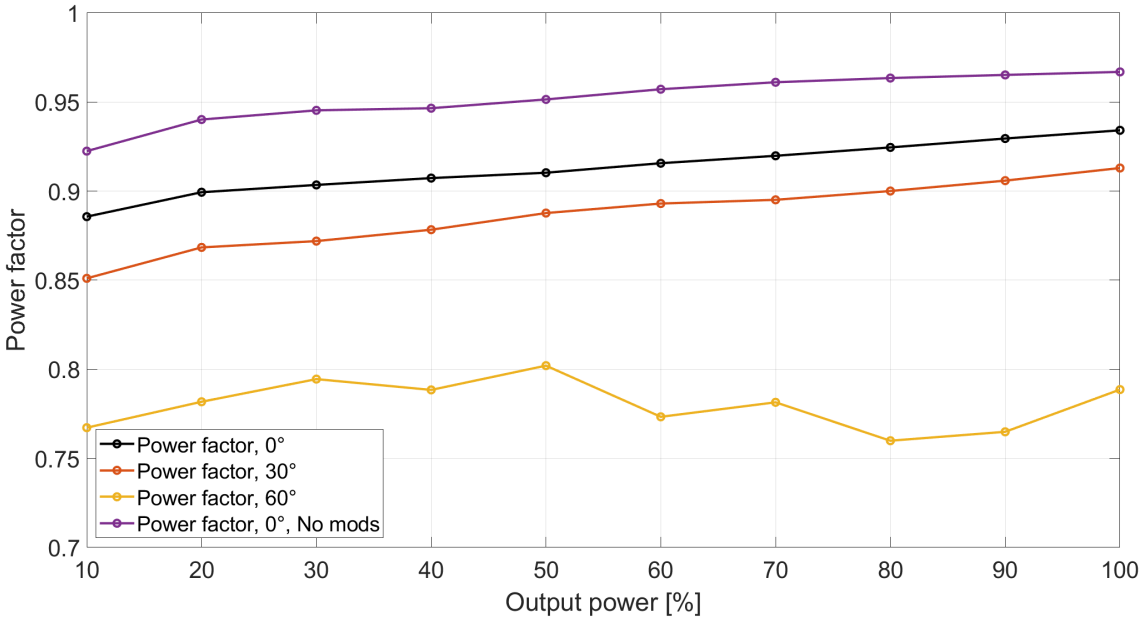

Figure 4.13: Measured power factor of the input current for different loads and phase inputs.

4.2.2 Efficiency

Figure 4.14 shows the converter's efficiency, reaching its highest point of 95 % at a load of 60 % (0.462 A) and 0° phase shift, with no modifications made to the control circuitry. The efficiency reached its minimum of 70.7 % when the load was set to 80 % and the phase shift to 60°. Generally, the efficiency increased with an increasing load, except for the case with a phase shift of 60° where it decreased.

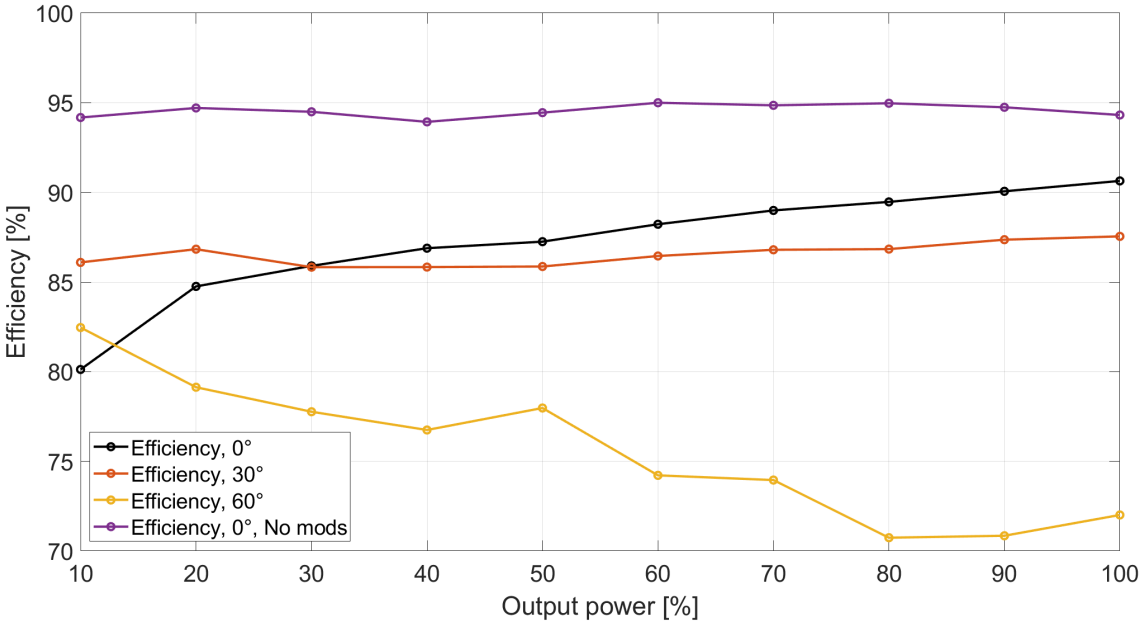

Figure 4.14: Measured efficiency of the converter at different loads and phase inputs.

4.2.3 Harmonics

The measured waveforms for a phase shift of 0°, are illustrated in Figure 4.15. The output voltage remained stable at approximately 390 V.

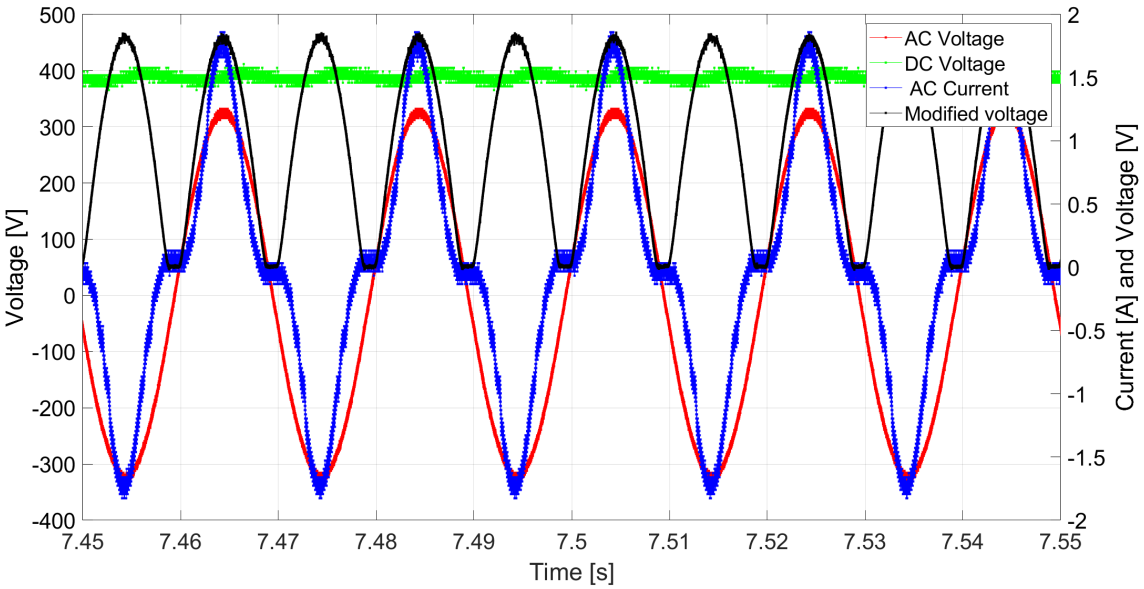

Figure 4.15: Measured voltages and current for 0° phase shift.

In Figure 4.16 the complete FFT of the signal is displayed, while Figure 4.17 represents the 20 first harmonic components of the current. The fundamental component was calculated to an RMS value of 0.882 A and the total RMS current was calculated to 0.947 A. The THD of the input current at 0° was 38.87 % and the total

power factor was 0.932.

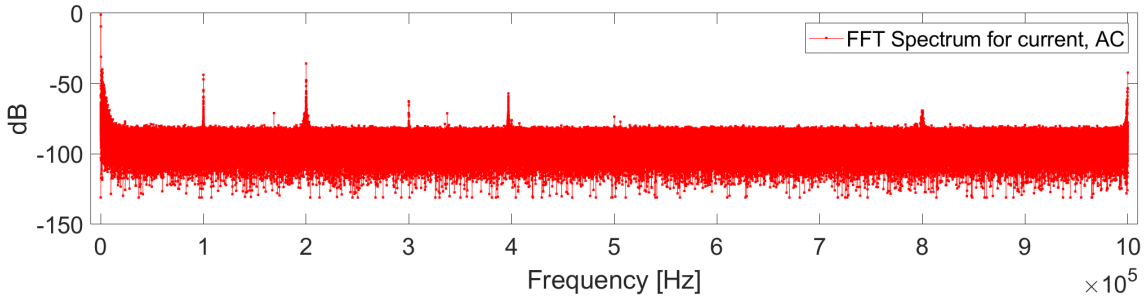

Figure 4.16: Whole FFT spectrum of the input current at 0° phase shift.

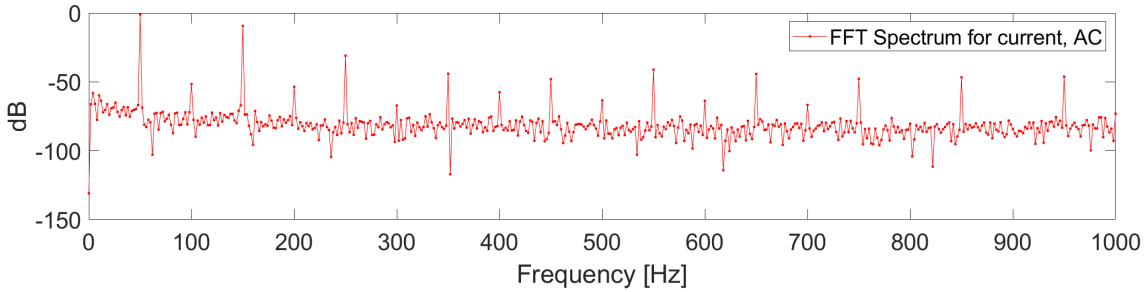

Figure 4.17: FFT analysis of the 20 first harmonic components for the input current, 0° phase shift.

In Figure 4.18 the measured waveforms are presented for a phase shift of 60°. It is observed that the current at the zero crossings has increased, compared to Figure 4.15, and that the input current is not as sinusoidal. The transients at the zero crossing reached a maximum value of ±3.5 A. Additionally, it was noticeable that the current (blue curve) did not align with the signal sent to the VINAC pin (black curve).

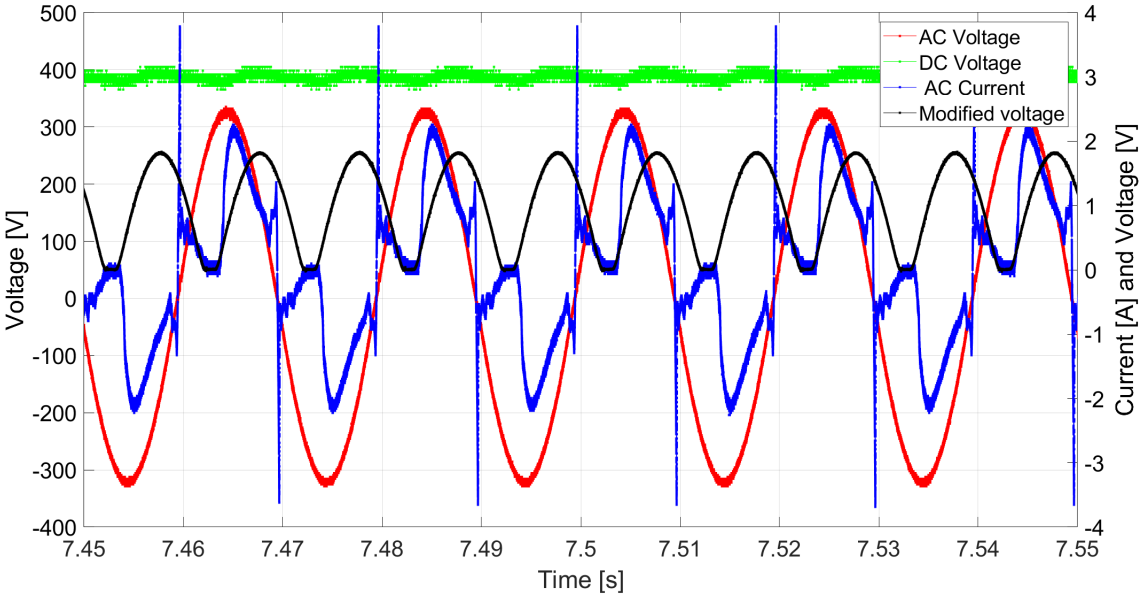

Figure 4.18: Measured voltages and current for 60° phase shift.

In Figure 4.19 the complete FFT of the signal is displayed, while Figure 4.20 represents the 20 first harmonic components of the current. The fundamental component was calculated to an RMS value of 0.935 A and the total RMS current was calculated to 1.155 A. The THD of the input current at 60° was 72.6 % and the total power factor was 0.787.

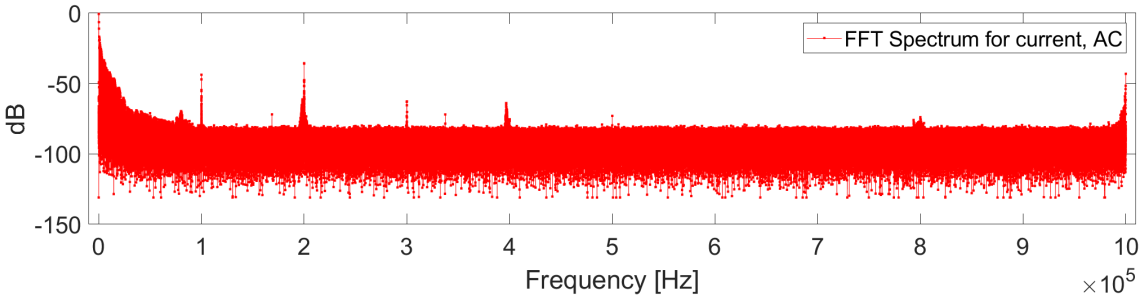

Figure 4.19: Whole FFT spectrum of the input current at 60° phase shift.

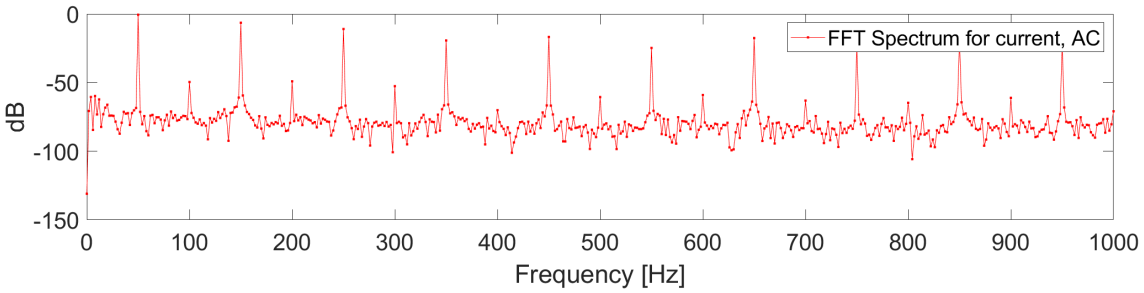

Figure 4.20: FFT analysis of the 20 first harmonic components for the input current, 60° phase shift.

The rest of the measurements are summarized in Table 4.3, where the outcome was the same for both negative and positive phase inputs. The table indicates a decrease in the distortion power factor as the phase input increases, dropping from 0.932 to 0.810. Simultaneously, the displacement power factor is reduced from 1 to 0.972.

Table 4.3: Performance of the converter for various phase shift inputs.

VINAC [°]	Current [°]	I_{in} [A]	$I_{in_{1st}}$ [A]	I, THD [%]	V, THD [%]	$PF_{distortion}$	$PF_{displacement}$	PF_{total}
0	0	0.947	0.882	38.87	15.44	0.932	1	0.932
10	0.72	0.951	0.882	40.34	15.59	0.927	0.999	0.927
20	0.74	0.966	0.885	43.92	15.50	0.916	0.999	0.915
30	0.9	0.984	0.891	46.66	15.52	0.906	0.999	0.906
40	3.9	1.022	0.910	50.97	15.53	0.891	0.998	0.888
50	6.7	1.054	0.920	55.78	15.55	0.873	0.993	0.867
55	9.9	1.077	0.926	59.35	15.68	0.860	0.985	0.847
60	13.5	1.155	0.934	72.60	15.82	0.810	0.972	0.787

4.2.4 Temperature

Figure 4.21 shows the IR picture of the EVM kit at a phase shift of 0°. The varistor reached a temperature of around 45 °C and the inductors reached a temperature of approximately 30 °C.

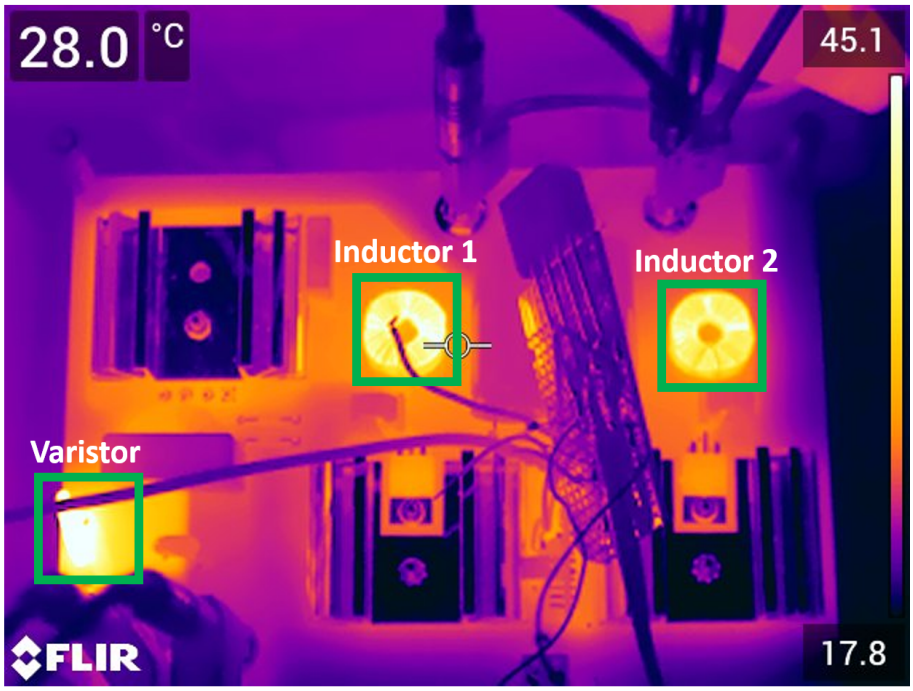

Figure 4.21: IR picture of the converter, 0° phase shift.

At a phase shift of 30°, see Figure 4.22, the varistor reached a temperature around 68 °C while the inductors reached a temperature of approximately 55 °C.

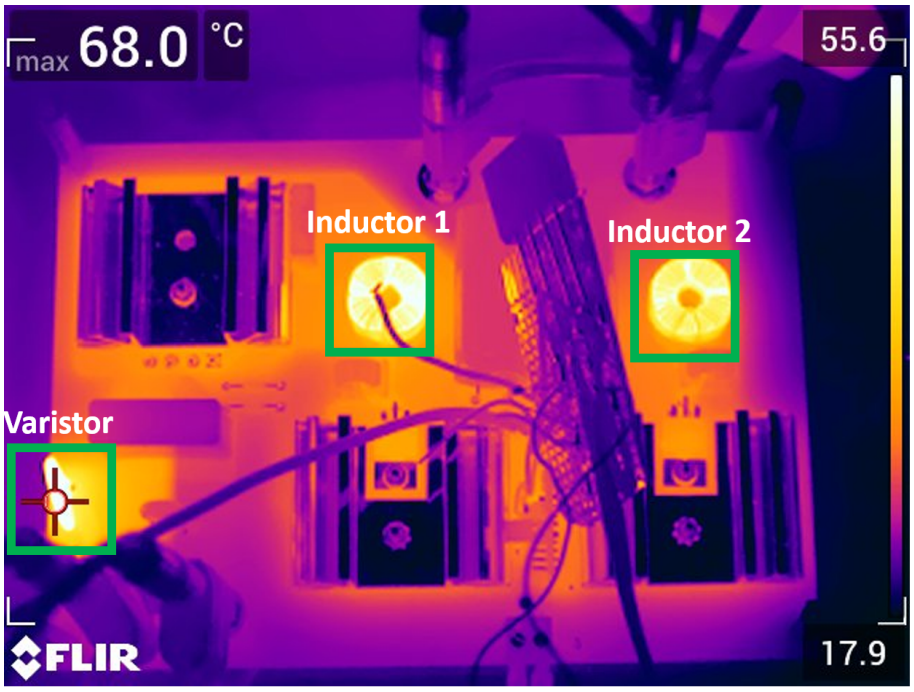

Figure 4.22: IR picture of the converter, 30° phase shift.

When having a phase shift of 60°, see Figure 4.23, the varistor reached a temperature around 93 °C while the inductors reached a temperature of approximately 65 °C.

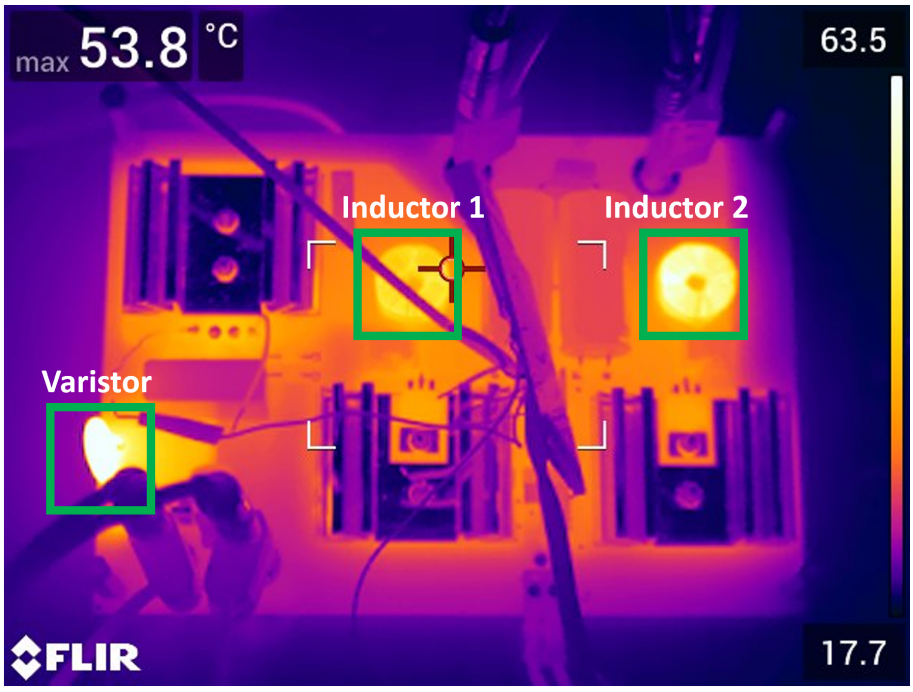

Figure 4.23: IR picture of the converter, 60° phase shift.

From the results of the infrared temperature test, it can be concluded that the varistor, located at the input, and the inductors, within the boost stage, experienced the

most heat dissipation. Yet the components still remained within their specific operating temperatures, presented in 3.5.4. Note that the temperature range in the pictures is not correct due to the hotspot detection points.

4.2.5 Microgrid

Figure 4.24 illustrates the baseline scenario of the microgrid test, achieving a power factor of 0.197 and a THD of 24.15 %. The current drawn by the fluorescent lights is represented by the yellow curve, and the grid voltage is depicted by the red curve. The RMS current drawn from the lights was 1.59 A.

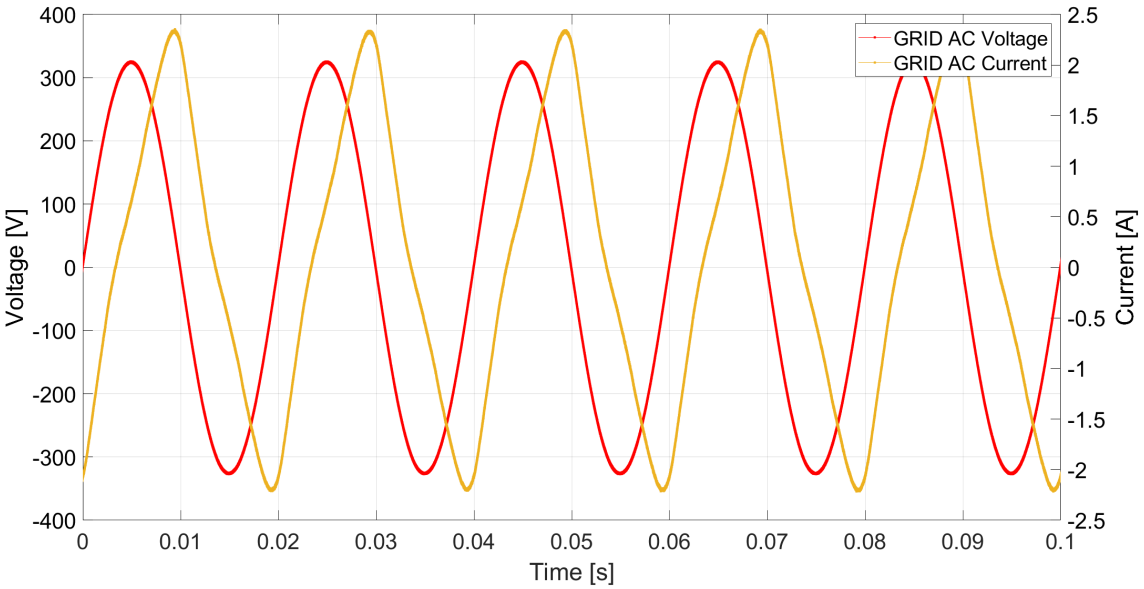

Figure 4.24: Measured voltage and current displayed for the microgrid with no AC/DC converter connected.

4.2.5.1 Microgrid, output current 0.05 A

Figure 4.25 displays the waveforms for a phase shift of 0° with a DC side current of 0.05 A, corresponding to an RMS current of 0.111 A on the AC side. It is evident that the grid current was phase-shifted relative to the grid voltage.

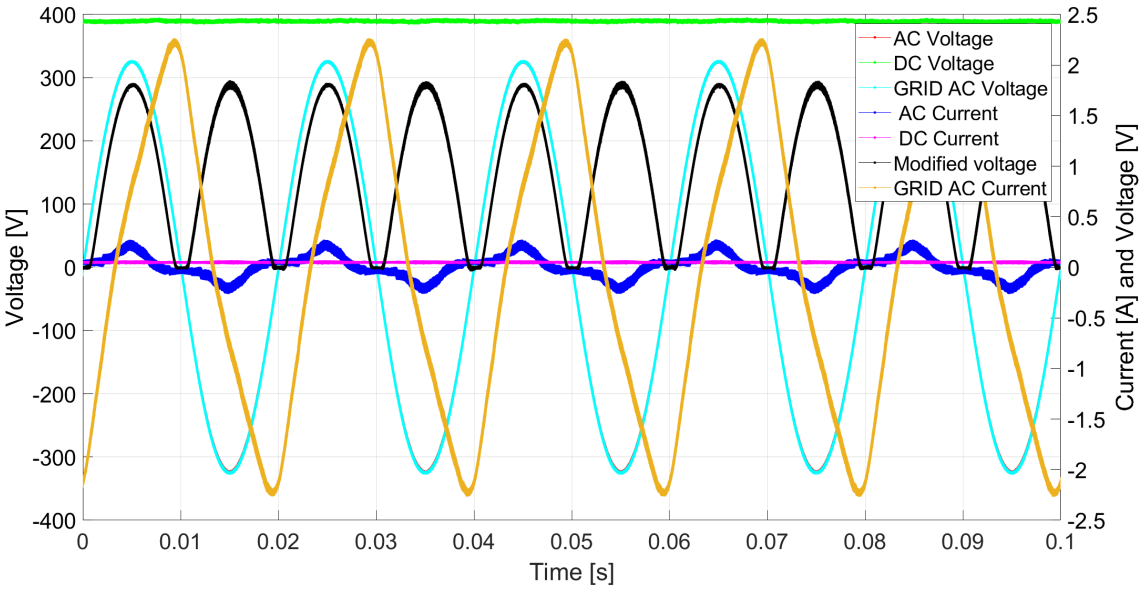

Figure 4.25: Measured voltages and currents for the microgrid, $I_{out} = 0.05$ A and 0 ° phase shift from the converter.

The FFT spectrum for the grid current is presented in Figures 4.26 and 4.27.

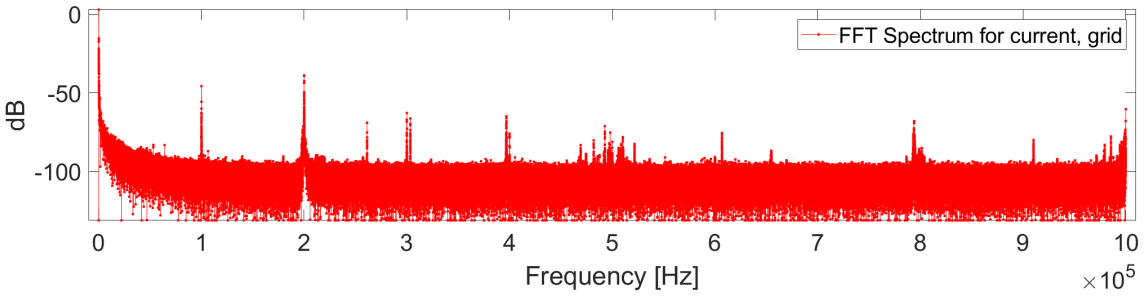

Figure 4.26: Whole FFT spectrum of the grid current at 0° phase shift, $I_{out} = 0.05$ A.

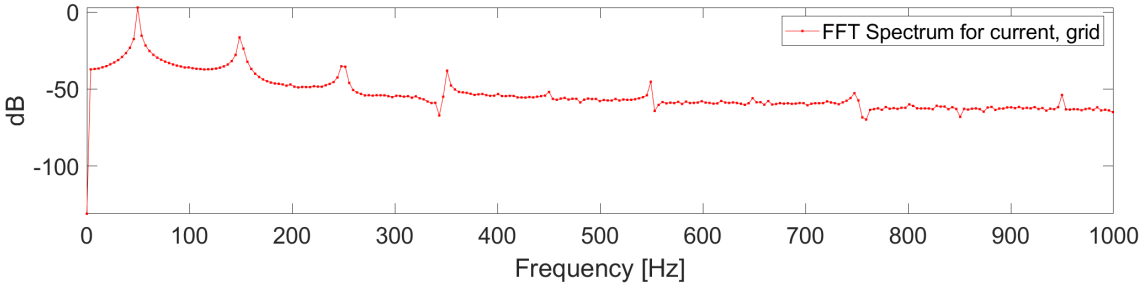

Figure 4.27: FFT analysis of the 20 first harmonic components for the grid current at 0° phase shift, $I_{out} = 0.05$ A.

Table 4.4 provides a summary of the various scenarios, illustrating that the power factor slightly increased relative to the baseline case when a phase shift of either

-30° or +60° was introduced. The power factor increased from 0.178 to 0.182 for the -30° case, while it went from 0.178 to 0.186 for the 60° case. Additional data for the waveforms is presented in B.2.1, illustrating phase shifts of ±60°.

Table 4.4: Behavior of the microgrid for various phase shift inputs, $I_{out} = 0.05$ A.

VINAC [°]	Current [°]	I_{in} [A]	$I_{in_{1st}}$ [A]	THD [%]	$PF_{distortion}$	$PF_{displacement}$	PF_{total}	$V_{out,Ripple}$ [%]	$I_{out,Ripple}$ [%]
-60	-13.63	1.40	1.35	26.17	0.967	0.179	0.173	2.57	54.46
-30	-4.82	1.42	1.38	24.22	0.972	0.187	0.182	2.16	52.96
0	-1.86	1.43	1.39	23.53	0.973	0.186	0.178	2.36	50.78
30	4.36	1.44	1.41	22.53	0.976	0.176	0.173	2.36	52.37
60	16.21	1.46	1.42	22.65	0.975	0.191	0.186	2.05	57.25

4.2.5.2 Microgrid, output current 0.145 A

Figure 4.28 displays the waveforms for a phase shift of 0° with a DC side current of 0.145 A, corresponding to an RMS current of 0.289 A on the AC side. It is evident from these observations that the grid current was phase-shifted in relation to the grid voltage.

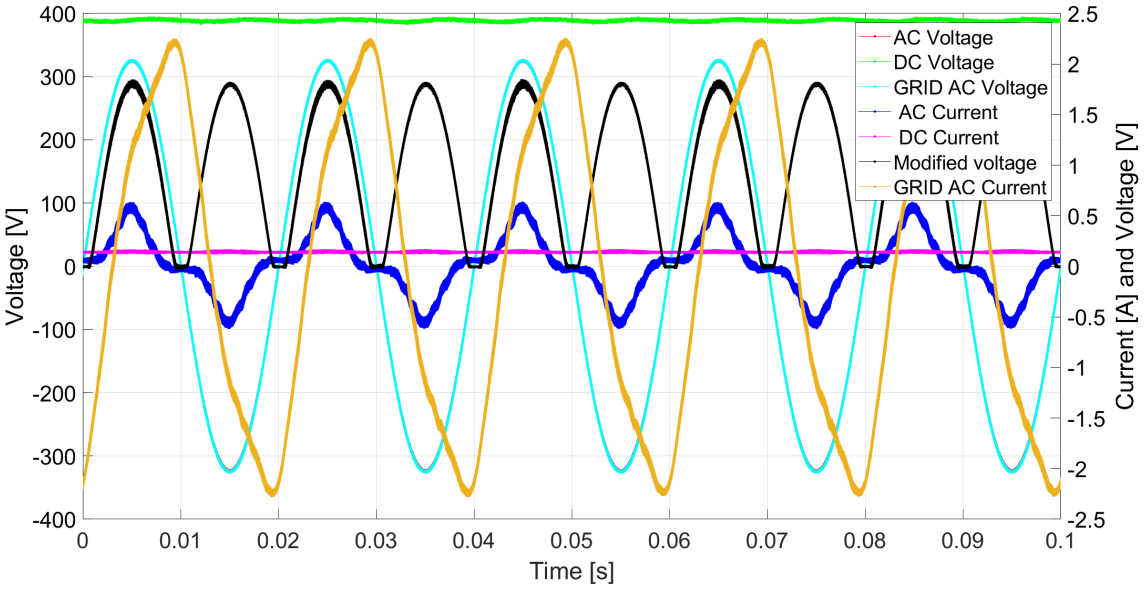

Figure 4.28: Measured voltages and currents for the microgrid, $I_{out} = 0.145$ A and 0 ° phase shift from the converter.

The FFT spectrum for the grid current is presented in Figures 4.29 and 4.30.

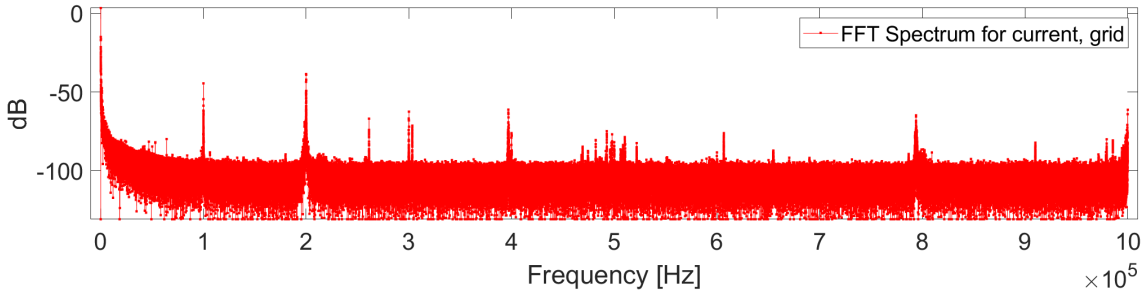

Figure 4.29: Whole FFT spectrum of the grid current at 0° phase shift, $I_{out} = 0.145$ A.

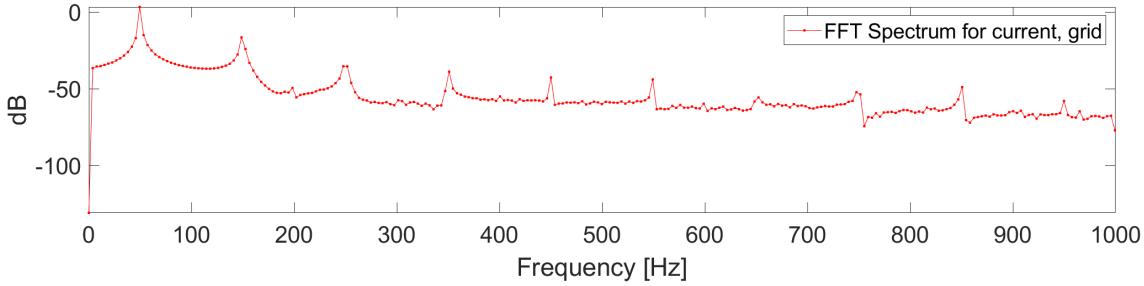

Figure 4.30: FFT analysis of the 20 first harmonic components for the grid current at 0° phase shift, $I_{out} = 0.145$ A.

Table 4.5 presents a summary of the different cases, indicating that the power factor improved when a phase shift was applied to the input current. The highest power factor, 0.328, was achieved with a phase shift of 60°. Additional data for the waveforms is presented in B.2.2, illustrating phase shifts of ±60°.

Table 4.5: Behavior of the microgrid for various phase shift inputs, $I_{out} = 0.145$ A.

VINAC [°]	Current [°]	I_{in} [A]	$I_{in_{1st}}$ [A]	THD [%]	$PF_{distortion}$	$PF_{displacement}$	PF_{total}	$V_{out,Ripple}$ [%]	$I_{out,Ripple}$ [%]
-60	-19.96	1.43	1.37	30.56	0.956	0.254	0.243	2.99	25.52
-30	-3.8	1.48	1.43	25.13	0.970	0.228	0.221	2.98	25.74
0	-2.12	1.51	1.47	23.11	0.974	0.193	0.188	2.88	25.17
30	7.15	1.55	1.52	21.25	0.978	0.246	0.240	2.88	26.85
60	19.40	1.60	1.56	22.39	0.976	0.336	0.328	2.88	27.56

4.2.5.3 Microgrid, output current 0.5 A

Figure 4.31 displays the waveforms for a phase shift of 0° with a DC side current of 0.5 A, corresponding to an RMS current of 0.977 A on the AC side. It was observed that the grid current was less phase-shifted relative to the grid voltage in comparison to Figures 4.25 and 4.28.

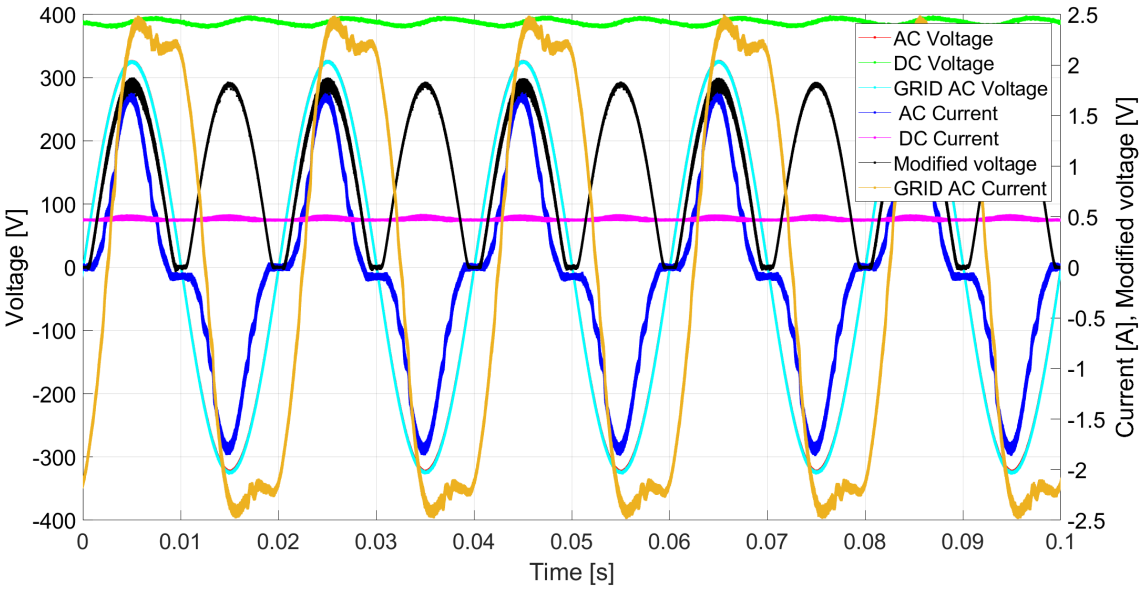

Figure 4.31: Measured voltages and currents for the microgrid, $I_{out} = 0.5$ A. 0 ° phase shift from the converter.

The FFT spectrum for the grid current is presented in Figures 4.32 and 4.33.

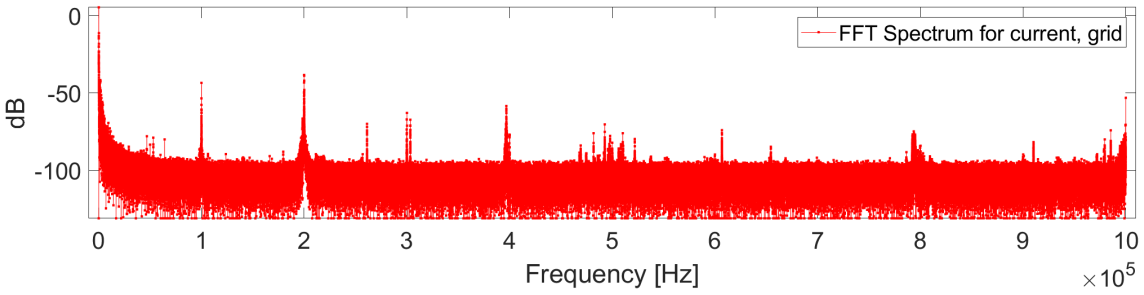

Figure 4.32: Whole FFT spectrum of the grid current at 0° phase shift, $I_{out} = 0.5$ A.

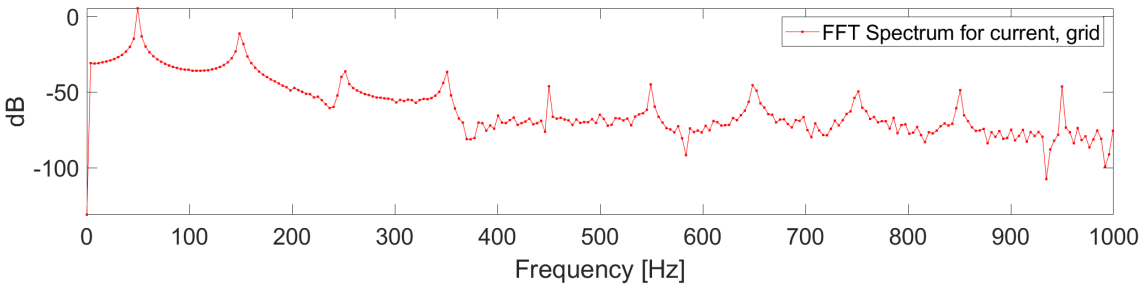

Figure 4.33: FFT analysis of the 20 first harmonic components for the grid current at 0° phase shift, $I_{out} = 0.05$ A.

In Table 4.6 a summary of the different cases is presented. The highest power factor, 0.951, was achieved with a phase shift of -30°, while the lowest power factor,

0.839, was achieved at 60°. Additional data for the waveforms is presented in B.2.3, illustrating phase shifts of ±60°.

Table 4.6: Behavior of microgrid for various phase shift inputs, $I_{out} = 0.5$ A.

VINAC [°]	Current [°]	I_{in} [A]	$I_{in_{1st}}$ [A]	THD [%]	$PF_{distortion}$	$PF_{displacement}$	PF_{total}	$V_{out,Ripple}$ [%]	$I_{out,Ripple}$ [%]
-60	-15.23	1.73	1.57	45.59	0.910	0.984	0.895	5.46	15.87
-30	-5.01	1.81	1.72	32.27	0.952	0.999	0.951	5.24	14.6
0	13.48	1.91	1.85	26.24	0.967	0.971	0.940	4.95	13.68
30	13.85	2.05	1.99	25.07	0.970	0.963	0.934	5.26	14.62
60	14.39	2.24	2.11	37.17	0.937	0.895	0.839	5.14	16.21

4.2.6 Maximum phase shift for different loads

In Figure 4.34, it is observed that the maximum attainable phase shift for full power, 300 W, was 43.2° which resulted in a phase shift between the current and the voltage of 3.1°.

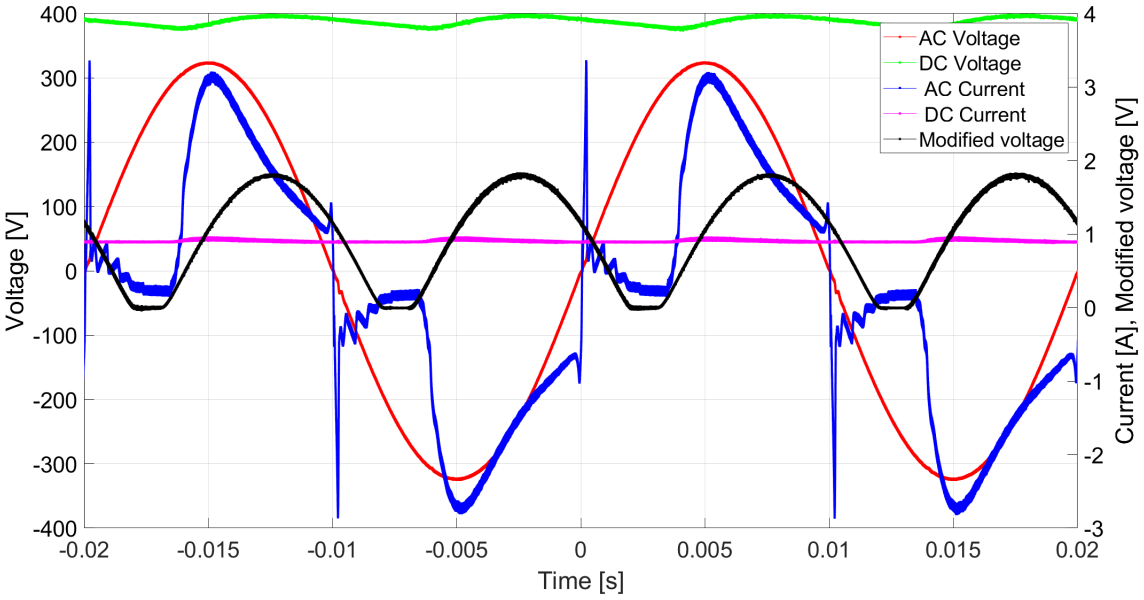

Figure 4.34: Measured maximum phase shift of the converter at full load, 300 W.

In Figure 4.35, it is observed that the maximum attainable phase shift for half the maximum power, 150 W, was 61.2° which resulted in a phase shift between the current and the voltage of 16.9°.

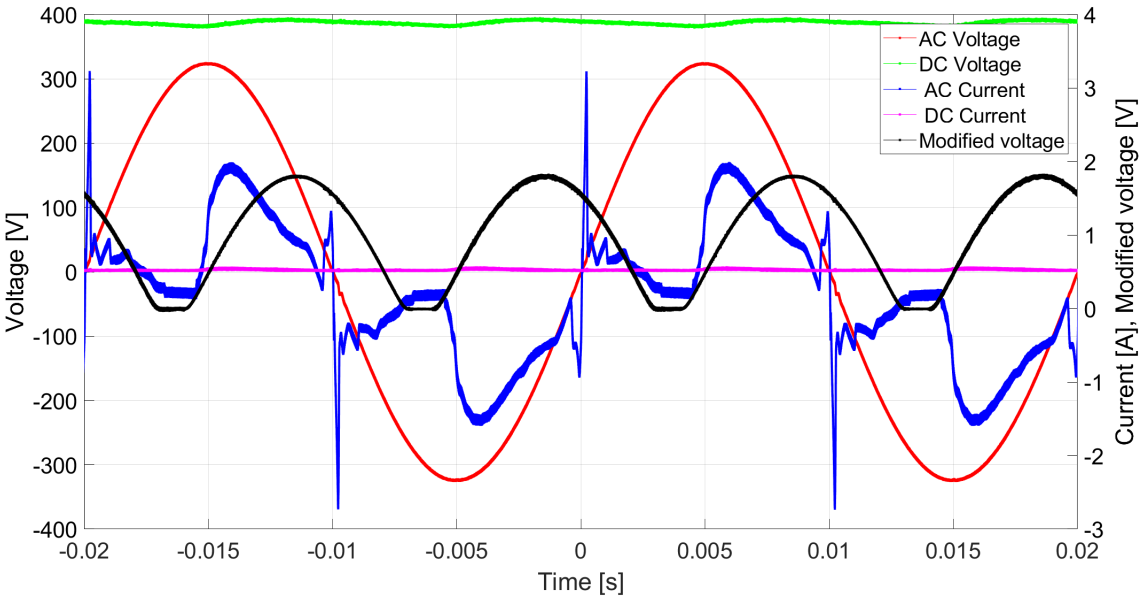

Figure 4.35: Measured maximum phase shift of the converter at half load, 150 W.

4.2.7 Line Regulation

For a half load of 150 W, all the three input voltage cases, 85 V, 175 V and 265 V exhibited a constant output voltage of 390 V for 0° and 30°. Only the input voltage of 265 V was tested for 60° due to the transient magnitude became too large in the other two cases.

At a full load of 300 W and an input voltage of 85 V, the converter failed to maintain stable line regulation. With a 0° phase shift, the output voltage was 226.2 V, which decreased to 199.3 V when the phase shift was adjusted to 30°. However, at the higher input voltages of 175 V and 265 V, the output voltage consistently remained at 390 V regardless of the applied phase shift. Similarly as for the half load case, only a phase shift of 60° was tested on an input voltage of 265°, due to the transient magnitude on the other two cases.

4.2.8 Input voltage distortion

Figure 4.36 shows that the voltage distortion was not affected by the phase shift and there was a THD of approximately 15.5 %.

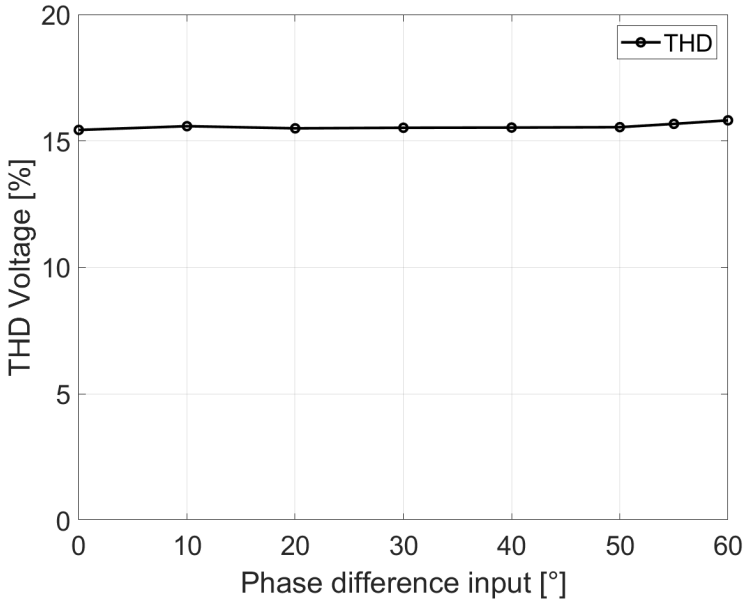

Figure 4.36: Measured THD of the input voltage for different phase shifts.

4.2.9 Load regulation

The output voltage is presented in Figure 4.37 for the different loads and phase shifts.

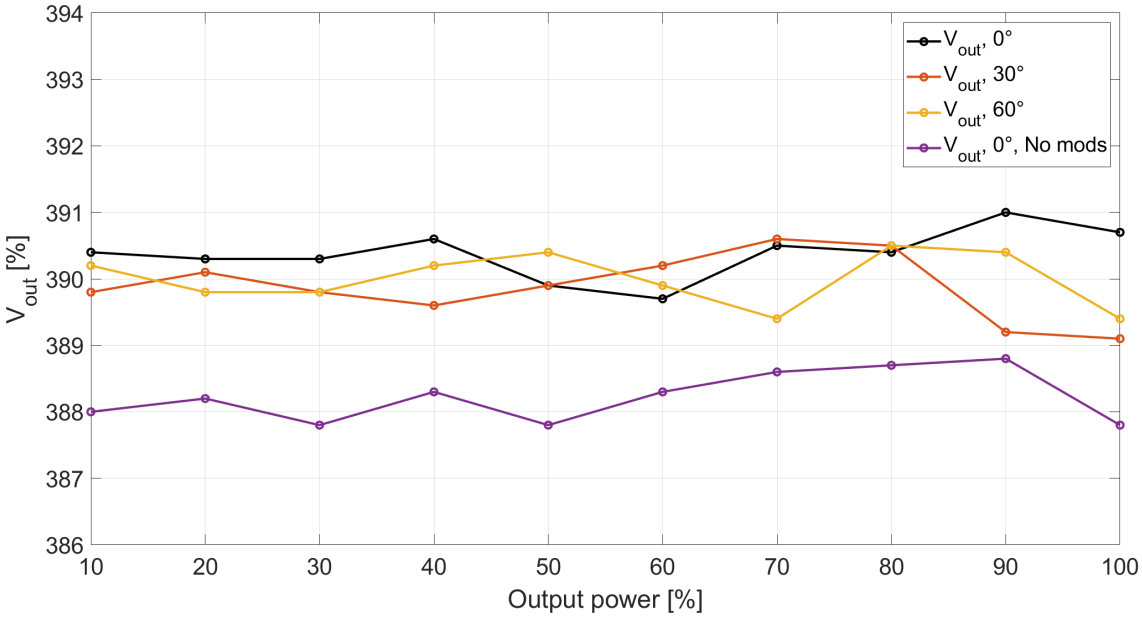

Figure 4.37: Measured output voltage, V_{out}, during different loads and phase shifts.

The lowest output voltage, 387.8 V, was obtained when the input phase shift remained at 0° without any modifications done to the circuit. Conversely, the highest output of 391 V was achieved when the input phase shift was manually adjusted to 0°.

4.2.10 Output voltage and output current ripple

In Figure 4.38 the output current ripple can be observed for the different loads and phase shifts. It can be observed that the output current ripple decreased with increasing load. This concept applies to all phase shifts, where an increase in phase shift results in a slightly higher output current ripple. It can be noted that the output current ripple reached a maximum of 39.3 % at minimum load, 10 %, and a phase shift of 0°. The minimum ripple was 10.1 % and occurs at maximum load, 100 %, and phase shift of 0° with no modifications.

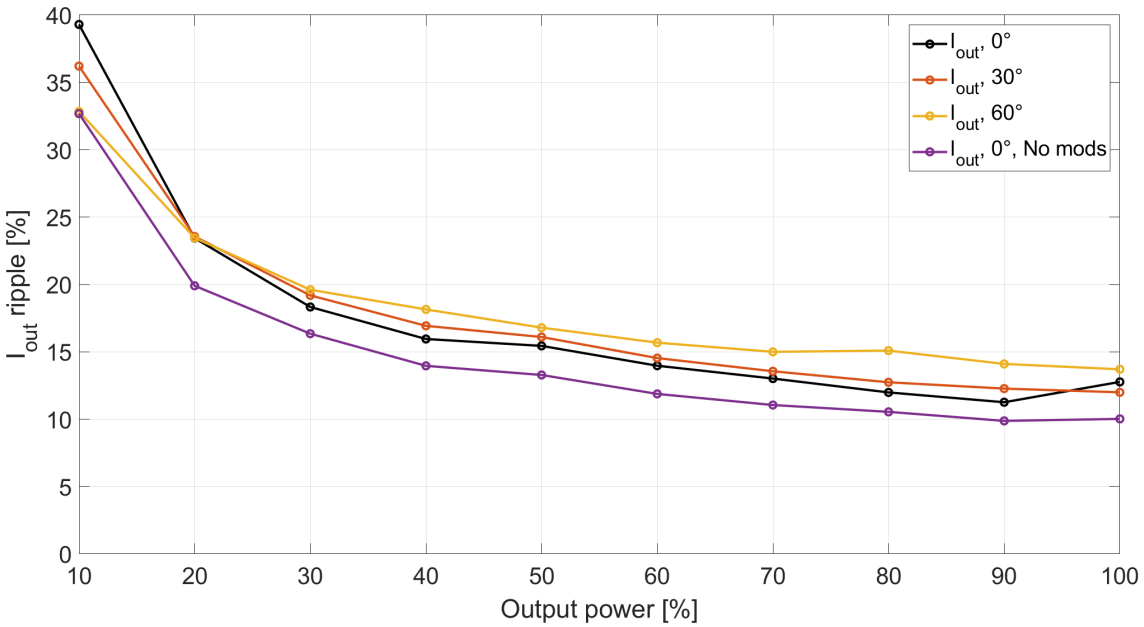

Figure 4.38: Measured output current ripple, $I_{out,Ripple}$, during different loads and phase shifts.

In Figure 4.39 the output voltage ripple can be observed for the different loads and phase shifts. The output voltage ripple increased with an increasing load. It can be observed that the output voltage ripple reached a maximum of 6.8 % at maximum load and a phase shift of 30°. A minimum of 2.36 % ripple was observed at a load of 10 % and phase shift of 0°.

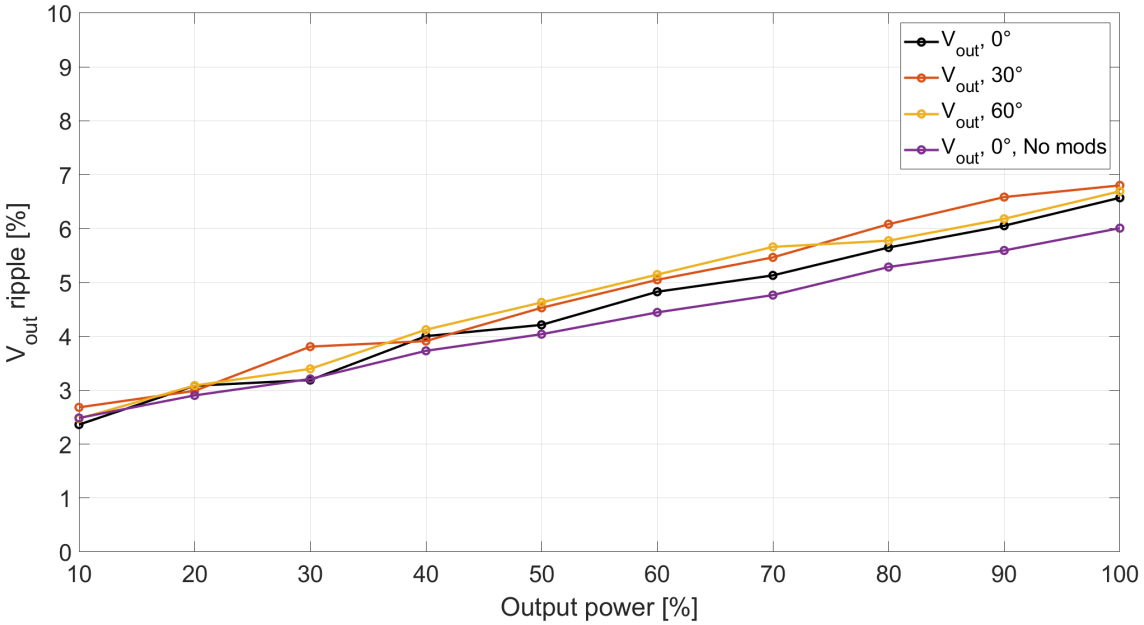

Figure 4.39: Measured output voltage ripple, $V_{out,Ripple}$, during different loads and phase shifts.

4.2.11 1:1 proportionality

The proportionality between the input current and VINAC signal, for an input voltage of 85 V and a load of 150 W, is presented in Figure 4.40.

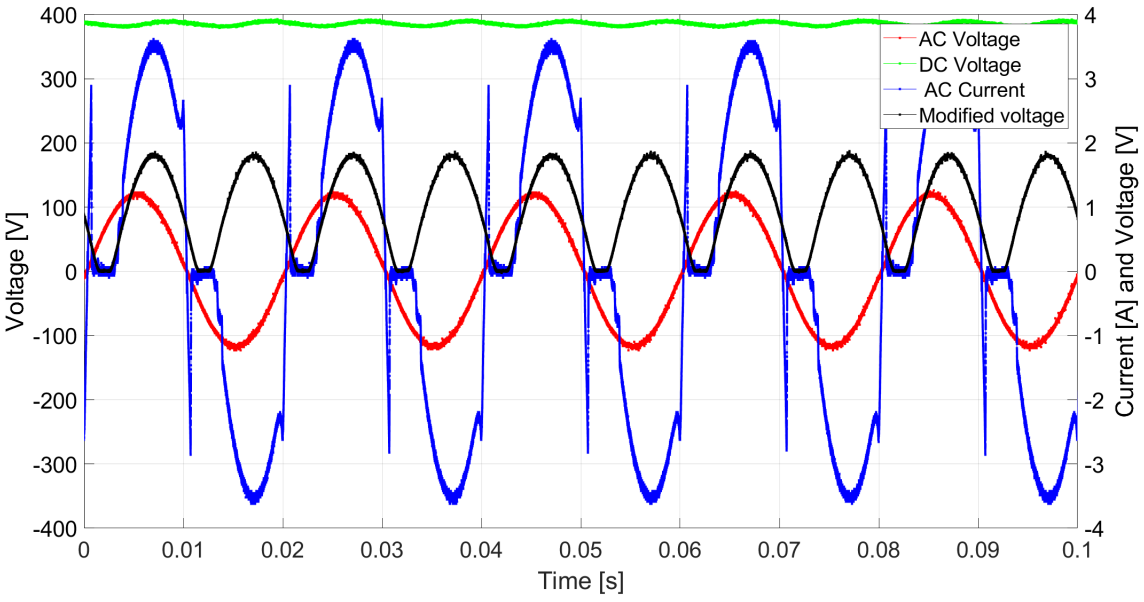

Figure 4.40: Measured current and VINAC proportionality, V_{in} = 85 V and P_{out} = 150 W.

The proportionality between the input current and VINAC signal, for an input voltage of 85 V and a load of 300 W, is presented in Figure 4.41

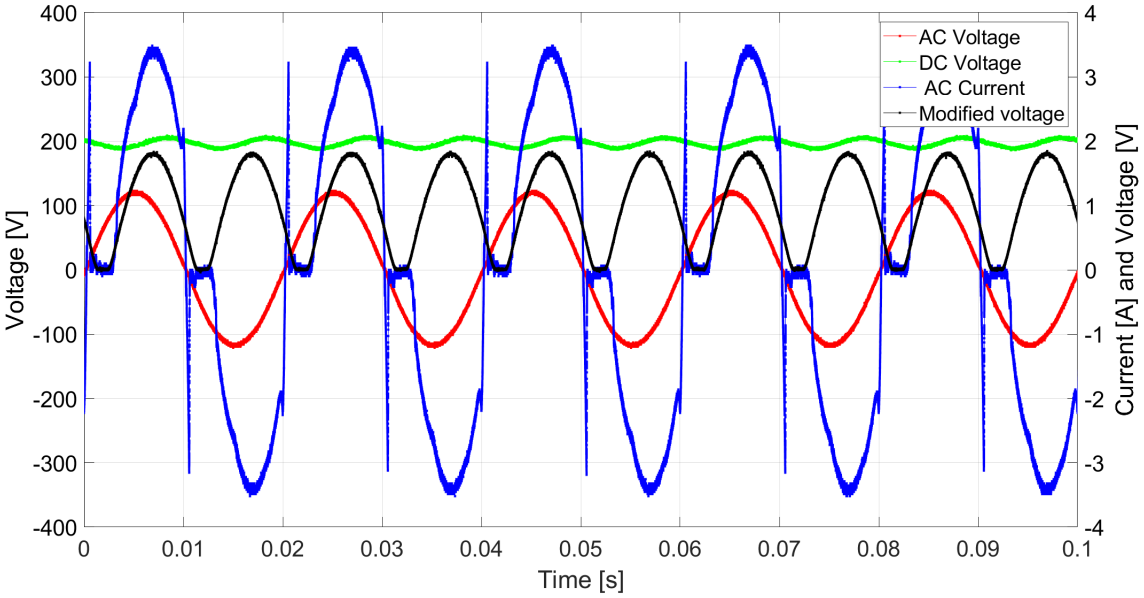

Figure 4.41: Measured current and VINAC proportionality, V_{in} = 85 V and P_{out} = 300 W.

It is noted from Figure 4.42 that the 1:1 proportionality between the current and VINAC signal decreased at an input voltage of 165 V.

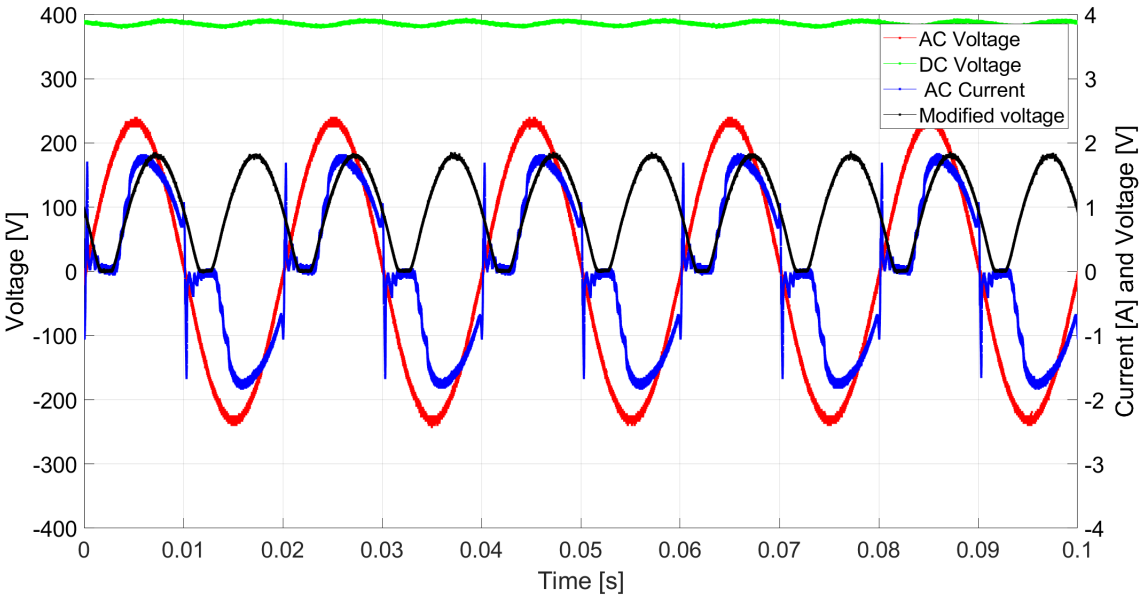

Figure 4.42: Measured current and VINAC proportionality, V_{in} = 165 V and P_{out} = 150 W.

The proportionality between the input current and VINAC signal, for an input voltage of 165 V and a load of 300 W, is presented in Figure 4.43

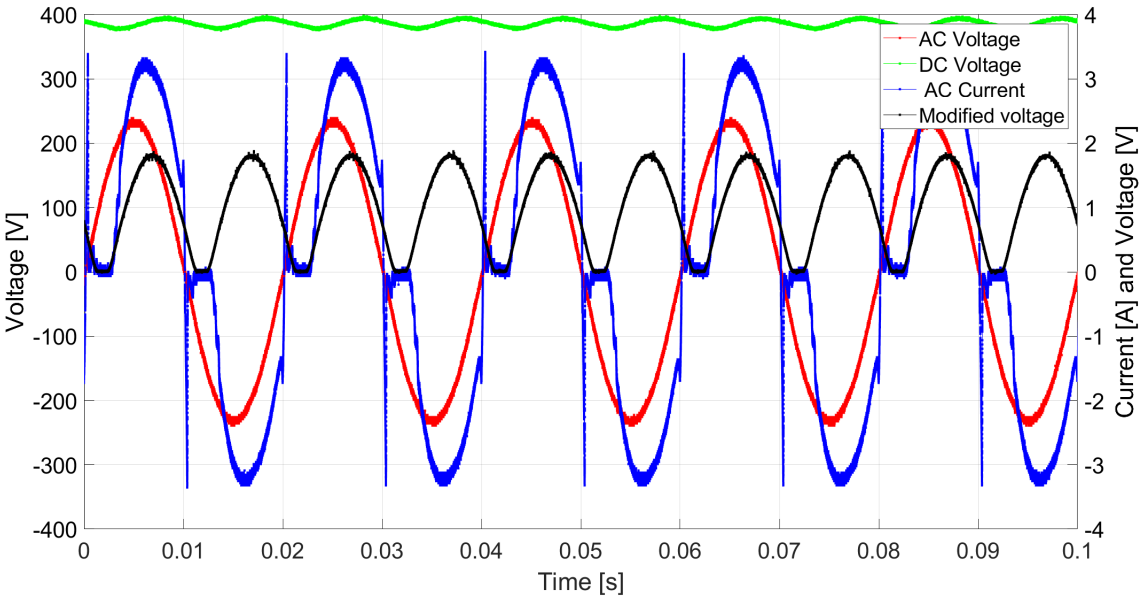

Figure 4.43: Measured current and VINAC proportionality, V_{in} = 165 V and P_{out} = 300 W.

All results from the proportionality measurements are presented together in Table 4.7.

Table 4.7: Voltage and Current Phase Shifts.

Voltage [V]	**Power [W]**	**VINAC [°]**	**Current phase shift [°]**
85	150	37.9	37.9
85	300	35.3	35.3
165	150	40.2	16.2
165	300	36.4	17.7

4.3 Digital Results

The signals from the current- and voltage measurement sensors are presented in Figure 4.44 while the PFC is switched off. There was no present noise and a phase shift between the actual voltage signal (red) and the measured signal (black) was denoted. The measured signals were scaled relative to the actual signals because the microcontroller's limited measuring ability.

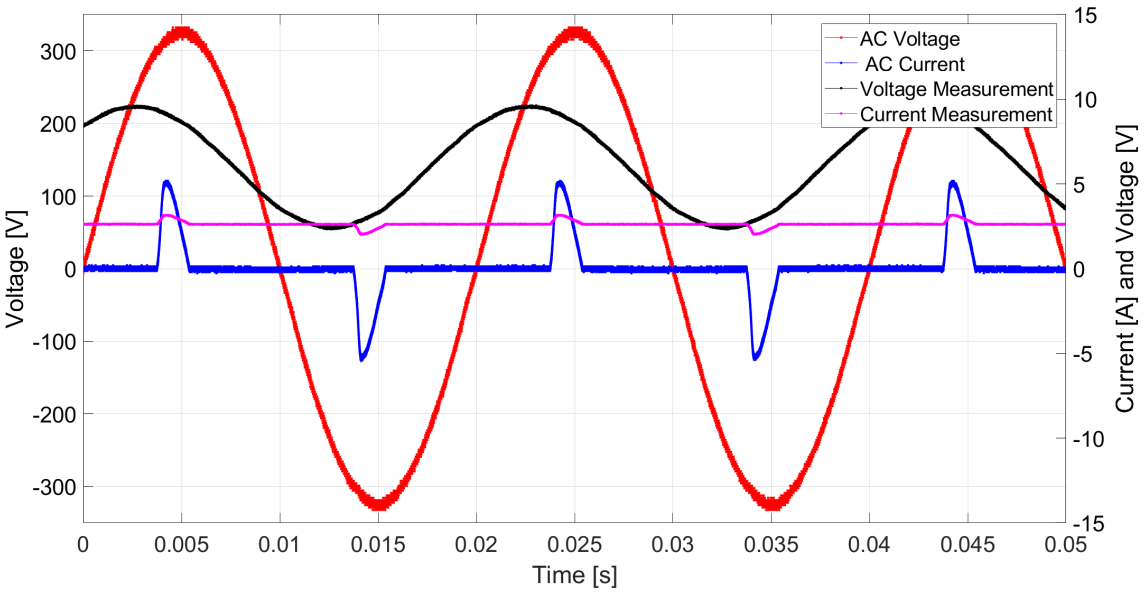

Figure 4.44: Voltage and current measurements using sensor modules with the PFC switched off.

In Figure 4.45 the PFC was switched on and the current measurement is amplified five times. It can be denoted that noise was present in the current measurement signal.

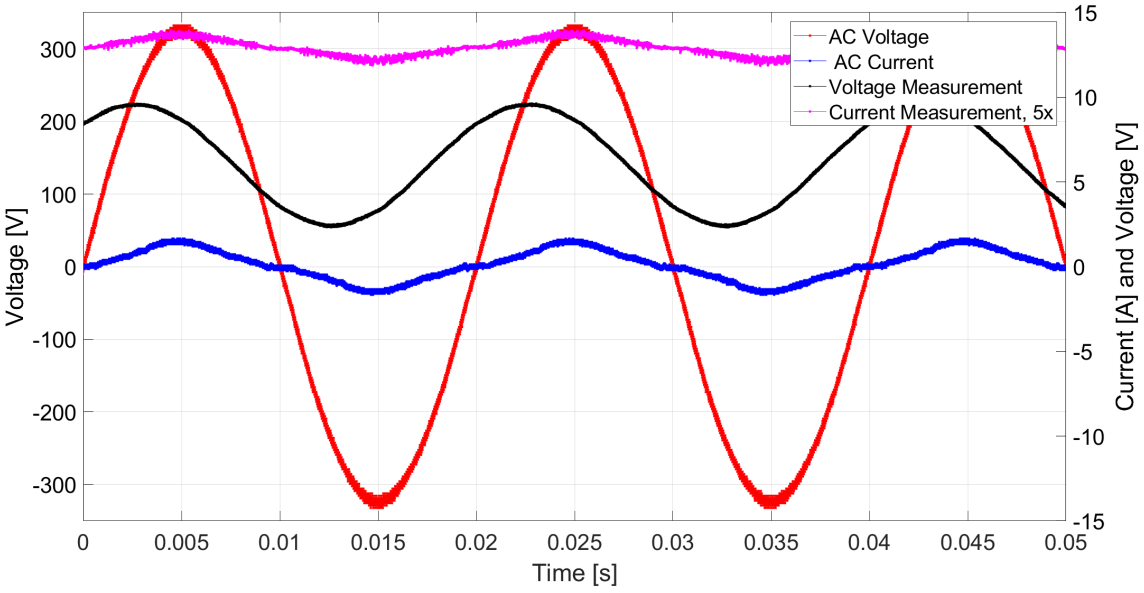

Figure 4.45: Voltage and current measurements using sensor modules, with the PFC switched on. The current measurement is amplified 5 times.

The DAC output of the microcontroller is presented in Figure 4.46 as the pink curve, the output is a rectified sine wave.

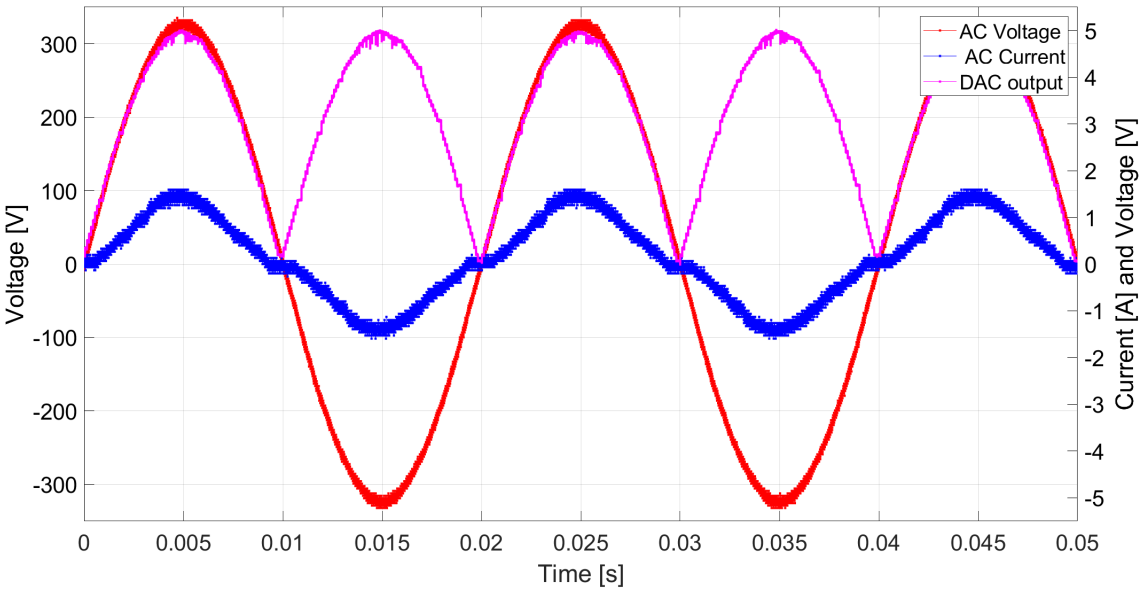

Figure 4.46: Measured output signal from microcontroller utilizing the DAC.

4.4 Demand and application for applicable grid services

The function of the AC/DC converter with a user-defined power factor, enabled a phase-shift of the current relative to the voltage. This facilitated a power factor adjustment that compensated for the inductive or capacitive characteristics of the grid. Based on the measurement results, presented in 4.2, the conceptual theory of the AC/DC PFC boost converter with user defined PFC, seemed feasible. Due to the increased implementation of renewable energy sources, presented in section 2.10, there is a demand for an equivalent product. Consequently, the application of such a product could ease the transition towards a more sustainable and renewable electricity grid.

4.5 Grid stabilization opportunities with Ericsson's base stations

A possible applicable scenario of the AC/DC converter with variable power factor is in Ericsson's base stations, presented in chapter 2.10.3. Such an application could be illustrated in Figure 4.47, resulting in a net power factor closer to one on the grid side, demonstrated in section 4.2.5. This enhanced the efficiency of the local grid at the cost of a reduced efficiency in the converter, see section 4.2.2. The phase compensation also implied increased stress on the converters components in terms of ripple and temperature, see section 4.2.10 and 4.2.4.

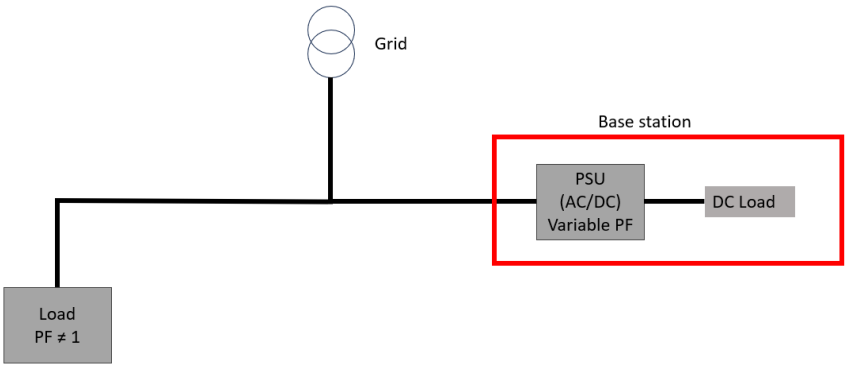

Figure 4.47: Block diagram with load and base station combined.

5
Discussion

5.1 Simulations

From the LTspice results presented in 4.1, the feasibility behind the theory of an AC/DC converter with adjustable power factor was validated. The behavioral simulation model showed a good possibility of achieving the desired PF though phase shifting the current. In the simulation model, the current was phase-shifted in direct proportion to the voltage waveform of the VINAC pin. This differs from the real-world prototype results presented in 4.2. For input voltages above 165 V the current experienced a smaller phase shift relative to the voltage.

Another thing that could be observed was the transients at the zero crossings. In the simulation model there was only one noticeable transient, whereas the prototype experienced more distortions and larger transients. Naturally, this is due to the ideal behaviour of the simulation model, which therefore offers a much larger possible phase shift compared to the prototype. The harmonic current content for the simulation model was also studied through the FFT function. As expected, the harmonics increased with the amount of phase shift applied, mainly due to the transients occurring at the zero crossings. Overall, a larger THD was seen in the prototype compared to the simulation, for the same current phase shift. This was mainly due to the increased distortions at the zero crossings in the prototype.

It should be noted that the LTspice model was only made for validating the initial theory of an possible phase shift between the current and voltage. While utilizing approximately the same control strategy as the UCC28070, the components were designed to make the model run smooth and not to emulate the real world prototype. Therefore, large values are be seen in components such as the two interleaved inductors and the bulk capacitor.

5.2 Discussion of prototype measurements

In the following section, a discussion regarding the measured results from section 4.2 will be presented in the same order.

5.2.1 Power factor

The power factor for the converter, presented in 4.2.1, increased with increased load. It implies that less reactive power is used, increasing the efficiency. This could be due to that the converter is operating in more favorable operating conditions, increasing its performance. Naturally, the power factor decreased of the converter when introducing a phase shift, as the reactive power consumption increased.

5.2.2 Efficiency

From the efficiency results, seen in section 4.2.2, it could be seen that the efficiency increased with a greater load. This is due to that the losses in the converter, such as switching-, conduction-, and magnetic losses, are fairly constant or decreased with increased load. Consequently, as the input power is increased, it results in a greater efficiency as the ratio between P_{out}/P_{in} is increased.

Since it was not possible to monitor each type of loss individually, only the total power loss was measured, rather than specific losses. The switching losses are occurring during the transitions of the power switches, proportional to the switching frequency. With an increased load, the duty cycle changes, affecting the losses. The conduction losses are dependent on the finite resistance in the conductors and switches, which are increasing with a greater load. The magnetic losses occur in the inductors and transformers. As anticipated, the efficiency decreased in the converter when introducing a phase shift between the current and voltage. The lowest efficiency, 70.7 % , was observed at a phase shift of 60° and a load of 80 %. Therefore the reasoning regarding that a higher load would lead to increased efficiency was proved invalid. This was attributed to the fact that the current waveform became more distorted under heavier loads for such a high phase shift.

5.2.3 Harmonics

Another important aspect, especially regarding the regulatory requirements, are the harmonics. Presented in section, 4.2.3, the 50 Hz component is identified as the fundamental frequency. This naturally corresponds to the dominant frequency of the alternating current signal of 50 Hz. The higher order harmonics are observed at multiples of the fundamental frequency, for example at 100 Hz, 150 Hz, 200 Hz and so on. These are generally lower in amplitude, but still contribute to distortions in the waveform. Note from the theory, presented in 2.6.1, that the more closely the input current of the converter matches a sine wave, the more effective the cancellation of the even harmonics is. As increased phase shift is applied, the current becomes less sinusoidal and the harmonics become more dominant. This is the most harmonics appear at the highest phase shift. In an ideal case, the current waveform would be purely sinusoidal at 50 Hz.

Beyond the harmonics related to the fundamental frequency of the AC input signal, switching converters also introduce harmonics related to their switching frequency. This can be seen at 200 kHz in the different figures representing the FFT, for exam-

ple, Figure 4.16. Based on the application of the converter, and consequently the desired phase shifting ability, filters might need to be introduced to suppress the harmonics. This is related to the once again, regulatory requirements, introduced in section 2.8.3. Note that the results could be seen as a benchmark in regards to the regulations, due to that the requirements for measuring EMI were not fulfilled.

5.2.4 Temperature

The temperature, measured by the infrared thermometer for the three various phase shifts (0°, 30°, and 60°), exhibited the anticipated behavior. As seen in section 4.2.4, the temperature was at its lowest for the base case with a 0 ° phase shift. Subsequently, it gradually increased with the application of a greater phase shift. The temperature never reached levels that could potentially damage the components, indicating that the converter was suitable for the three different test setups. As expected, the two inductors in the EVM, see Figure 4.2.4, experienced the most heat generation with increasing phase shift. This was due to the rise in current harmonics, which led to an increase in ripple with the increased phase shift. Another more unusual result was that the varistor also increased in temperature with increased phase shift. While the explanation is not as clear, it might be due to voltage spikes that are occurring with the phase shift. These spikes would cause the varistor to absorb more energy, leading to an increase in its temperature.

However, it is worth noting that in a real-world application, the converter would likely be enclosed within a protective box of some sort, leading to increased temperatures within the converter. Consequently, further studies would be required to assess whether additional cooling measures would be necessary.

5.2.5 Microgrid

In section 4.2.5, it was seen that the converter practically was able to create a local phase compensation according the underlying theory. One key observation was however that the phase shifting ability of the converter depended on the magnitude of the current from the converter in regards to the grid current. A high converter current indicated that a significant phase compensation could be achieved. Conversely, a lower converter current resulted in a limited phase compensation. This implies that if the desire is to achieve a significant phase compensation on the grid side, it may necessitate the connection of multiple converters to obtain a higher total converter current.

It should be noted that the total power factor is the product of the distortion- and displacement power factor, in accordance to (2.8). The distortion power factor is influenced by the waveform shape, whereas the displacement power factor depends on the time difference between the current and voltage waveforms. This highlights the necessity of considering both factors when optimizing the power factor through phase shifting. Therefore, in efforts to achieve an effective local phase compensation for an inductive grid, it is necessary to adjust the converter to a capacitive

behaviour, while simultaneously consider the shape of the waveform. Conversely, if the grid is capacitive, the converter should be set to an inductive behaviour while observing the waveform.

5.2.6 Maximum phase shift for different loads

As seen in section 4.2.6, the amount of phase shift that could be achieved was highly dependent on the amount of load on the DC-side. A greater load resulted in higher transients at the zero crossings, which consequently meant that a smaller phase shift was possible. A smaller load conversely entailed lower transients and enabled a greater phase shift. This suggest that overdimensioning the converter, in an real world application, could result in a greater phase shift, as it allows for the tolerance of larger transients.

5.2.7 Line Regulation

Test 4.2.7, showed that that the line regulation ability was depended on the input voltage and load applied. For a half load of 150 W, the converter operated with less stress and was able to regulate and hold a constant output voltage of 390 V. This was the case for all input voltages and phase shifts applied.

For a load of 300 W and at a low input voltage, 85 V, the converter failed to maintain a stable line regulation when a phase shift was introduced. This indicated that the converter's ability to regulate the output voltage was limited at lower voltages and higher loads. Conversely, at higher voltages, the line regulation remained stable even when introducing different phase shifts to the current. This demonstrated that the converter exhibited a greater line regulation within the higher voltage range.

This implies that if the intended use of the converter is within the lower voltages and higher loads, it needs be optimized to ensure stability across the entire range of expected voltages. In a real world application, it may therefore be necessary to establish a lower voltage limit if a phase shift is introduced. This is because fluctuations in DC voltage could potentially damage connected loads. However, in certain practical applications, such as in railway where a ripple of 15 % is allowed, setting a lower voltage limit may not be necessary since some fluctuation in the DC voltage is allowable.

5.2.8 Input voltage

As shown in test 4.2.8, the voltage distortion was approximately 15 % for the different scenarios. When comparing this to the standard IEC 61000-2-2 limiting the total distortion to 8 %, the converter failed the regulation. Because there was no great increase in THD when changing the phase, it could not be said whether the converter needs additional filtering when implementing the adjustable phase. One could argue that the selected EVM does not initially comply with regulations, as its THD exceeds 8 %. However the standard is set for commercial devices, while the EVM kit is only for research purposes. Another aspect to consider is that the

THD might appear larger due to noisy measuring signals. Therefore, measured THD value should be interpreted with caution, as the tests were not conducted precisely according to the testing standard, see section 2.8. While this means these values may not be entirely accurate or comparable to IEC 61000-2-2, the changes in THD still provide an indication of how the results vary across different phase shifts.

5.2.9 Load Regulation

As seen in section 4.2.9, the converter managed to adequately sustain the output voltage at 390 V. Consequently, there is no need to over-dimension the converter in regards to this test. Although it might be relevant to perform some sort of lifetime test of the converter for the different operating conditions.

5.2.10 Output voltage and output current ripple

When comparing the results for the ripple from 4.2.5 and 4.2.10 it can be noticed that the ripple of the output current is affected by the load, as well as by the phase input. When comparing a phase shift of 0° to 60° at full load, the output current ripple increased from 10 % to 15 %. Additionally, the output current ripple decreased from 39 % to 11 %, when comparing a load of 0.077 A to maximum load of 0.77 A. This showed that the output current ripple was significantly more impacted by the load compared to the phase shift. To ensure compliance with regulations it might be needed to filter the current before connecting any load. This is due to that a high ripple current has the potential to damage electrical devices.

It was also seen that the output voltage ripple was affected by the phase input and the load. A greater phase difference resulted in a higher output voltage ripple. When comparing a phase shift of 0° to 60° at full load, the output voltage ripple increased from 5 % to 6.8 %. Additionally, with an increased load the output voltage ripple was increased. The ripple increased from 2.3 % to 6.8 % when comparing a load of 0.077 A to maximum load of 0.77 A. This showed that the output voltage ripple was significantly more impacted by the load compared to the phase shift. Dependent on the intended use, filtering might be needed to meet the specific requirements for different devices as mentioned in 2.8.3. This is because voltage ripple could harm electronic devices that are connected to the DC side.

The ripple will decrease the efficiency of the converter and cause heating in components, due to current passing through parasitic elements, for instance the ESR of capacitors. A large ripple could also generate electromagnetic interference, potentially interfering with nearby electronic devices or communication systems and overstepping the regulatory compliance standards. Components such as capacitors, inductors, and diodes may be exposed to higher stress levels due to the increased current- and voltage ripple. This can lead to premature failure or degradation of these components.

Combining these results indicates that implementing an adjustable power factor

may necessitate additional filtering on the DC side. Depending on the indented use of the converter the bulk capacitors will vary and might need to be increased. However, increasing the capacitors not only enlarges their physical size but also escalates the associated costs. However, it is important to be aware that the converter in use is not designed for commercial applications, resulting in notably high ripple in both current and voltage, even without any modifications.

5.3 Error analysis

In this section, the potential causes of the phase shift deviation between the VINAC pin and the input current will be explained. Additionally, other sources of error will be discussed.

5.3.1 Lack of 1:1 proportionality

As seen in section 3.5.11, it could be seen that the proportionality between the current and the voltage signal in the VINAC pin mainly depended on the input voltage. It was observed that the 1:1 proportionality was valid for input voltages within the range 85-165 V. At higher voltages, including the main operating point of 230 V, the proportionality between the current and voltage phases was non-linear. This leads to the need of a more complex control strategy if a certain power factor is desired. Worth noting is that the proportionality was not affected by the amount of load on the converter.

One potential reason for the lack of proportionality at higher input voltages has to do with the inductor. At lower input voltages the duty cycle of the switches in the converter is high, due to that the converter has to increase a lower input voltage to the desired voltage on the output side, 390 V. In this case, the inductor's current waveform follows the voltage waveform more accurately, resulting in a more 1:1 proportionality between the two. This is due to the controlled current ripple inside the inductor, and the higher voltage ratio between input and output. Conversely, when the input voltage increases the duty cycle decreases. This leads to a higher current ripple and affects the converters ability to follow the reference set by the control loop. The PFC circuit must therefore work harder to achieve the desired phase relationship between current and voltage as the input voltage increases. This is dependent on the control loop's bandwidth and response ability to adjust the current waveform in real time in regards to the voltage waveform. Essentially, this means that the inductor experiences different dynamics dependent on the input voltage, and by manipulating the design of the inductor different characteristics could be achieved.

Another possible explanation for the lack of one-to-one proportionality is when there is a significant phase shift between the current and the measured input voltage. This could lead to the current through the inductor reaching values below zero, resulting in the PFC circuit going out of CCM, see section 2.4.2. The normal control over the current and voltage is therefore no longer maintained and the current does not

follow the voltage in the VINAC pin in a one-to-one relation.

Additionally, the PFC circuitry contains multiple feedback and sensing stages, which need to be considered when adjusting the functionality of the converter. One possible cause for the non-proportionality is the feedback network in the circuit. The network and the compensation components around the error amplifier, may be countering any phase shift introduced at the VINAC pin. This network is robust enough to maintain control stability and correct any phase errors, thus ensuring a high power factor.

Another potential cause is the current sensing stage. As the controller is utilizing an ACMC strategy, the current sense signal is crucial for the operation. The controller adjusts the duty cycle of the switches to minimize the difference between a reference signal, derived from the VINAC pin, and the actual current sense signal. However, if the error is significant, the controller could reach its maximum switching frequency which is limited to 200 kHz. This leads to the input current being unable to follow the intended VINAC signal. An attempt was made to analyze the current sense signals, but due to limited options on measurement tools the signals could not be measured accurately. When trying to use an oscilloscope probe an additional capacitance was introduced in the circuit, which affected the circuit's sensitive feedback loop, leading to incorrect operation of the PFC circuit.

Lastly, the control algorithm within the UCC28070 might have inherent characteristics or limits that prevent significant degradation of the power factor, even when external adjustments are attempted. The controller is fundamentally designed to optimize power factor, and deviating from this might be constrained by the controller's firmware or hardware capabilities.

5.3.2 Measurement inaccuracies

A potential source of insecurity in the results was the lack of synchronization between the signal generator, providing the VINAC signal, and the AC power source, supplying the converter. The generated signal did not synchronize with the 50 Hz signal from the AC power source, causing it to deviate. This required manual adjustment of the signal generator's phase relative to the AC source, which introduced the possibility of human error affecting the intended phase alignment. The same issue appeared when adjusting the VINAC signal for the various phase shifts. In essence, the phase difference could deviate from the initially set value because the signal from the generator was not synchronized. This problem could have been resolved by using a phase-locked loop, utilizing a feedback signal to maintain synchronization between the signal generator and the AC power source.

5.4 Digital case

As seen in section 4.3 the current- and voltage measurement modules successfully measured the current and voltage signals. When the PFC circuit was switched on,

there was a small amount of noise in the measured current signal as seen in Figure 4.45. This in turn caused some inaccuracies when the microcontroller read the signals. The observed phase shift in the measured voltage signal, relative to the actual signal, was attributed to the inherent characteristics of the module. This behavior was influenced by the added capacitors to the circuit, where the schematic can be seen in Figure A.15. Therefore, when integrating the module with the microcontroller, it is crucial to account for the phase shift to ensure accuracy of the calculations.

The DAC output from the microcontroller introduced two challenges in the present configuration. The signal contained noise and was distorted, not accurately representing a purely rectified sinusoidal waveform. This affected how the UCC28070 read the signal, which was addressed by filtering the DAC output digitally in the microcontroller. However, the main issue was setting the output frequency of the DAC to consistently track the frequency of the voltage signal from the power source. This could either be due to the measurement inaccuracies from the voltage- and current modules or due to the code, failing to accurately detect the zero crossings and therefore output the correct frequency. An external synchronization with the AC power source could have resolved this issue but the used source lacked such synchronization. The difficult frequency setting complicated the implementation process, as it prevented the complete system from achieving stable and reliable operation. This meant that a user defined power factor could not be set digitally, as the DAC output floated in relation to the voltage.

5.5 Demand and application for applicable grid services

The concept behind the AC/DC converter with a adjustable power factor offers a solution that could enhance grid efficiency and stability. One application lies within voltage regulation in the grid. Variations in terms of voltage are common challenges in power distribution systems, especially when trying to integrate renewable energy sources such as wind- and solar power. Through enabling users to regulate their power factor, the converter can actively contribute to voltage stabilization and indirectly frequency control. This is true for systems with less mechanical inertia, such as grids with a lot of renewable energy sources. Here, the frequency could be more sensitive to changes in consumption and production. By utilizing the AC/DC converter, the net power factor could be improved which reduces the sensitivity. This contributes to a more stable load profile and indirectly supports frequency stability.

Another benefit for the adjustable power factor is its possibility to suit demand response programs, which would require real time monitoring of the power factor in the grid. Users could then adjust their power factor for their renewable energy systems based on the signals from the TSO. This flexibility contributes to grid stability by making the grid more effective by balancing supply and demand. The demand response programs could be incorporated with customized power supply agreements.

Grid operators could negotiate agreements with decentralized providers to optimize grid performance through specific power factor values. This enhances both the efficiency and cost-effectiveness of the suppliers and consumers. Based on the growth of the technology and the variations in the desired local phase compensation, complex control strategies would likely be needed. This to ensure compliance with present standards in regards to power quality, see section 2.8.3.

5.6 Grid stabilization opportunities with Ericsson's base stations

It was seen from the results presented in 4.5 that Ericsson's base stations unveiled numerous potential opportunities within grid stabilization utilizing power factor adjustment. As outlined in chapter 2.10.3 Ericsson will have the opportunity to synchronize their converters with the TSO, potentially enabling a high-level solution for grid stabilization. This service could however be limited by the present power quality regulations regarding AC/DC converters. These regulations include the maximum amount of allowed harmonic distortion, directly limiting the amount of phase shift possible and therefore restricting the converters applicability. Additionally, when enabling a phase shift the converter experienced increased harmonic content, together with DC side ripple. The last mentioned is especially important in regards to the base stations, where increased ripple deteriorates the performance.

During the microgrid setup test, 5.2.5, the modified AC/DC converter demonstrated the capability to compensate for inductive loads. However, in the test consisting of a lower converter current, grid stabilization was not as effective as desired. This could be experienced in a real world application, where the grid current is larger than the converter current. To manage this in Ericsson's scenario, a combination of multiple converters would be necessary, as a single converter might be insufficient to compensate at high level. The connection of multiple converters would provide a higher total converter current, allowing for a greater phase shift on the grid side.

Lastly, Ericsson also has the opportunity to expand the reach of the AC/DC converter solution to a wider customer base with its own smart grid technology. This would allow for integration with existing infrastructure contributing to a comprehensive solution. Furthermore, the solution could pave the way for new grid stabilization services, increasing the capabilities of the electrical grid.

5.7 Sustainability and ethical parts

The integration of an AC/DC converter with adjustable power factor implies a step toward a future with sustainable and efficient energy management. It optimizes energy transport and decreases transmission losses, saving energy and minimizes waste. The technology enables better integration of renewable energy sources such as solar- and wind power, through adapting to their variable power output. Therefore, re-

ducing greenhouse emissions associated with energy transmission and production.

The solution could contribute to reaching the sustainable development Goal 7 from the United Nations. This goal aims at ensuring an affordable, reliable, sustainable, and modern energy for all [63]. It includes targets that enhance international cooperation facilitating access to clean energy research and technology, such as renewable energy, energy efficiency, and cleaner fossil-fuel technologies. Additionally, this product supports the objectives of Goal 9 by promoting sustainable infrastructure upgrades and industry improvements. These increase resource efficiency, and foster the adoption of clean and environmentally sound technologies [63]. Furthermore, the technology indirectly contributes in achieving Goal 13, which focuses on energy improvements by reducing greenhouse gas emissions, a natural outcome when renewable energy sources are implemented. By contributing to these goals and keeping a social responsibility, the trend towards a sustainable energy system could be set.

6
Conclusion

This thesis concluded that it was feasible to practically modify an AC/DC converter to achieve an adjustable power factor. The prototype solution was tested in a microgrid environment, where a local phase compensation was achieved. The underlying theory regarding attaining a possible phase shift in the converter was validated through a behavioral model in LTspice. This was done by modifying the voltage signal in the control loop. The theory was then applied to the UCC28070 AC/DC converter, where the control circuitry was modified.

A phase shifted current in regards to the voltage was achieved. However, for higher input voltages, $\geq$ 165 V, the current phase did not mirror the phase of the voltage fed into the control circuitry in a 1:1 ratio. At 165 V and at full load, 300 W, a phase shift of about 36.4° in the controller could be achieved before the system encountered significant stress. This translated to a 17.7° phase shift in the current.

When phase shifting the current, a local phase compensation could be achieved. The converter could either be set to exhibit an inductive or capacitive behaviour, depending on the grid characteristics to optimize phase compensation. However, an observation during phase shifting was the development of current transients at the zero crossings of the voltage, intensifying with increased phase shift. This translated into higher peak power demands in the system and challenges in the power electronics. It was also seen that the attainable phase shift was depended on the load on the DC-side, where lower loads allowed for a greater phase shift compared to higher loads. For a half load, 150 W, the maximum amount of current phase shift was 16.9°, while a full load, 300 W, resulted in a maximum current phase shift of 3.1°.

Additionally, the achievable local phase compensation depended on the magnitude of the converter current in relation to the grid current. A high current from the converter resulted in a greater phase compensation, whereas a lower current entailed in a lower phase compensation. With an inductive grid current of 1.59 A RMS and a capacitive converter current (phase shifted by -30°) of 0.977 A RMS, the power factor was increased from 0.93 to 0.95 through adjusting the phase of the current. On the other hand, when having a capacitive converter current of 0.111 A RMS the PF increased from 0.177 to 0.181.

Another consequence of phase shifting was the increased power losses within the circuit and increased harmonic distortion. With an increased phase shift the efficiency of the converter decreased, while the THD increased. At full load, 300 W,

the efficiency decreased from 94.3 % to 72.1 % when applying a phase shift of 60°, simultaneously the THD increased from 26.4 % to 74.6 %. Moreover, when applying a phase shift, the boost inductors and the varistor increased in temperature and contributed to the power losses. A phase shift of 60° resulted in a temperature of 93 °C of the varistor and the inductors reached a temperature of 65 °C. Consequently, phase shifting increased stress on components like inductors and capacitors due to increased temperature and ripple. Therefore, when designing an AC/DC converter with adjustable power factor, it is necessary to account for component stress when phase shifting. It might require the use of components with higher voltage and current ratings, impacting their size, and introducing potential limitations.

Conclusively, by enabling local phase compensation through the converter, the grid efficiency and stability could be enhanced. This is crucial for voltage regulation, especially with the increased integration of renewable energy sources. The converter solution with adjustable power factor could promote and enhance grid stability. Multiple converters could be implemented into Ericsson's base stations and be utilized as a local grid stabilization service.

7
Future work

In this section, future work is suggested, aimed at validating the results and conclusions. By identifying the key areas for improvement, the goal is to commercialize the applicability of a future product. Another possible solution regarding phase compensation is also going to be presented.

- The primary improvement regarding this project is to transition the prototype into an Printed Circuit Board, PCB. This would enhance the signal integrity, leading to more accurate measurements. This would especially benefit the digital solution involving the Arduino UNO R4, allowing for more accurate calculations. The built voltage and current sensors would also likely become usable without the excessive noise when the PFC is turned on. Additionally, a PCB design would ease the performance assessment through simplifying testing procedures and eliminating the need for numerous cables. It would also be a crucial step towards developing a commercial solution, through enabling real-life testing of the product.

- The design of the microgrid in this project consisted of numerous fluorescent lights, symbolizing an inductive grid. While giving an insight into the functionality of the converter, it does not fully capture the complexity of real world systems. To attain a more accurate real world representation, alternative microgrid configurations need be used. These could involve using variable inductive or capacitive loads to asses the converters performance. In addition to the microgrid, it would be interesting to analyze the amount of converters needed for different power levels to achieve a sufficient amount of phase shift.

- Tests that needed further attention are the EMI measurements, which were conducted using the FFT function of the oscilloscope. To achieve credible results and ascertain regulatory compliance, presented in 2.8.3, there are numerous prerequisites for performing the tests. For instance, a LISN together with an environment suitable for EMI measurements is needed [31]. Due to that the requirements for the tests could not be fulfilled, the values obtained cannot directly be compared to the standards.

- It would also be interesting to study the concept of a modified input voltage signal in another converter that utilizes a similar control strategy, ACMC. Then a comparison could have been done regarding the performance and achievable current phase shift of the different converters. This would help in choosing,

and or building, an optimal converter, with adjustable phase shift.

- A financial viability assessment within a commercial context could also be done. It entails making an market analysis and evaluating the economic feasibility for the investment. This could be done by comparing the installation cost with the revenue from the product being sold and the grid stabilization service.

- The expansion from a single phase prototype to a three phase solution could also be done, increasing scale and complexity. This would in turn open up a broader commercial application for the product. The product would require a completely new design and analysis regarding control strategy, harmonics, efficiency and so on, addressing the demands of large scale electrical systems.

- Finally, another possible phase compensation solution, could involve developing a bidirectional solution together with the existing batteries at the base stations. This would, in addition to the adjustable power factor, enable the converter to supply the grid with reactive power, increasing the flexibility.

Bibliography

[1] Jennifer Freeman et al. *The Economic Potential of Offshore Wind in the United States*. Tech. rep. NREL/TP-5000-78472. National Renewable Energy Laboratory (NREL), 2020. URL: https://www.nrel.gov/docs/fy21osti/78472.pdf.

[2] Ciprian Coman, Adriana Florescu, and Constantin-Daniel Oancea. "Improving the Efficiency and Sustainability of Power Systems Using Distributed Power Factor Correction Methods". In: *Sustainability* 12 (Apr. 2020), p. 3134. DOI: 10.3390/su12083134.

[3] WAI-KAI CHEN, ed. *Index*. Burlington: Academic Press, 2003, pp. 1171–1208. ISBN: 978-0-12-170960-0. DOI: https://doi.org/10.1016/B978-012170960-0/50092-X. URL: https://www.sciencedirect.com/science/article/pii/B978012170960050092X.

[4] Ned Mohan, Tore M. Undeland, and William P. Robbins. *Power Electronics. Converters, Applications and Design*. third. John Wiley and Sons, Inc, 2003.

[5] Steve Winder, ed. Second Edition. Newnes, 2017. ISBN: 978-0-08-100925-3. DOI: https://doi.org/10.1016/B978-0-08-100925-3.00019-7. URL: https://www.sciencedirect.com/science/article/pii/B9780081009253000197.

[6] Rudy Severns. *Snubber Circuits For Power Electronics*. Accessed: March 4, 2024. n.d. P. 5. URL: https://rudys.typepad.com/files/snubber-e-book-complete.pdf.

[7] Monolithic Power Systems. *Boost Converters*. Accessed: February 24, 2024. Accessed 2024. URL: https://www.monolithicpower.com/power-electronics/dc-dc-converters/boost-converters.

[8] Harish Sudhakaran Nair and N Lakshminarasamma. "Implementation Aspects of a Single Phase Boost PFC Converter". In: *IECON 2018 - 44th Annual Conference of the IEEE Industrial Electronics Society*. 2018, pp. 1261–1266. DOI: 10.1109/IECON.2018.8591662.

[9] Sunpower. *What is Universal Input?* Accessed: May 5, 2024.

[10] Kali Naraharisetti, Janamejaya Channegowda, and Peter B. Green. "Design and modeling of CCM average current control PFC AC-DC Boost converter". In: *2021 IEEE Green Technologies Conference (GreenTech)*. 2021, pp. 403–408. DOI: 10.1109/GreenTech48523.2021.00069.

[11] Monolithic Power Systems. *Power Factor Correction Technologies*. https://www.monolithicpower.com/en/power-factor-correction. Accessed: April 9, 2024. 2024.

[12] Emmanuel Hernández Mayoral et al. *Fourier Analysis for Harmonic Signals in Electrical Power Systems*. Ed. by Goran S. Nikolic, Milorad D. Cakic, and

Dragan J. Cvetkovic. Rijeka: IntechOpen, 2017. Chap. 3. DOI: 10.5772/66733. URL: https://doi.org/10.5772/66733.

[13] Pratap Ranjan Mohanty, Anup Kumar Panda, and Dhiman Das. "An active PFC boost converter topology for power factor correction". In: *2015 Annual IEEE India Conference (INDICON)*. 2015, pp. 1–5. DOI: 10.1109/INDICON.2015.7443118.

[14] Kali Naraharisetti, Janamejaya Channegowda, and Peter B. Green. "Design and modeling of CCM average current control PFC AC-DC Boost converter". In: *2021 IEEE Green Technologies Conference (GreenTech)*. 2021, pp. 403–408. DOI: 10.1109/GreenTech48523.2021.00069.

[15] Klaus Raggl et al. "Comprehensive Design and Optimization of a High-Power-Density Single-Phase Boost PFC". In: *IEEE Transactions on Industrial Electronics* 56.7 (2009), pp. 2574–2587. DOI: 10.1109/TIE.2009.2020074.

[16] Texas Instruments. *Basic Calculation of a Buck Converter's Power Stage*. Accessed: May-20-2024. 2015. URL: https://www.ti.com/lit/an/slva477b/slva477b.pdf.

[17] Hengshan Xu et al. "Optimal Design Method of Interleaved Boost PFC for Improving Efficiency from Switching Frequency, Boost Inductor, and Output Voltage". In: *IEEE Transactions on Power Electronics* 34.7 (2019), pp. 6088–6107. DOI: 10.1109/TPEL.2018.2872427.

[18] D.J.S. Newlin, R. Ramalakshmi, and S. Rajasekaran. "A performance comparison of interleaved boost converter and conventional boost converter for renewable energy application". In: Mar. 2013, pp. 1–6. ISBN: 978-1-4673-2592-9. DOI: 10.1109/ICGHPC.2013.6533924.

[19] Sandeep Kolluri and N. Lakshmi Narasamma. "Analysis, modeling, design and implementation of average current mode control for interleaved boost converter". In: *2013 IEEE 10th International Conference on Power Electronics and Drive Systems (PEDS)*. 2013, pp. 280–285. DOI: 10.1109/PEDS.2013.6527029.

[20] Michael O'Loughlin, Texas Instruments. *An Interleaved PFC Preregulator for High-Power Converters*. https://www.ti.com/lit/wp/slua746/slua746.pdf. Accessed: May 21, 2024. 2015.

[21] Abhishek Kar and Mainak Sengupta. "Design, analysis, fabrication and testing of a 3kW power factor correction boost rectifier". In: *2016 IEEE International Conference on Power Electronics, Drives and Energy Systems (PEDES)*. 2016, pp. 1–6. DOI: 10.1109/PEDES.2016.7914361.

[22] William Bolton. "Chapter 13 - Control Systems". In: *Instrumentation and Control Systems (Third Edition)*. Ed. by William Bolton. Third Edition. Newnes, 2021, pp. 297–328. ISBN: 978-0-12-823471-6. DOI: https://doi.org/10.1016/B978-0-12-823471-6.00013-7. URL: https://www.sciencedirect.com/science/article/pii/B9780128234716000137.

[23] Texas Instruments. *Average Current Mode Controlled Power Factor Correction Converter using TMS320LF2407A*. Application Report SPRA902A. Accessed: April 9 2024. Texas Instruments, 2002. URL: https://www.ti.com/lit/an/spra902a/spra902a.pdf.

[24] Petr Frgal. *Avergae Current Mode Interleaved PFC Control*. Tech. rep. Accessed: March 30, 2024. NXP Semiconductors, 2016.

[25] ON Semiconductor. *Power Factor Correction (PFC) Handbook, Choosing the Right Power Factor Controller Solution*. Tech. rep. Accessed: March 30, 2024. ON Semiconductor, 2014.

[26] A. V. Oppenheim and A. S. Willsky. *Signals and Systems*. 2nd ed. Prentice Hall, 2013. ISBN: 0-13-651175-9.

[27] Texas Instruments. *UCC28070 Interleaving Continuous Conduction Mode PFC Controller*. Accessed: March 4, 2024. 2016.

[28] MIchael O'Loughlin. *UCC28070 300-W Interleaved PFC Pre-Regulator Design Review*. Tech. rep. Accessed: March 4, 2024. Texas Instruments, 2010.

[29] Andrzej M. Trzynadlowski. "Chapter 40 - EMI Effects of Power Converters". In: *Power Electronics Handbook (Fifth Edition)*. Ed. by Muhammad H. Rashid. Fifth Edition. Butterworth-Heinemann, 2024, pp. 1343–1358. ISBN: 978-0-323-99216-9. DOI: https://doi.org/10.1016/B978-0-323-99216-9.00017-2. URL: https://www.sciencedirect.com/science/article/pii/B9780323992169000172.

[30] Würth Elektronik Dheeraj Jain. *Understanding EMC and EMI Basics with Würth Elektronik*. https://www.allaboutcircuits.com/industry-white-papers/understanding-emc-emi-basics-wurth-elektronik/. Accessed: May 4, 2024. 2022.

[31] Academy of EMC. *EMC Standards*. https://www.academyofemc.com/emc-standards. Accessed: May 4, 2024. 2024.

[32] Comsys. *Power Quality - IEEE 519-2022*. https://comsys.se/our-adf-technology/power-quality-ieee-519-2022/. Accessed: May 4, 2024. 2024.

[33] Comsys. *Power Quality - IEC 61000*. https://comsys.se/our-adf-technology/power-quality-iec-61000/. Accessed: May 4, 2024. 2024.

[34] SEK Svensk Elstandard. *SS-EN 50155 Railway applications - Rolling stock - Electronic equipment*. https://elstandard.se/standard/1899601. Accessed: May 12, 2024. 2017.

[35] *IACS Requirements concerning electrical and electronic installations*. https://safety4sea.com/wp-content/uploads/2023/10/IACS-Requirements-concerning-electrical-and-electronic-installations-2023_09.pdf. [Accessed: May 12, 2024]. 2023.

[36] *USB 2.0 Specification*. https://usb.org/document-library/usb-20-specification. [Accessed: May 12, 2024]. 2000.

[37] UL. *IEC 62368-1 Testing and Certification*. https://www.ul.com/services/iec-62368-1-testing-certification. Accessed: May 4, 2024. 2024.

[38] Ben Lutkevich. *Microcontroller (MCU)*. https://www.techtarget.com/iotagenda/definition/microcontroller. Accessed: March 17, 2024. 2019.

[39] WeMos. *WeMos D32 Documentation*. https://www.wemos.cc/en/latest/d32/d32.html. Accessed: April 4, 2024. 2021.

[40] Arduino. *Arduino Uno R4 WiFi*. https://store.arduino.cc/products/uno-r4-wifi. Accessed: April 30, 2024. 2024.

[41] Darko Hercog et al. "Design and Implementation of ESP32-Based IoT Devices". In: *Sensors* 23 (July 2023), p. 6739. DOI: 10.3390/s23156739.

[42] Espressif Systems. *ESP32-WROOM-32E & ESP32-WROOM-32UE Datasheet*. https://www.espressif.com/sites/default/files/documentation/esp32-wroom-32e_esp32-wroom-32ue_datasheet_en.pdf. Accessed: April 10, 2024. 2024.

[43] uPesy. *How to connect to a WiFi network with the ESP32*. https://www.upesy.com/blogs/tutorials/how-to-connect-wifi-acces-point-with-esp32. Accessed: April 15, 2024. 2023.

[44] Espressif. *ESP-Modbus*. https://docs.espressif.com/projects/esp-idf/en/v4.4.3/esp32/api-reference/protocols/modbus.html. Accessed: April 15, 2024. 2022.

[45] Emmanuel Hernández-Mayoral et al. "A Comprehensive Review on Power-Quality Issues, Optimization Techniques, and Control Strategies of Microgrid Based on Renewable Energy Sources". In: *Sustainability* 15.12 (2023). ISSN: 2071-1050. DOI: 10.3390/su15129847. URL: https://www.mdpi.com/2071-1050/15/12/9847.

[46] Jindi Hu et al. "Assessment for Voltage Violations considering Reactive Power Compensation Provided by Smart Inverters in Distribution Network". In: *Frontiers in Energy Research* 9 (July 2021), p. 713510. DOI: 10.3389/fenrg.2021.713510.

[47] Svenska Kraftnät. *Karta över transmissionsnätet*. https://www.svk.se/om-kraftsystemet/om-transmissionsnatet/transmissionsnatskarta/. Accessed: March 17, 2024. 2023.

[48] Strålsäkerhetsmyndigheten. *Kärnkraft*. https://www.stralsakerhetsmyndigheten.se/omraden/karnkraft/. Accessed: March 19, 2024. 2024.

[49] Svenska Kraftnät. *Sveriges Elnät*. https://www.svk.se/om-kraftsystemet/oversikt-av-kraftsystemet/sveriges-elnat/. Accessed: March 19, 2024. 2024.

[50] Lackis Eleftheriadis et al. *Balance Smart Grids with 5G Backup for Utilities*. https://www.ericsson.com/en/reports-and-papers/white-papers/balance-smart-grids-with-5g-backup-for-utilities. Accessed: March 19, 2024. 2024.

[51] M. H. Albadi and E. F. El-Saadany. "Demand Response in Electricity Markets: An Overview". In: *2007 IEEE Power Engineering Society General Meeting*. 2007, pp. 1–5. DOI: 10.1109/PES.2007.385728.

[52] Gavin Wright. *Base Station*. https://www.techtarget.com/whatis/definition/base-station. Accessed: March 18, 2024.

[53] Svenska Kraftnät. *Frekvensstabilitet*. https://www.svk.se/om-kraftsystemet/om-systemansvaret/kraftsystemstabilitet/frekvensstabilitet/. Accessed: March 21, 2024. 2024.

[54] Dallas Semiconductor. *Digitally-Controlled Phase Shift Using the DS1669*. https://www.analog.com/media/en/technical-documentation/app-notes/digitallycontrolled-phase-shift-using-the-ds1669.pdf. Accessed: April 8, 2024.

[55] Electronics Tutorials. *RC Oscillator Circuit*. [Accessed: May 12, 2024]. 2021. URL: https://www.electronics-tutorials.ws/oscillator/rc_oscillator.html.

[56] Cadence. *RC Phase Shift Oscillator Design for Sine Wave Generation*. https://resources.system-analysis.cadence.com/blog/msa2020-rc-phase-shift-oscillator-design-for-sine-wave-generation. [Accessed: May 12, 2024]. 2020.

[57] Electronics Tutorial. *Inverting Operational Amplifier*. https://www.electronics-tutorials.ws/opamp/opamp_2.html. [Accessed: May 12, 2024].

[58] Toshiba Semiconductor. *What is the Input Offset Voltage of an Op-Amp*. https://toshiba.semicon-storage.com/ap-en/semiconductor/knowledge/faq/linear_opamp/what-is-the-input-offset-voltage-of-an-op-amp.html. [Accessed: May 12, 2024]. 2024.

[59] Allegro Microsystems. *ACS70331EESATR-2P5U3 Datasheet*. Accessed: May 6, 2024.

[60] Solarduino. *AC Power Measurement with Arduino*. https://solarduino.com/wp-content/uploads/2019/12/2019-12-31_AC_Power.ino. Accessed: May 19, 2024. Dec. 2019.

[61] ELFA. *SOM5-250-R-L2 Varistor*. https://www.elfa.se/sv/isomsv-varistor-250vac-320vdc-bourns-isom5-250-l2/p/30229576. Accessed: May 21, 2024. 2024.

[62] DigiKey. *Eaton Electronics Division CTX16-18405-R*. https://www.digikey.se/en/products/detail/eaton-electronics-division/CTX16-18405-R/1839857. Accessed: May 21, 2024. 2024.

[63] United Nations. *Take Action for the Sustainable Development Goals*. https://www.un.org/sustainabledevelopment/sustainable-development-goals/. [Accessed: May 12, 2024].

A

Appendix I

A.1 Evaluation Module, EVM, of the converter

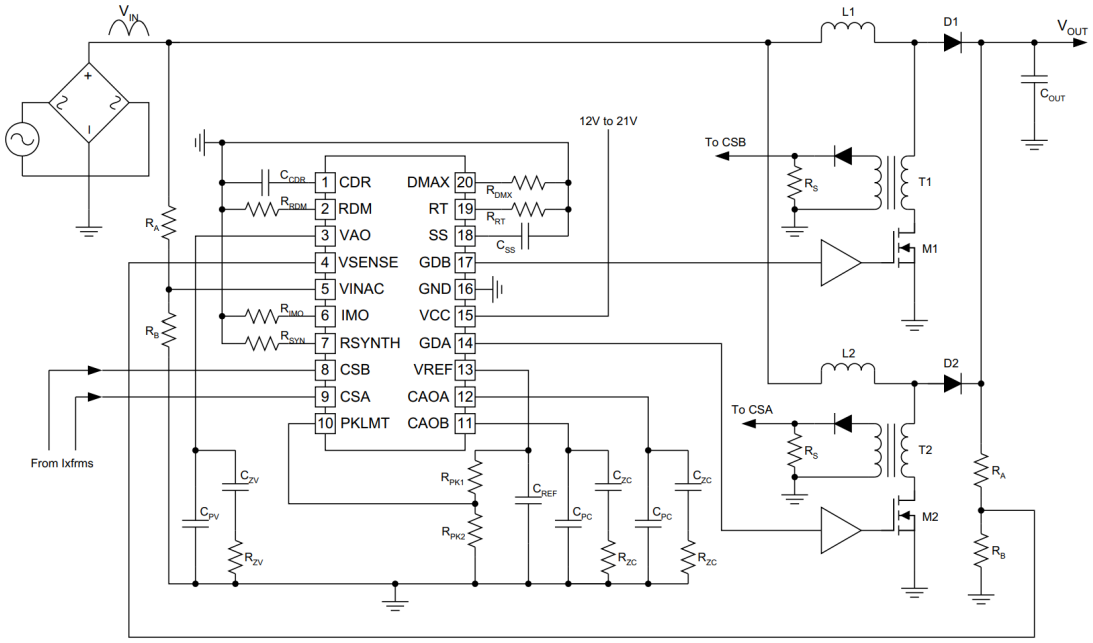

Figure A.1: Typical application for the UCC28070 [28]. Reprinted with permission.

A.1.1 Motherboard of UCC28070 EVM

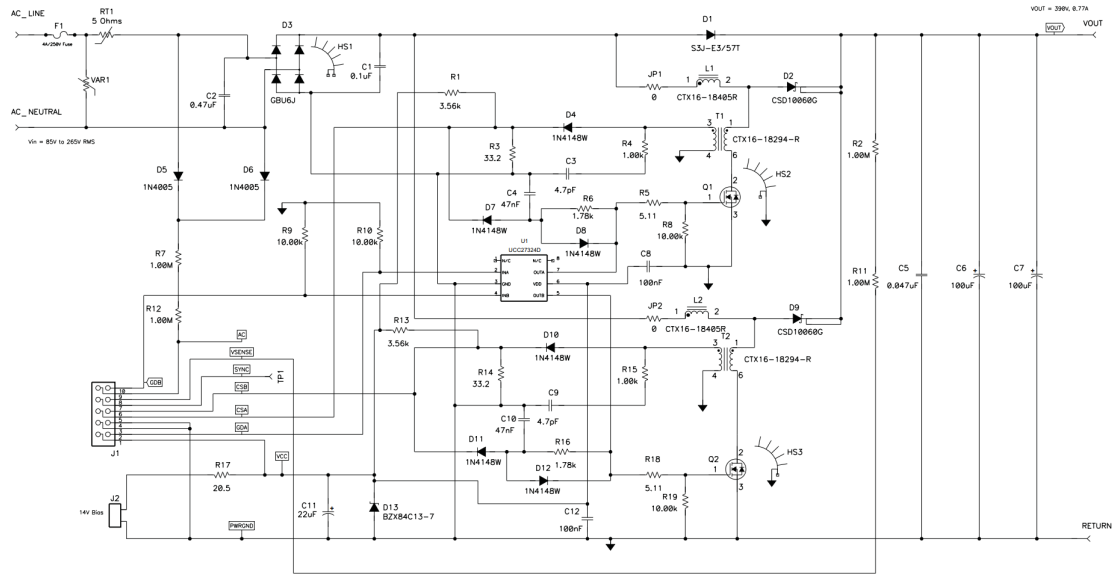

Figure A.2: Schematic for the motherboard of UCC28070EVM [28]. Reprinted with permission.

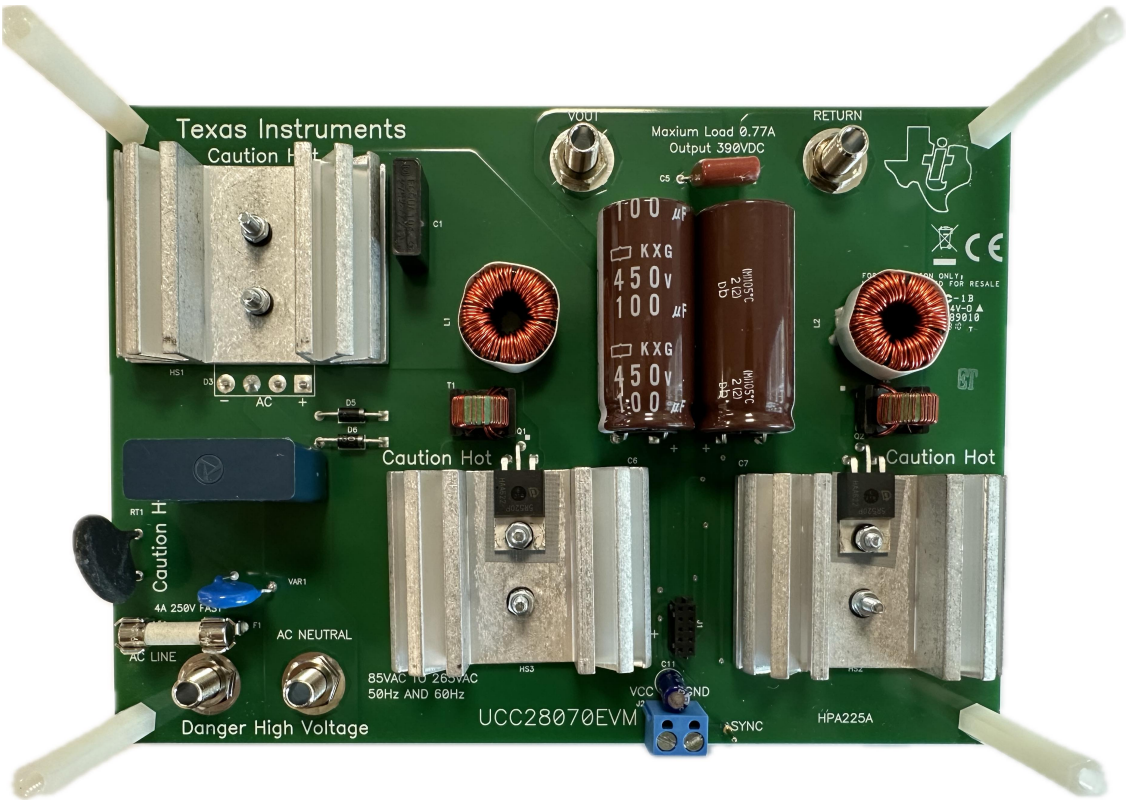

Figure A.3: Motherboard of UCC28070EVM.

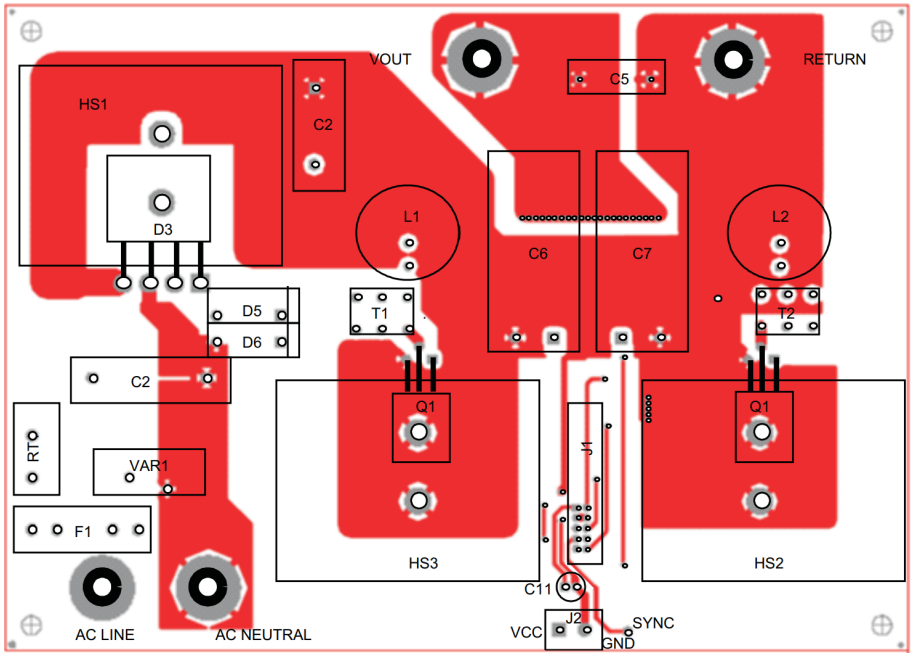

Figure A.4: Motherboard of UCC28070EVM top assembly [28]. Reprinted with permission.

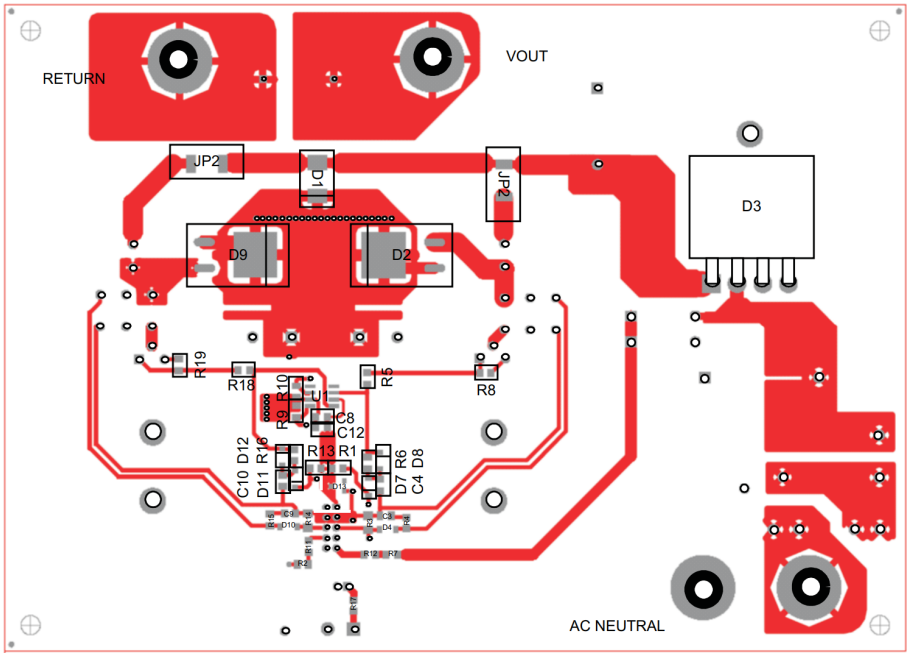

Figure A.5: Motherboard of UCC28070EVM bottom assembly [28]. Reprinted with permission.

A.1.2 Daughterboard of UCC28070EVM

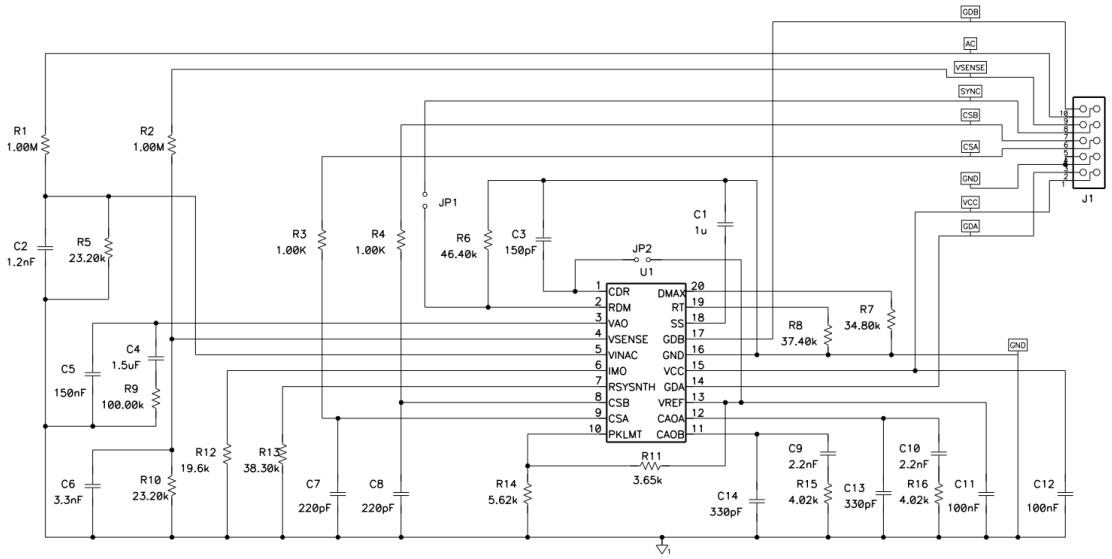

Figure A.6: Schematic for the daughterboard of UCC28070EVM [28]. Reprinted with permission.

Figure A.7: Daughterboard of UCC28070EVM.

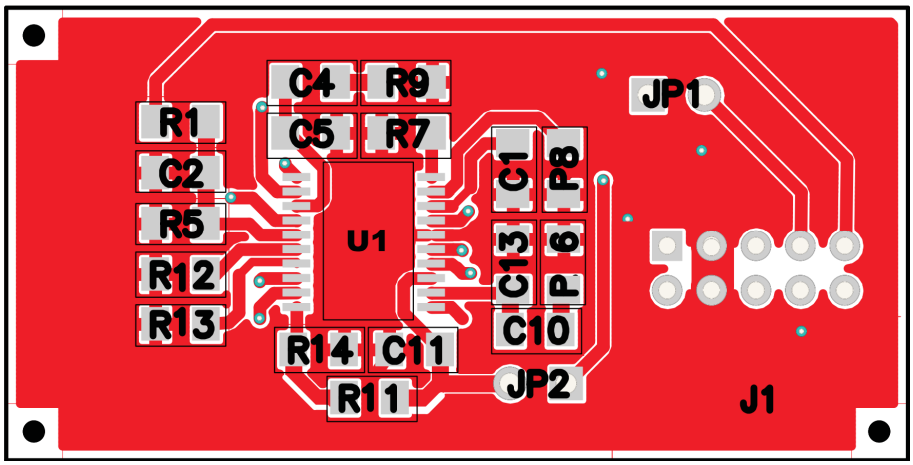

Figure A.8: Daughterboard of UCC28070 top assembly [28]. Reprinted with permission.

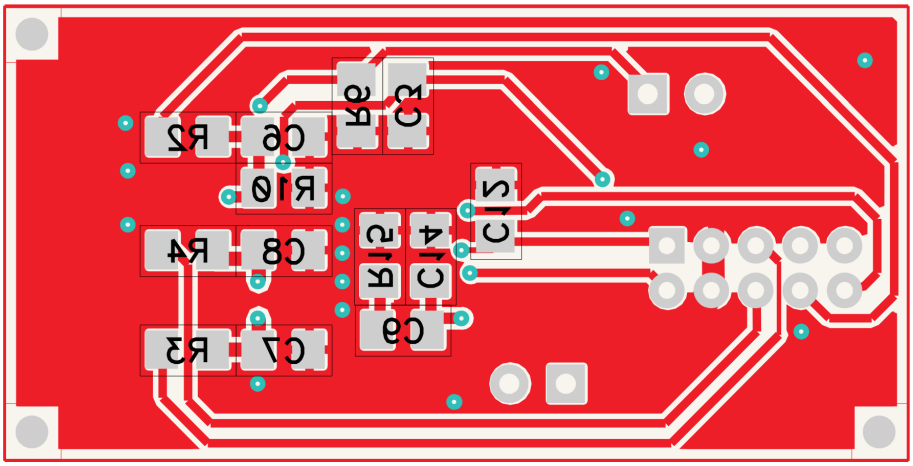

Figure A.9: Daughterboard of UCC28070 bottom assembly [28]. Reprinted with permission.

A.1.3 Functional block diagram

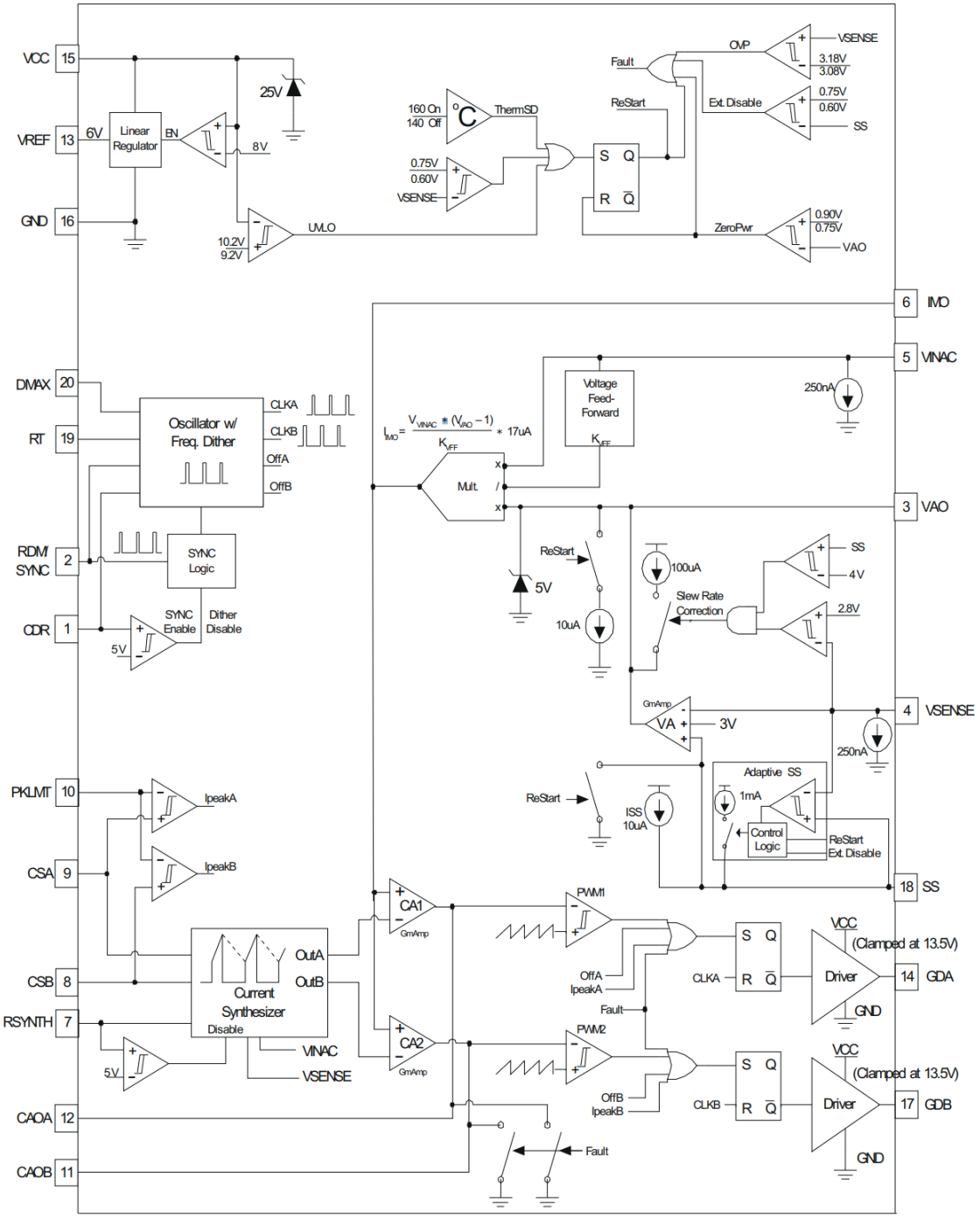

Figure A.10: Functional block diagram over the UCC28070 [28]. Reprinted with permission.

A.2 Built voltage- and current sensors

A.2.1 Current measurement modules

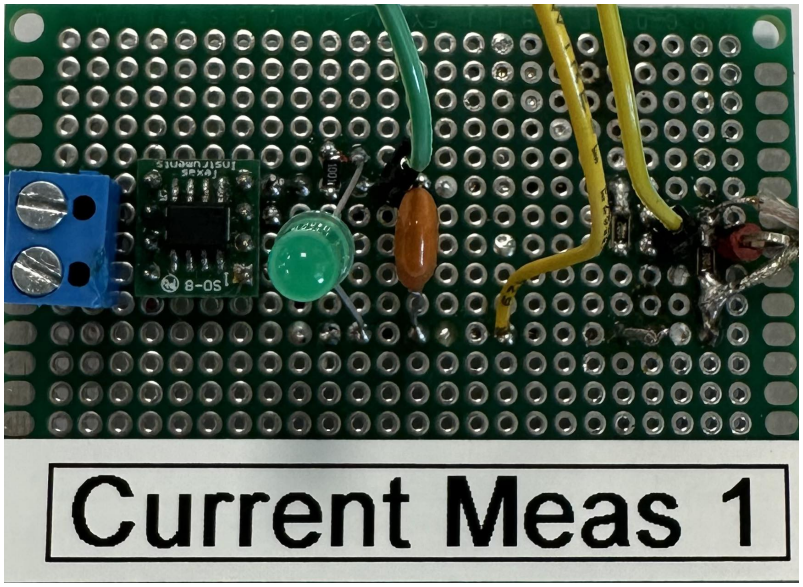

Figure A.11: First version of the built current measurement module.

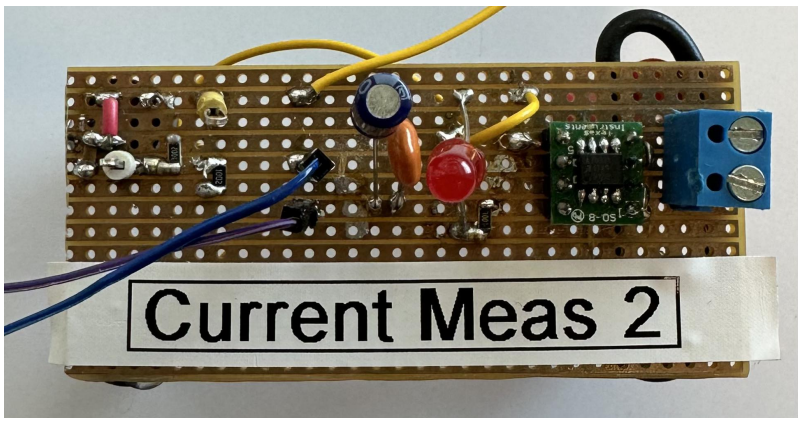

Figure A.12: Second version of the built current measurement module.

A.2.2 Voltage measurement module

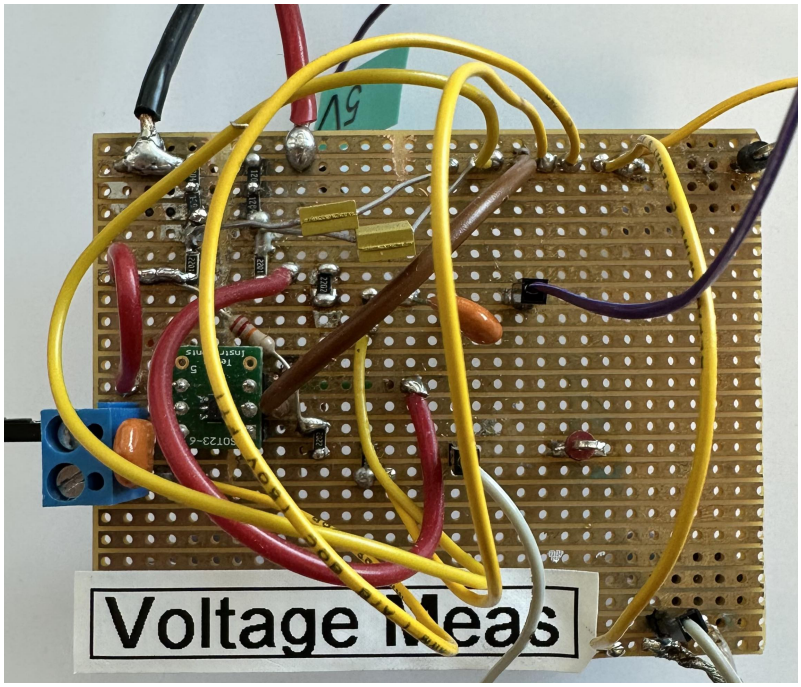

Figure A.13: Built voltage measurement module.

A.3 Bought voltage- and current sensor modules

A.3.1 Voltage measurement module

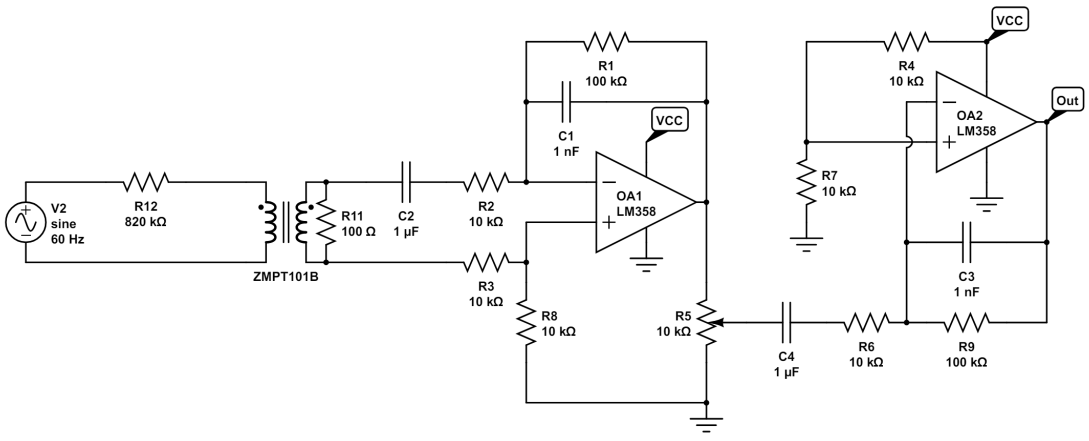

Figure A.14: Schematic over ZMPT101B voltage sensor module.

A.3.2 Current measurement module

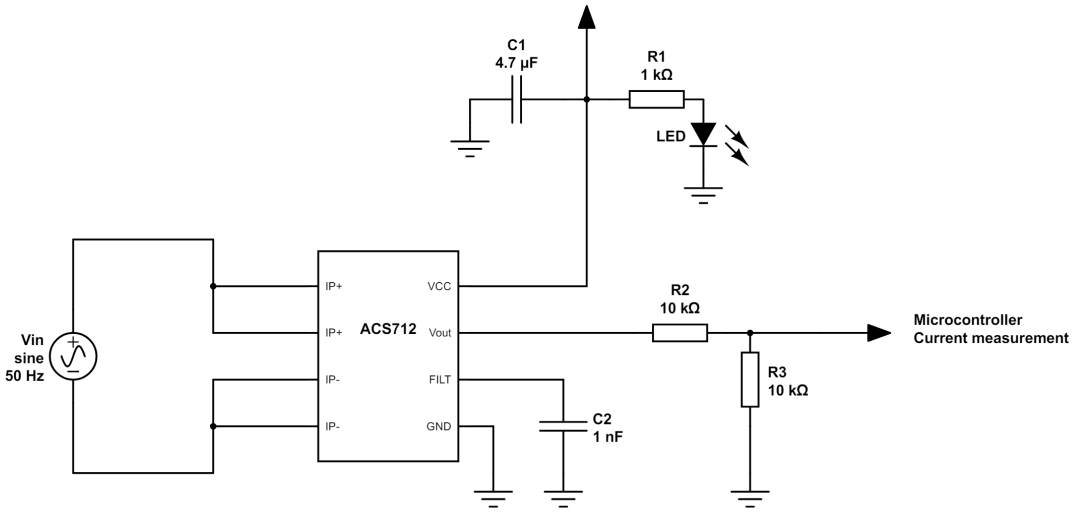

Figure A.15: Schematic over ACS712 current sensor module.

A.4 Analog phase shifting units

A.4.1 RC phase shift oscillator with one op-amp

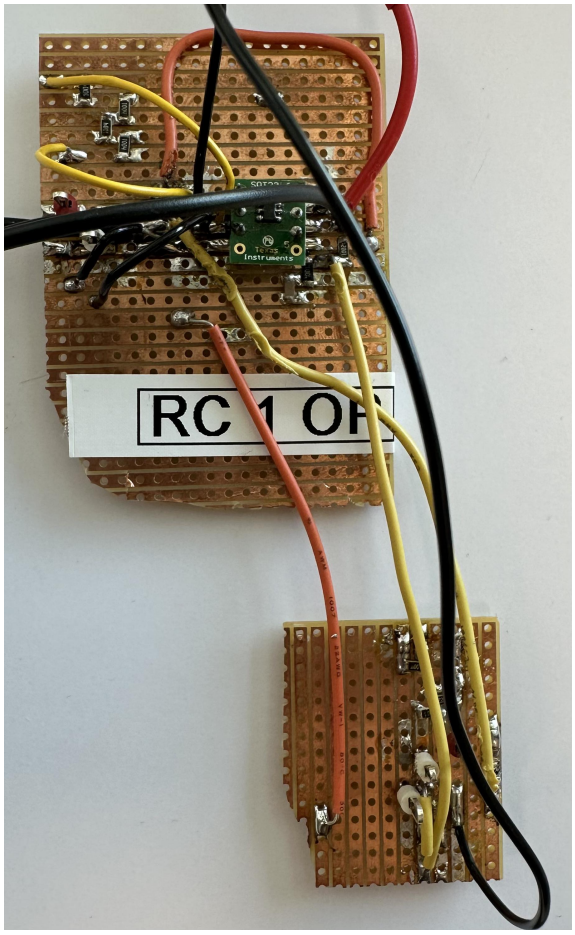

Figure A.16: Built RC phase shift oscillator with one op-amp.

A.4.2 RC phase shift oscillator 3 op-amps

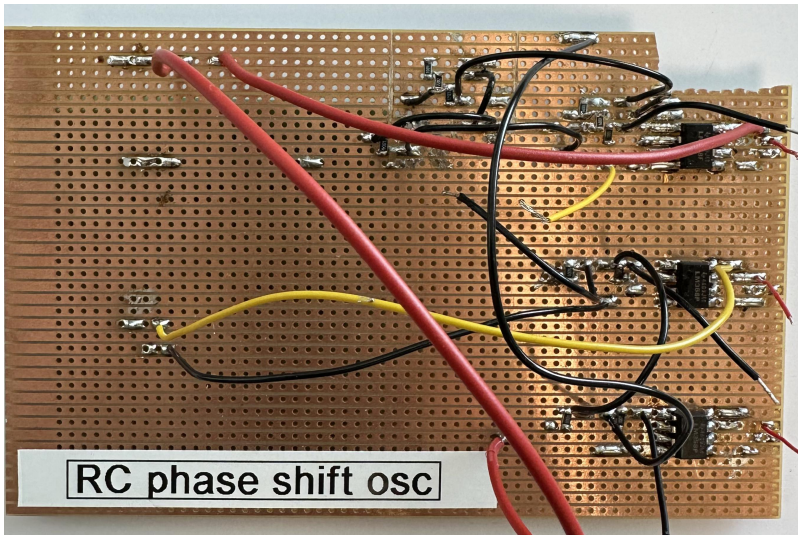

Figure A.17: Built RC phase shift oscillator with three op-amps.

A.5 Diode bridge

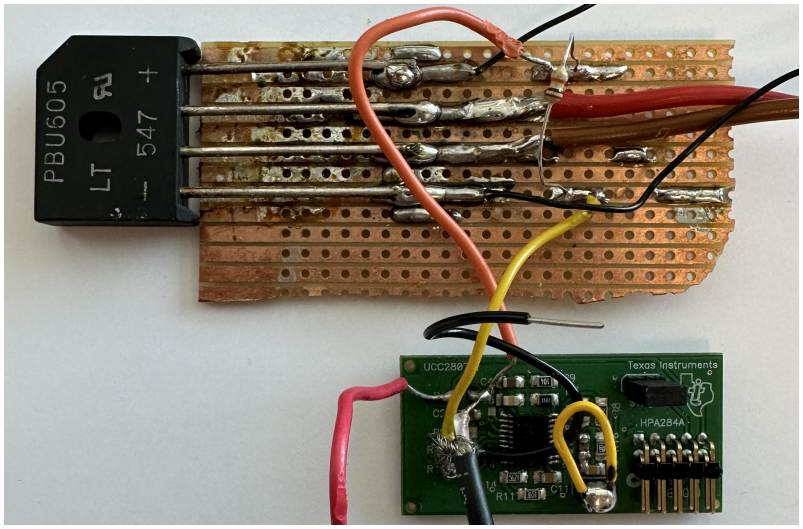

Figure A.18: Built diode bridge rectifier setup with the daughterboard.

B
Appendix II

B.1 Results from simulations

In Figure B.1 the rectified signal had been phase shifted -30°, when the output power of the converter was set to 300 W. The RMS value of the current reached a value 1.44 A and the current spikes at the zero crossings reached approximately ±0.91 A.

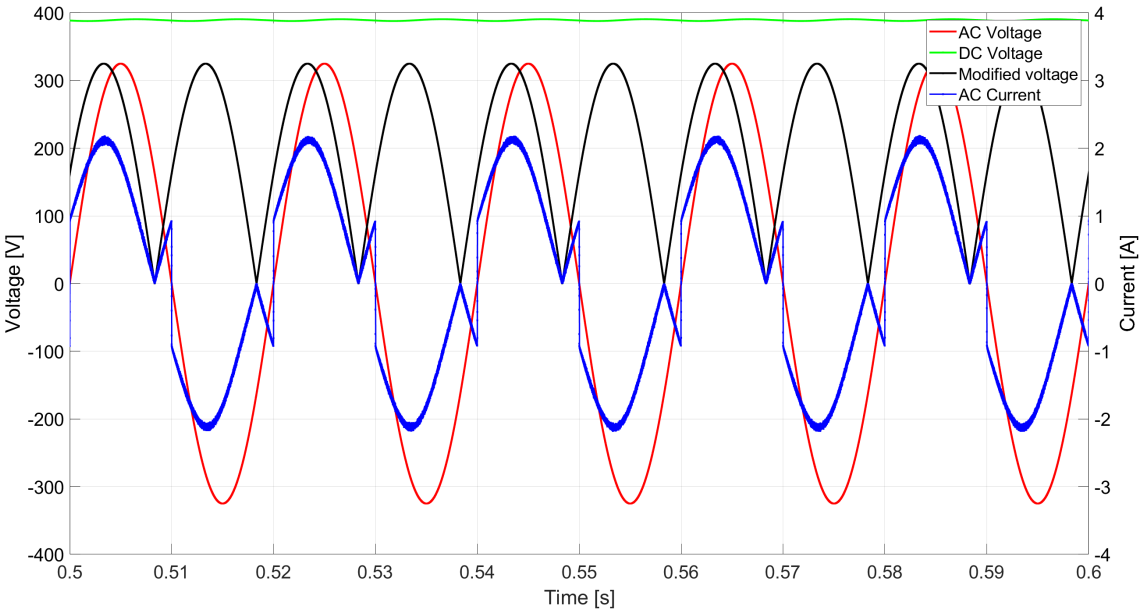

Figure B.1: Simulated input voltage and current, modified voltage and output current, -30° phase shift for an output power of 300 W.

Figure B.2 represents the 20 first harmonic components of the input current at a load of 300 W. The THD of the input current at -30° is 27.84 %.

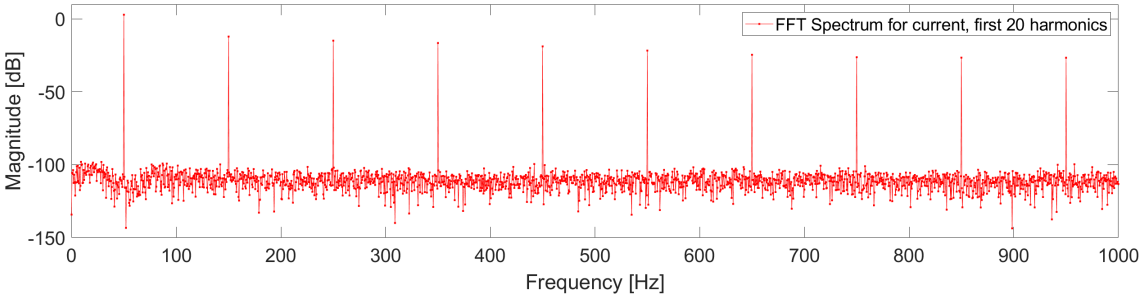

Figure B.2: FFT analysis of the 20 first harmonic components for the input current, -30° phase shift for an output power of 300 W.

In Figure B.3 the rectified signal had been phase shifted -60°, when the output power of the converter was set to 300 W. The RMS value of the current reached a value 1.82 A and the current spikes at the zero crossings reached approximately ±2.09 A.

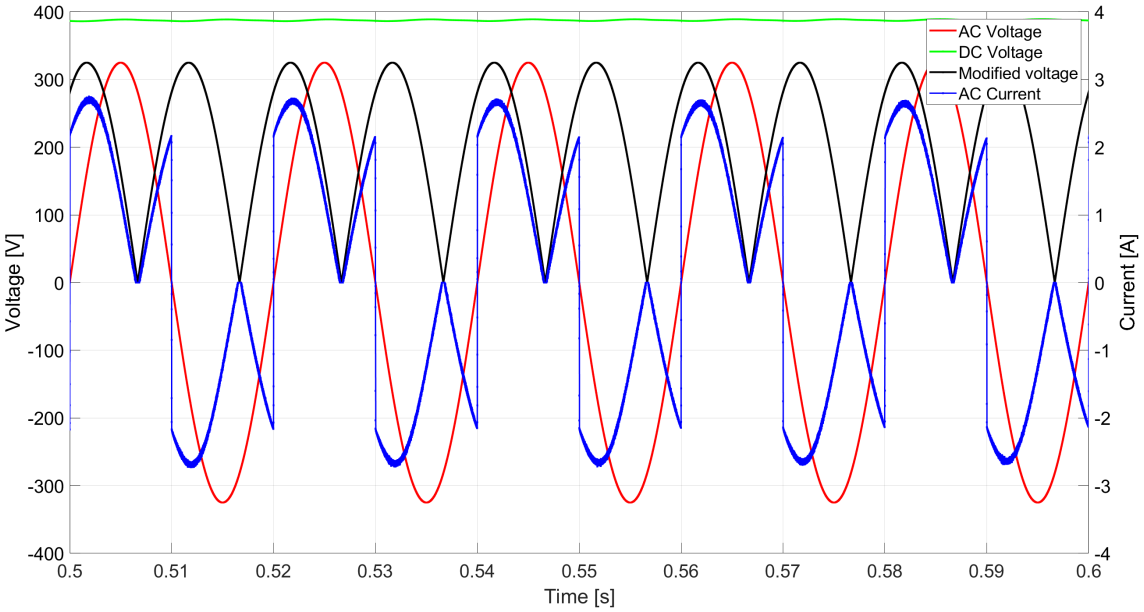

Figure B.3: Simulated input voltage and current, modified voltage and output current, -60° phase shift for an output power of 300 W.

Figure B.4 represents the 20 first harmonic components of the input current at a load of 300 W. The THD of the input current at -60° is 77.43 %.

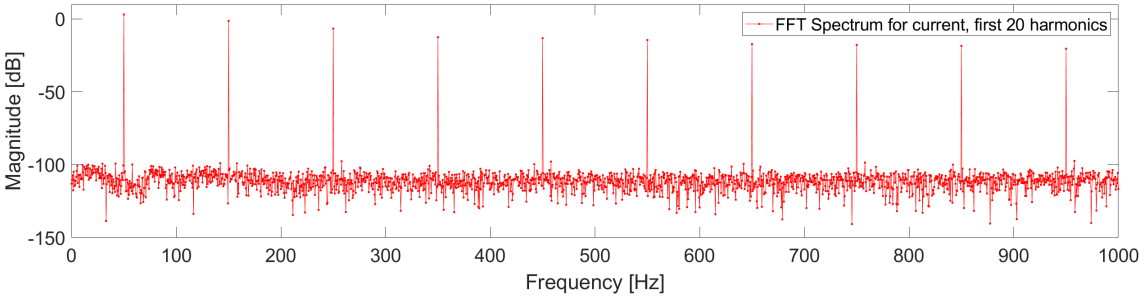

Figure B.4: FFT analysis of the 20 first harmonic components for the input current, -60° phase shift for an output power of 300 W.

B.2 Results from microgrid test

B.2.1 Microgrid, output current 0.05 A

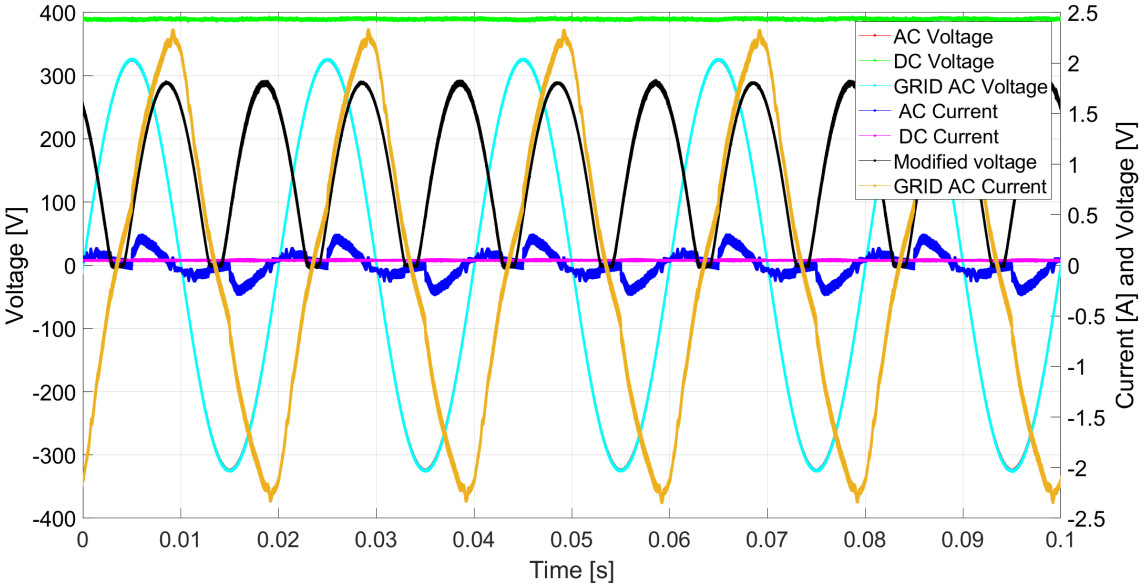

Figure B.5: Measured voltages and currents for the microgrid, I_{out} = 0.05 A and 60° phase shift from the converter.

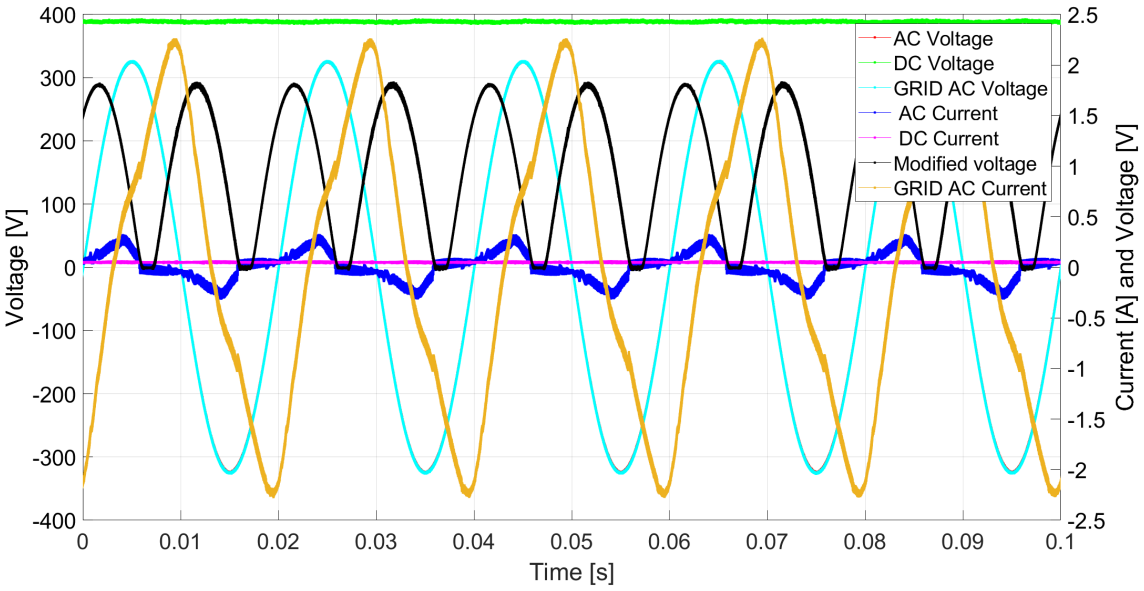

Figure B.6: Measured voltages and currents for the microgrid, I_{out} = 0.05 A and -60° phase shift from the converter.

B.2.2 Microgrid, output current 0.145 A

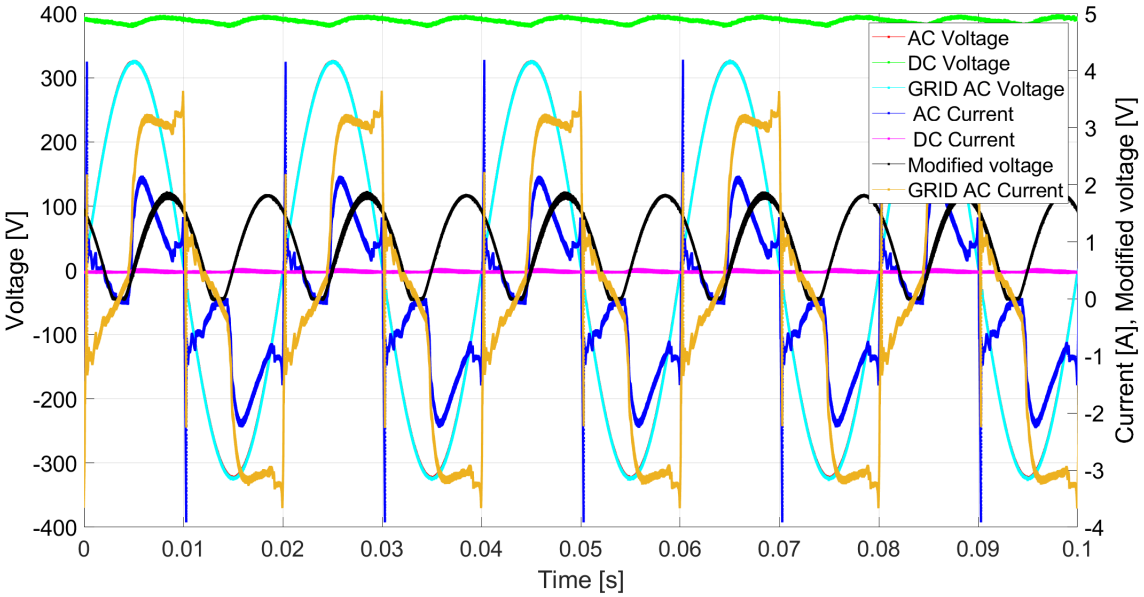

Figure B.7: Measured voltages and currents for the microgrid, I_{out} = 0.145 A and 60° phase shift from the converter.

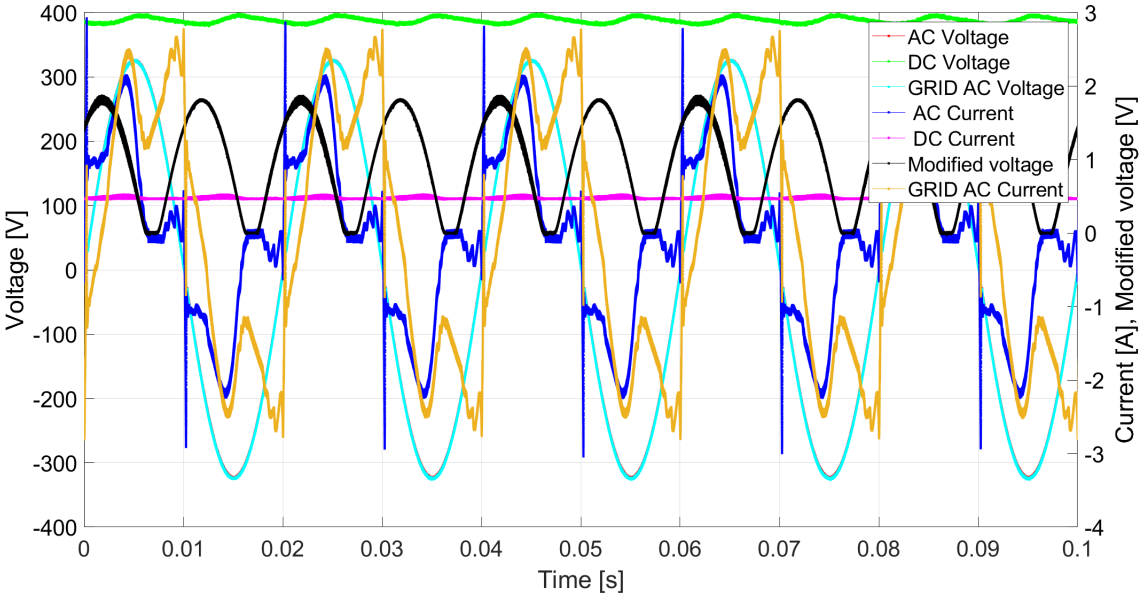

Figure B.8: Measured voltages and currents for the microgrid, I_{out} = 0.145 A and -60° phase shift from the converter.

B.2.3 Microgrid, output current 0.5 A

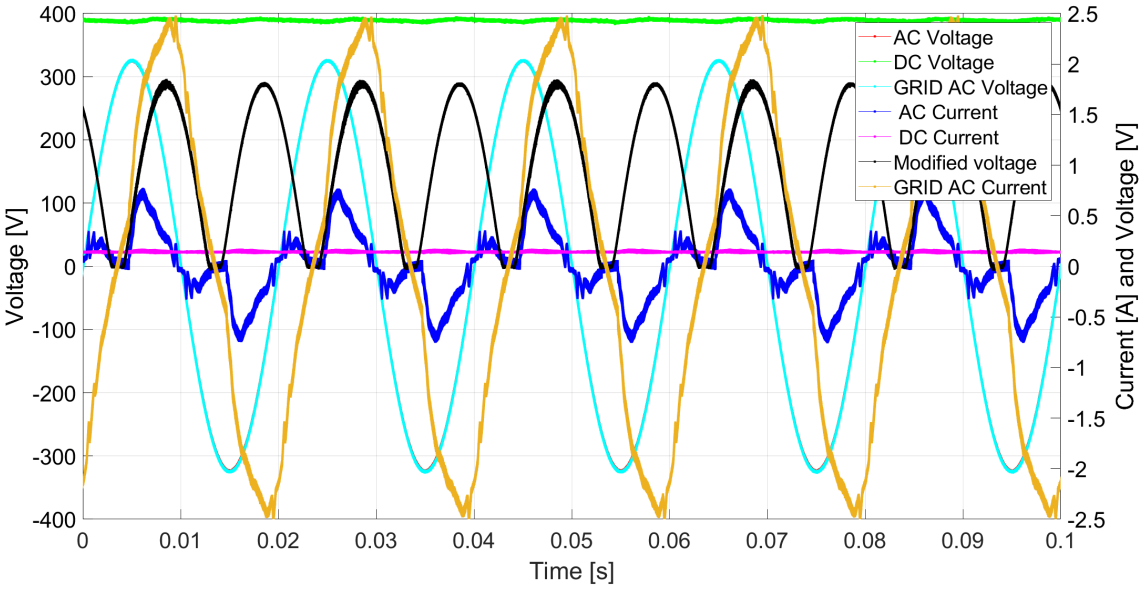

Figure B.9: Measured voltages and currents for the microgrid, I_{out} = 0.5 A and 60° phase shift from the converter.

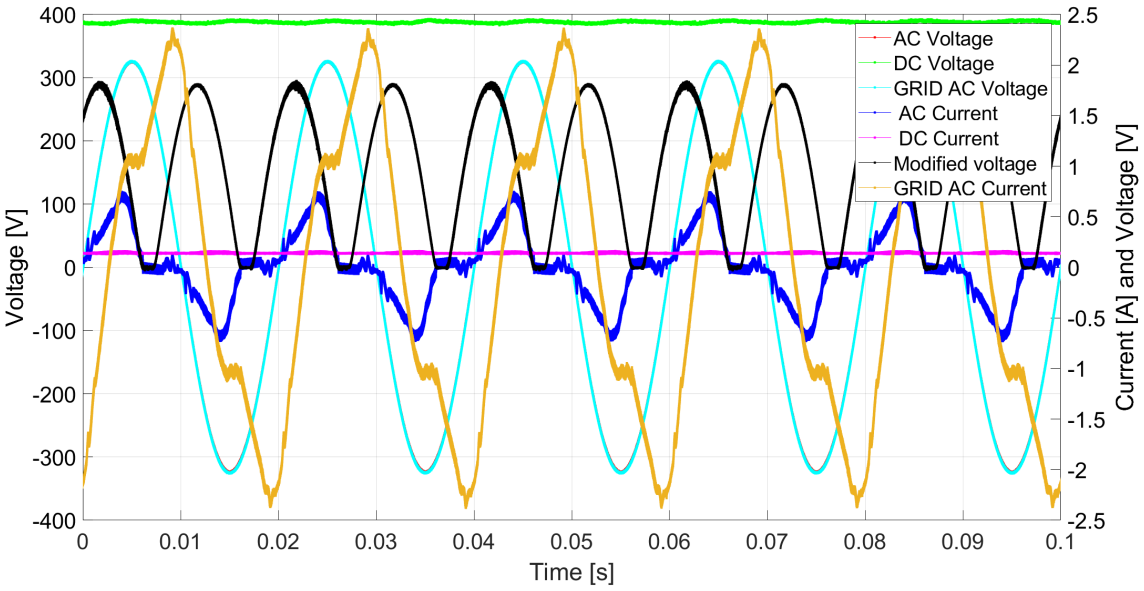

Figure B.10: Measured voltages and currents for the microgrid, $I_{out} = 0.5$ A and -60° phase shift from the converter.

C

Appendix III

C.1 Arduino code

```
/* 0- General */
int decimalPrecision = 2;

/* 1- AC Voltage Measurement */
int voltageOffset1 = 344;
int voltageOffset2 = 8;
int VoltageAnalogInputPin = A2; // Pin for reading AC voltage
float voltageSampleRead = 0; // Variable to store the voltage sample
float voltageLastSample = 0; // Time of the last voltage sample
float voltageSampleSum = 0; // Sum the voltage samples
float voltageSampleCount = 0; // Count number of voltage samples
float RMSVoltageMean; // Voltage RMS
unsigned long lastVoltageZeroCrossingTime = 0; // Time of the last voltage zero
    crossing
float voltageFrequency = 0; // Voltage frequency

/* 2- AC Current Measurement */
int currentOffset1 = -17;
int currentOffset2 = -2;
int CurrentAnalogInputPin = A3; // Pin for reading AC current
float mVperAmpValue = 100; // Conversion factor
float currentSampleRead = 0; // Variable to store the current sample
float currentLastSample = 0; // Time of the last current sample
float currentSampleSum = 0; // Sum of current samples
float currentSampleCount = 0; // Count number of current samples
float currentMean; // Mean value of current
float RMSCurrentMean = 0; // Current RMS
float FinalRMSCurrent; // Current RMS with conversion considered

/* 3- AC Rectified Voltage Measurement */
int rectifiedVoltageOffset = 0;
int RectifiedVoltageDigitalOutputPin = A0; // Pin for DAC output
float rectifiedVoltageSampleRead = 0; // Variable to store the rectified voltage
float rectifiedVoltageLastSample = 0; // Time of the last rectified voltage
float rectifiedVoltageSampleSum = 0; // Sum of rectified voltage
float rectifiedVoltageSampleCount = 0; // Count number of rectified voltage samples
float rectifiedVoltageMean; // Mean value of rectified voltage

/* 4- AC Power Measurement */
int powerOffset = 0;
float sampleCurrent1;
float sampleCurrent2;
float sampleCurrent3;
float apparentPower; // Defining apparent power
float realPower = 0; // Defining real power
float powerSampleRead = 0; // Storing the power sample
float powerLastSample = 0; // Time of the last power sample
float powerSampleCount = 0; // Count number of power samples
float powerSampleSum = 0; // Sum power samples
float powerFactor = 0; // Defining power factor
float desiredPowerFactor = 0.8; // USER DEFINED POWER FACTOR, change this!
```

```
// PI Controller parameters
float kp = 10; // Proportional gain
float ki = 0.1; // Integral gain
float integralTerm = 0; // Defining integral term

// Moving Average Filter Parameters
const int filterWindowSize = 10; // Window size for the average filter, change this
     for incresed filtering!!
float filterWindow[filterWindowSize]; // Array for filter window values
int filterIndex = 0; // Filter window index
float filterSum = 0; // Sum of the filter window values
int filterCount = 0; // Count number of values in the filter window

void setup() {
  Serial.begin(9600); // Serial communication at 9600 baud rate
  pinMode(RectifiedVoltageDigitalOutputPin, OUTPUT); // Defining the rectified
      output voltage pin

  // Initialize filter window
  for (int i = 0; i < filterWindowSize; i++) {
    filterWindow[i] = 0; // Initialize each element of the filter window to 0
  }
}

void loop() {
  // AC Voltage Measurement
  if (millis() >= voltageLastSample + 1) { // Check if 1 millisecond has passed
      since the last voltage sample
    voltageSampleRead = (analogRead(VoltageAnalogInputPin) - 512) * 2 +
        voltageOffset1;
    voltageSampleSum += sq(voltageSampleRead); // Add the square of the sample
    voltageSampleCount++; // Increase the sample count
    voltageLastSample = millis(); // Update the time from last voltage sample

    // Zero crossing detection
    if ((voltageSampleRead >= 0 && voltageLastSample - lastVoltageZeroCrossingTime
        > 10) ||
        (voltageSampleRead < 0 && lastVoltageZeroCrossingTime == 0)) {
      if (lastVoltageZeroCrossingTime != 0) {
        float period = voltageLastSample - lastVoltageZeroCrossingTime; //
            Calculate the period between zero crossings
        voltageFrequency = 1000.0 / period; // Frequency calculated by the period
      }
      lastVoltageZeroCrossingTime = voltageLastSample; // Update time from last
          zero crossing
    }
  }
  if (voltageSampleCount == 1000) {
    voltageMean = voltageSampleSum / voltageSampleCount; // Mean voltage
    RMSVoltageMean = sqrt(voltageMean) + voltageOffset2; // RMS voltage with offset
    Serial.print("Voltage RMS:");
    Serial.print(RMSVoltageMean, decimalPrecision);
    Serial.println("V  ");
    voltageSampleSum = 0; // Reset sum of samples
    voltageSampleCount = 0; // Reset sample count
  }

  // AC Current Measurement
  if (millis() >= currentLastSample + 1) { // Check if 1 millisecond has passed
      since the last current sample
    currentSampleRead = analogRead(CurrentAnalogInputPin) - 512 + currentOffset1;
    currentSampleSum += sq(currentSampleRead); // Add the square of the sample
    currentSampleCount++; // Increase the sample count
    currentLastSample = millis(); // Update the time from last current sample
  }
  if (currentSampleCount == 1000) { //
    currentMean = currentSampleSum / currentSampleCount; // Mean current
    RMSCurrentMean = sqrt(currentMean) + currentOffset2; // RMS current with offset
    FinalRMSCurrent = ((RMSCurrentMean / 1024.0) * 5000.0) / mVperAmpValue; //
```

```
        Conversion of RMS current
    Serial.print("Current RMS:");
    Serial.print(FinalRMSCurrent, decimalPrecision);
    Serial.println(" A  ");
    currentSampleSum = 0; // Reset sum of samples
    currentSampleCount = 0; // Reset sample count
  }

  // AC Rectified Voltage Generation & Phase Shifting
  unsigned long currentTime = millis(); // Current time in milliseconds
  float phaseShiftRadians = 0; // Phase shift in radians
  float generatedVoltage = 650 + (2000 * fabs(sin(2 * PI * voltageFrequency * (
      currentTime / 1000.0) + phaseShiftRadians))); // Generate a rectified voltage
       signal
  float rectifiedVoltage = max(0.0, generatedVoltage); // Ensuring non-negative
      rectified voltage

  // Moving Average Filter
  filterSum -= filterWindow[filterIndex]; // Subtract the first value
  filterWindow[filterIndex] = rectifiedVoltage; // Add the new value to the filter
      window
  filterSum += rectifiedVoltage; // Add the new value to the sum
  filterIndex = (filterIndex + 1) % filterWindowSize; // Update the index
  if (filterCount < filterWindowSize) {
    filterCount++; //
  }
  float filteredVoltage = filterSum / filterCount; // Average of the filtered
      voltage

  // Send data to the integrated DAC
  int dacValue = map(filteredVoltage, 650, 2650, 0, 255); // Express the filtered
      voltage as a DAC value
  analogWrite(RectifiedVoltageDigitalOutputPin, dacValue); // Write the DAC value
      to the output pin

  // AC Power Measurement
  if (millis() >= powerLastSample + 1) { // Check if 1 millisecond has passed since
       the last power sample
    sampleCurrent1 = analogRead(CurrentAnalogInputPin) - 512 + currentOffset1;
    sampleCurrent2 = (sampleCurrent1 / 1024.0) * 5000.0; // Conversion to
        millivolts
    sampleCurrent3 = sampleCurrent2 / mVperAmpValue; // Conversion to ampere
    voltageSampleRead = (analogRead(VoltageAnalogInputPin) - 512) * 2 +
        voltageOffset1;
    powerSampleRead = voltageSampleRead * sampleCurrent3; // Instantaneous power
        calculation
    powerSampleSum += powerSampleRead; // Power sample added to the sum
    powerSampleCount++; // Increase the sample count
    powerLastSample = millis(); // Update the time from last power sample
  }
  if (powerSampleCount == 1000) {
    realPower = (powerSampleSum / powerSampleCount) + powerOffset; // Real power
        with offset
    Serial.print("Real Power (W): ");
    Serial.println(" W  ");
    apparentPower = FinalRMSCurrent * RMSVoltageMean; // Calculate the apparent
        power
    Serial.print("Apparent Power (VA): ");
    Serial.print(apparentPower, decimalPrecision);
    Serial.println(" VA  ");
    powerFactor = realPower / apparentPower; // Calculate the power factor
    Serial.print("Power Factor: ");
    Serial.println(powerFactor, decimalPrecision);
    calculateTimeDelay(powerFactor); // Calculate the time delay for the selected
        power factor
    powerSampleSum = 0; // Reset the sum of samples
    powerSampleCount = 0; // Reset the sample count
  }
}
```

```
void calculateTimeDelay(float pf) {
  float error = desiredPowerFactor - pf; // Error between the selected- and actual
      power factor
  integralTerm += error; // Update the integral term with the error
  float output = kp * error + ki * integralTerm; // Controller output
}
```

DEPARTMENT OF SOME SUBJECT OR TECHNOLOGY
CHALMERS UNIVERSITY OF TECHNOLOGY
Gothenburg, Sweden
www.chalmers.se

CHALMERS
UNIVERSITY OF TECHNOLOGY